U.PORTO

Universidade do Porto
FEUP Faculdade de Engenharia

Finite element analysis of residual stresses in parts manufactured by laser powder-bed fusion

Jorge Wolfs Gil

Dissertation submitted to
Faculty of Engineering of the University of Porto
for the degree of

Masters in Mechanical Engineering

Advisor:
Prof. Dr. Abílio de Jesus

Co-advisors:
MSc. Felipe Fiorentin
Dr. João Pereira

Department of Mechanical Engineering
Faculty of Engineering of the University of Porto

June 30th, Porto, 2020

The work presented in this dissertation was performed at
Advanced Manufacturing Processes Unit (UTAF)
Institute of Science and Innovation in Mechanical
and Industrial Engineering (INEGI)
Porto, Portugal.

Jorge Wolfs Gil
E-mail: jgil@inegi.up.pt

Instituto de Ciência e Inovação em Engenharia Mecânica
e Engenharia Industrial
Unidade de Tecnologias Avançadas de Fabrico
Rua Dr. Roberto Frias s/n
4200-465 Porto
Portugal

Abstract

Additive manufacturing has significantly improved from its early objective of producing aesthetic prototypes for product development applications, into manufacturing structurally demanding components, as materials, accuracy and the overall quality of the output evolved. Hence, the demand for numerical models that allow satisfying predictions in regards to a component's microstructure, distortion and residual stresses has increased. Therefore, it is of utmost importance to not only know how to use a finite element tool, but to understand it and its parameters.

Within this context of distortion and residual stress simulation in parts produced through additive manufacturing lies the main goal of this dissertation: to gain insight into the commercially available finite element packages that simulate metallic additive manufacturing process, more specifically, laser powder bed fusion. This is done in two distinct, but complementary ways: establishing convergence and parametrical studies that determine the influence of simulation inputs and their respective impact on the predicted residual stress field, and simulating the conditions of existing physical systems that allow the comparison with experimental values. Two software packages were employed in the following analysis, knowing that their formulation varies in complexity: one applies a weakly-coupled thermomechanical model while the other doesn't perform a heat transfer analysis.

Firstly, convergence studies were conducted to measure the influence of a component's mesh in its residual stresses; then, several geometrical and manufacturing parameters with varying base plate thickness were developed; the effects of the laser speed, hatch spacing, pre-heat temperature and cooldown temperature were assessed.

Comparisons between two software packages were established, using three distinct physical models: a one layered component; a component with very simple geometry, thus relinquishing the need for support structures and minimising the mesh's effect; a benchmark unit developed by the National Institute of Standards and Technology (NIST), designed for the study of residual stresses. This also allowed the validation of the overall process, establishing an analogous case in distinct softwares.

The analysis of the displacement and stress field with the progressive removal of a workpiece from its baseplate was analysed and compared to experimental values.

Lastly, comparisons of the residual strain field with experimental values were conducted for the benchmark component, allowing final conclusions on the validity and robustness of the provided solutions.

Keywords: Finite Element Method, Laser Powder-Bed Fusion, Metallic Additive Manufacturing, Residual Stresses

Resumo

Processos de fabrico aditivo evoluíram significativamente desde a sua incepção, em que eram sobretudo utilizados como processos expeditos de fabrico de protótipos com fins estéticos, para o desenvolvimento de peças de aplicação estrutural, uma evolução possibilitada por melhorias nos materiais envolvidos, na precisão geométrica e na qualidade global do produto final. Consequentemente, a demanda por modelos numéricos que permitem a previsão satisfatória de microestrutura, distorção e do tensões residuais aumentou. Logo, é de extrema importância não apenas saber como utilizar um software, mas conhecer a sua formulação e os seus parâmetros.

Dentro do contexto de simulação numérica de distorções e tensões residuais em peças manufaturadas por fabrico aditivo encontra-se o objetivo principal desta dissertação: compreender melhor o funcionamento dos programas comerciais de elementos finitos que simulem o processo de fabrico aditivo metálico, mais especificamente o processo de *laser powder bed fusion*. O procedimento para atingir este objetivo é distinto, mas complementar: estabelecer estudos paramétricos e de convergência de forma a determinar a influência das variáveis e o seu respetivo impacto na previsão do campo de tensões residuais, e simular o processo com parâmetros de fabrico idênticos a peças existentes, permitindo a comparação de valores com valores obtidos experimentalmente. Foram escolhidos dois softwares para os estudos conduzidos, sabendo que formulam o problema de maneiras distintas: um software recorre a uma análise termomecânica fracamente acoplada, enquanto o segundo não concretiza uma análise de transferências de calor.

Primeiramente, estudos de convergência foram efetuados de forma a medir a influência da malha de uma peça nas suas tensões residuais; de seguida, diversos modelos com diferentes espessuras de placa de base foram desenvolvidos; os efeitos da velocidade do laser, largura entre passes, temperatura de pré-aquecimento e temperatura de arrefecimento também foram determinadas.

Comparações entre os dois programas foram estabelecidas recorrendo a três peças distintas: uma componente constituída por uma só camada; uma componente geometricamente simples de forma a minimizar os efeitos de malha e não necessitar de suportes; uma componente de referência, desenvolvida pelo Instituto Americano de Padrões e Tecnologia (NIST), especialmente pensada para estudos de tensões residuais. Estas simulações permitiram também a validação do processo, estabelecendo um caso análogo aos dois programas.

A análise de deslocamentos e do campo de tensões para uma peça progressivamente removida da placa base também foi efetuada, e comparada com valores experimentais.

Por último, comparações entre resultados numéricos e valores obtidos experimentalmente foram efetuadas para o componente de referência, permitindo concluir sobre a validade e robustez das soluções numéricas determinadas.

Palavras-chave: Método de Elementos Finitos, Laser Powder-Bed Fusion, Fabrico Aditivo Metálico, Tensões Residuais

To my sister.

'Off we go! Goodbye, until we meet soon, dear friends.'

Yuri Gagarin

Acknowledgements

First and foremost, I would like to write a few words of appreciation and gratitude to everyone involved in the development of this thesis:

To Professor Dr. Abílio de Jesus, for trusting me with this dissertation, and despite all the adversities that emerged during the semester, didn't relinquish the frequent meetings to share knowledge and advice;

To FCT, whose continuous support towards the Add.Strength project and team allowed this thesis to take place;

To Engineer Felipe Fiorentin, who was ceaselessly available for meetings, helping me overcome the obstacles that appeared;

To Dr. João Pereira for his availability and professionalism that helped me settle at INEGI;

To all INEGI collaborators, who made me feel at home;

To all the teachers that accompanied me during the last five years at FEUP, whose dedication and commitment made me grow as a student and as a human being;

To my parents for all of their immense effort giving me the conditions to attend this course, remaining ever so supportive throughout;

To my sister, who although distant, always felt close, and taught me that it is possible to go your own way;

To Miguel Neto, whose loyalty and kindness is immeasurable, making me proud of calling a friend;

To Carolina Fernandes, an inspiration to me every single day, and whose thought alone makes me smile, helping me no matter what the issue at hand is;

To all of my friends, with whom I crafted wonderful memories that I will cherish for the rest of my life.

To everyone mentioned, I wholeheartedly thank, for I wouldn't be here without them.

Institutional acknowledgements

The project *Add.Strength* entitled "Enhanced Mechanical Properties in Additive Manufactured Components" funded by the Programa Operacional Competitividade e Internacionalização, and Programa Operacional Regional de Lisboa funded by FEDER and National Funds (FCT) is acknowledged (Reference PTDC/EME-EME/31307/2017). The BIC scholarship funded by the *Add.Strength* project is also acknowledged. The projet "MAMTool - Machinability of Additive Manufactured Parts for Tooling Industry" funded by the Programa Operacional Competitividade e Internacionalização, and Programa Operacional Regional de Lisboa funded by FEDER and National Funds (FCT) is acknowledged (Reference PTDC/EME-EME/31895/2017).

Contents

Abstract i

Resumo iii

Acknowledgements ix

Institutional acknowledgements xi

1 Introduction 1
- 1.1 Framework and motivation . . . 1
- 1.2 Objectives . . . 2
- 1.3 Layout . . . 3

2 Theoretical Review 5
- 2.1 Additive Manufacturing . . . 5
  - 2.1.1 Introduction and Definition . . . 5
  - 2.1.2 Developments . . . 5
  - 2.1.3 Description of a generic AM process . . . 6
  - 2.1.4 Design for AM . . . 6
  - 2.1.5 Metallic AM processes . . . 8
  - 2.1.6 LPBF process parameters . . . 10
  - 2.1.7 Mechanical considerations . . . 11
- 2.2 Finite Element Method . . . 13
  - 2.2.1 Introduction . . . 13
  - 2.2.2 FEM within AM . . . 14

3 Simulation Details and Methods 21
- 3.1 Physical specimens . . . 21
  - 3.1.1 Introduction . . . 21
  - 3.1.2 Prism . . . 22
  - 3.1.3 INEGI's benchmark bridges . . . 23
  - 3.1.4 NIST's benchmark bridges . . . 26
- 3.2 Material definition . . . 26
  - 3.2.1 Introduction . . . 26
  - 3.2.2 Software #1 . . . 26
  - 3.2.3 Software #2 . . . 28
- 3.3 Parametric analysis . . . 33
  - 3.3.1 Introduction . . . 33
  - 3.3.2 Software #1 . . . 33
  - 3.3.3 Software #2 . . . 37

3.4 Simulations aimed at comparing software . . . 39
3.4.1 One layer . . . 39
3.4.2 Prism . . . 39
3.4.3 Benchmark bridges . . . 40
3.5 Part removal simulation . . . 40
3.6 Comparison between numerical and experimental results . . . 41
3.6.1 Experimental result attainment . . . 42
3.6.2 Process parameters . . . 43

4 Results and Discussion **45**
4.1 Parametric simulations . . . 45
4.1.1 Mesh size . . . 46
4.1.2 Lumping Factor . . . 52
4.1.3 Baseplate Thickness . . . 56
4.1.4 Laser Speed . . . 58
4.1.5 Hatch Spacing . . . 60
4.1.6 Preheat temperature . . . 63
4.1.7 Cooldown temperature . . . 64
4.2 Simulations aimed at comparing software . . . 64
4.2.1 One layer . . . 64
4.2.2 Prism . . . 67
4.2.3 Benchmark Bridges . . . 73
4.3 Part removal . . . 84
4.4 Comparison between numerical and experimental results . . . 85
4.4.1 Residual strain field . . . 86
4.4.2 Deflection analysis . . . 95

5 Conclusions and Future Work **97**
5.1 Conclusions . . . 97
5.2 Future Work . . . 98

References **99**

A Fatigue Overview and Preliminary Experimental Results **105**
A.1 Introduction . . . 105
A.2 Fatigue . . . 105
A.2.1 Introduction and definition . . . 105
A.2.2 Stress-life method . . . 106
A.2.3 Strain-life method . . . 109
A.2.4 Fracture mechanics . . . 111
A.2.5 Fatigue life and modifying factors . . . 114
A.2.6 Stress concentration and notch sensitivity . . . 115
A.2.7 Accumulated damage . . . 116
A.2.8 Fatigue tests . . . 116
A.3 Preliminary results . . . 117

B Distortion Evaluation Experimental Procedure **123**
B.1 Electrical discharge machining . . . 123
B.1.1 Introduction and definition . . . 123
B.1.2 Developments . . . 126

B.1.3 Parameters 126
B.1.4 Materials 127
B.2 Future procedure 128

Appendix references **131**

List of Figures

Figure 2.1: Schematic representation of .STL wireframe. 7
Figure 2.2: Schematic representation of same cylinder design printed with two distinct orientations. 7
Figure 2.3: Schematic representation of structural improvement through size, shape and topology optimisation. 9
Figure 2.4: Representation of a topology optimisation workflow for a structural example. 10
Figure 2.5: Schematic representation of DED process. 10
Figure 2.6: Typical LPBF machine setup. 11
Figure 2.7: Basic mechanisms of stress and plastic deformation evolution. . . . 12
Figure 2.8: Examples of residual stress types into three categories. 12
Figure 2.9: Schematic representation of the Finite Element Method computational model's structure 14
Figure 2.10: Interaction between phenomena in the LPBF process. 15
Figure 2.11: Schematic representation of thermomechanical coupling. 17
Figure 2.12: Software #1's simulation stages. 19
Figure 2.13: Software #2's simulation stages 20

Figure 3.1: Schematic renders pertaining to the components subjected to study. 22
Figure 3.2: Prism dimensions and coordinate system (dimensions in millimetres). 23
Figure 3.3: Dimensional properties and geometrical details regarding thin legs and slanted corners pertaining to the benchmark bridges. 24
Figure 3.4: Benchmark bridges' layout within the baseplate, numeration and coordinate system. 25
Figure 3.5: Scanning strategies of the benchmark bridges, printed by *EROFIO*. 25
Figure 3.6: 316 stainless steel properties as functions of temperature, as defined in Software #1's internal libraries. 28
Figure 3.7: 316 stainless steel properties as functions of temperature, as defined in Software #2's internal libraries. 30
Figure 3.8: Iconel 625 properties as functions of temperature, as defined in Software #2's internal libraries. 31
Figure 3.9: Plasticity laws in function of temperature, as defined in Software #2's internal library. 32
Figure 3.10: Mesh size evolution within the 2nd Group of simulations using Software #1, with lumping factor of 50. 35
Figure 3.11: Mesh size evolution within the 2nd Group of simulations using Software #1, with a mesh size of 2.5 mm. 35
Figure 3.12: Software #1's meshing strategies. 36
Figure 3.13: One layer meshing strategy. 39

Figure 3.14: Mesh evolution according to the projection factor. 40
Figure 3.15: Evolution of the boundary conditions between the benchmark bridge and the baseplate in the removal simulation. 40
Figure 3.16: Schematic representation of plane in which residual strains were experimentally measured. 42
Figure 3.17: Measurement locations, in the Iconel 625 benchmark bridges produced by NIST, for the residual strains using X-ray diffraction. . . 42

Figure 4.1: Schematic representation of nodes (A), (B) and (C). 45
Figure 4.2: Evolution of longitudinal σ_{xx} and transverse σ_{yy} stresses in node (C). 49
Figure 4.3: Evolution of out-of-plane stresses σ_{zz} in nodes (A) and (B). 50
Figure 4.4: Software #1's mesh refinement in baseplate-workpiece interface, for mesh size of 5 mm and lumping factor of 25. 51
Figure 4.5: Schematic representation of meshes requiring hanging nodes. 51
Figure 4.6: Evolution of stresses in node (C) with an increase in the number of layers that are simulated. 53
Figure 4.7: Evolution of stresses with an increase in the number of layers that are simulated. 54
Figure 4.8: σ_{zz} configuration with a decrease in the Lumping Factor, for the same mesh of 2.5 mm, with section cut at $y = 5$ mm plane. 54
Figure 4.9: Three dimensional convergence curves. 55
Figure 4.10: Evolution of stresses with an increase in the baseplate's thickness. . 57
Figure 4.11: Longitudinal stress distribution σ_{xx} with large strain hypothesis. . . 58
Figure 4.12: Evolution of stresses with an increase in laser speed. 59
Figure 4.13: Laser speed influence on time step creation. 60
Figure 4.14: Evolution of stresses with an increase in hatch distance. 61
Figure 4.15: Transverse stress σ_{yy} field with different hatch spacing values. . . . 61
Figure 4.16: Evolution of temperature steps with hatch distance. 62
Figure 4.17: Hatch spacing influence on time step creation. 62
Figure 4.18: Schematic representation of the thermal boundary conditions. . . . 63
Figure 4.19: Evolution of stresses with an increase in preheat temperature. . . . 63
Figure 4.20: Evolution of stresses with an increase in cooldown temperature. . . 64
Figure 4.21: Definition of node (D). 65
Figure 4.22: Bar plot with stresses obtained in node (D). 66
Figure 4.23: Temperature T, longitudinal σ_{xx} and transverse σ_{yy} stress evolution with time, in single layer configuration. 66
Figure 4.24: Stress configuration changes for two time steps, for Software #2. . 67
Figure 4.25: Meshes used in prism comparison, as defined in Software #2. . . . 68
Figure 4.26: σ_{xx} and σ_{yy} stress values for node (C), and σ_{zz} for node (A), for a cubic 5 mm mesh. 68
Figure 4.27: σ_{xx} and σ_{yy} stress values in node (C), and σ_{zz} in node (A), for a 1 mm mesh. 69
Figure 4.28: Longitudinal stresses σ_{xx} contour plots. 71
Figure 4.29: Definition of node (E). 71
Figure 4.30: Longitudinal stress σ_{xx} and temperature T evolution with time, in node (E). 72
Figure 4.31: σ_{xx} comparison between Software #1 and Software #2, before cooldown. 72
Figure 4.32: Definition of node (N), used to retrieve residual stress values in Software #1. 73

Figure 4.33: Longitudinal and transverse stress convergence curves, in node (N), in Software #1. 74
Figure 4.34: Schematic representation of the aspect ratio in hexahedral elements. 74
Figure 4.35: Schematic representation of the Jacobian ratio in hexahedral elements. 75
Figure 4.36: Element quality contour plots, for three meshes with different projection factors, as defined in Software #2. 77
Figure 4.37: Jacobian ratio contour plots, for three meshes with different projection factors, as defined in Software #2. 78
Figure 4.38: Aspect ratio contour plots, for three meshes with different projection factors, as defined in Software #2. 79
Figure 4.39: Element quality contour plots of bevelled extremity detail, for two different meshes, as defined in Software #2. 80
Figure 4.40: Element quality contour plots of bridge legs, for two different meshes, as defined in Software #2. 80
Figure 4.41: Longitudinal and transverse stresses in node (N), for different projection factor meshes, in Software #2 81
Figure 4.42: Longitudinal stress σ_{xx} contour plots for three different projection factors, as defined in Software #2, for the benchmark bridge's simulation. 82
Figure 4.43: Longitudinal stress σ_{xx} contour plots in the slanted legs detail, for three different projection factors, as defined in Software #2, for the benchmark bridge's simulation. 83
Figure 4.44: Points used to track nodal variables during the removal stage of the benchmark bridge's legs, in Software #1. 84
Figure 4.45: Stress and displacement evolution with number of removed legs. . . 85
Figure 4.46: Displacement u_{zz} evolution with number of removed legs. 85
Figure 4.47: Experimental and numerical comparison between longitudinal residual strain ε_{xx} contour plots, extracted from $y = 2.5\,\text{mm}$ plane in Iconel 625 benchmark bridges. 87
Figure 4.48: Experimental and numerical comparison between vertical residual strain ε_{zz} contour plots, extracted from $y = 2.5\,\text{mm}$ plane in Iconel 625 benchmark bridges. 88
Figure 4.49: Experimental and numerical comparison between vertical residual strain ε_{xz} contour plots, extracted from $y = 2.5\,\text{mm}$ plane in Iconel 625 benchmark bridges. 89
Figure 4.50: Experimental and numerical and numerical comparison between skewed residual strain ε_{45} contour plots, extracted from $y = 2.5\,\text{mm}$ plane in Iconel 625 benchmark bridges. 90
Figure 4.51: Longitudinal elastic strain ε_{xx} contour plots, extracted from $y = 2.5\,\text{mm}$ plane in Iconel 625 benchmark bridges. 91
Figure 4.52: vertical residual strain ε_{zz} contour plots, extracted from $y = 2.5\,\text{mm}$ plane in Iconel 625 benchmark bridges. 92
Figure 4.53: vertical residual strain ε_{xz} contour plots, extracted from $y = 2.5\,\text{mm}$ plane in Iconel 625 benchmark bridges. 93
Figure 4.54: Skewed residual strain ε_{45} contour plots, extracted from $y = 2.5\,\text{mm}$ plane in Iconel 625 benchmark bridges. 94
Figure 4.55: Experimental and numerical comparison between vertical deflection u_{zz} after leg removal. 95

Figure 4.56: Displacement u_{zz} contour plot with geometrical scale of 6.6. 96

Figure A.1: Repeated stress cycle with a positive mean stress σ_m. 107
Figure A.2: Typical behaviours of S-N curves. 108
Figure A.3: Hysterisis loop showing the first five stress reversals. 109
Figure A.4: Schematic of a total strain amplitude-life curve. 110
Figure A.5: Modes of fracture. 112
Figure A.6: Fracture parameters: δ_m, δ_t, δ_5 and ψ_t. 113
Figure A.7: Comparison between Dugdale's and Irwin's normalised stress intensity factor approximation. 113
Figure A.8: Schematic representation of a typical $da/dN = f(\Delta K)$ curve (adapted from [A10]). 114
Figure A.9: Schematic representation of the stress evolution in a notched component. 115
Figure A.10: Fatigue specimens. 117
Figure A.11: Specimens for axial fatigue analysis. 118
Figure A.12: Ageing chart for Maraging steel (holding time of three hours). . . . 119
Figure A.13: Fatigue testing results, shown in logarithmic representation. 120
Figure A.14: Fractured specimen photos detailing fracture zones resulting from fatigue testing. 121

Figure B.1: EDM cycle phases. 124
Figure B.2: Visual representation of frequency's impact on finishing. 124
Figure B.3: Visual representation of WEDM. 125
Figure B.4: Diagram with suggest future tasks 129

List of Tables

Table 3.1: Some machine settings used in the AM process of the prism. 23
Table 3.2: Additional machine settings used in the AM process of the benchmark bridges. 25
Table 3.3: 316L and Iconel 625's properties, as defined by Software #1's internal library. 27
Table 3.4: 316L and Iconel 625 chemical compositions. 27
Table 3.5: 316L thermal properties, as user-defined in Software #2. 29
Table 3.6: Physical properties of Iconel 625, as defined in Software #2 29
Table 3.7: Parameter simulation groups. 33
Table 3.8: Simulation properties common in all mesh size and lumping factor parametric studies, for Software #1. 34
Table 3.9: Developed numerical simulations to measure the effect of the lumping factor. 36
Table 3.10: Developed numerical simulations to measure the effect of the baseplate thickness. 36
Table 3.11: Simulation properties common in all baseplate thickness parametric studies, for Software #1. 37
Table 3.12: Simulation properties common in all parametric studies, for Software #2. 38
Table 3.13: Laser speed parameter values. 38
Table 3.14: Hatch space parameter values. 38
Table 3.15: Preheat temperature parameter values. 39
Table 3.16: Cooldown Temperature parameter values. 39
Table 3.17: Simulation properties of the benchmark bridge removal simulation, for Software #1. 41
Table 3.18: Simulation properties of the benchmark bridge removal simulation, for Software #2. 43

Table 4.1: Baseplate bending stiffness. 57
Table 4.2: Stress values for the one layer case, for both software packages. . . . 65
Table 4.3: Mesh size, lumping factor and total number of elements in part. . . 73
Table 4.4: Percentage of elements that fulfil mesh metric condition, for three different meshes, pertaining to benchmark bridge with differing projection factors, in Software #2 76

Table A.1: S-N curve parameters for AM and conventional specimens. 118
Table A.2: S-N curve parameters for miniature specimens under bending loading conditions. 120

Acronyms

AM Additive Manufacturing. 1, 2, 5, 6, 8, 9, 11, 12, 16–21, 26, 28, 39, 63, 66, 97, 117–119

AMF Additive Manufacturing File Format. 6

ASCs Anisotropic Strain Coefficients. 16

ASTM American Society for Testing and Materials. 6, 117

BIC Initiation in Science Scholarship. 2

CAD Computer Aided Design. 5, 6, 9

CAM Computer Aided Manufacturing. 5

CMM Coordinate Measuring Machine. 95

DED Direct Energy Deposition. 8, 9, 18

DSPC Direct Shell Production Casting. 5

EBM Electron Beam Melting. 9, 10

EDM Electrical Discharge Machining. xx, 42, 84, 95, 123–127

FCC Face-Centred Cubic. 27

FCT Foundation for Science and Technology. 2

FDM Fused Deposition Modelling. 5

FEA Finite Element Analysis. 41, 74, 76, 86, 95, 97

FEM Finite Element Method. 13, 17, 20, 21, 56

FEUP Faculty of Engineering of the University of Porto. 2

FSDT First Shear Deformation Theory. 56

GSAS General Structural Analysis System. 42

HCF High Cycle Fatigue. 106

INEGI Institute for Science and Innovation in Mechanical and Industrial Engineering. 1, 2, 22, 23, 43, 85, 98, 117

ISO International Organisation for Standardisation. 6

LCF Linear Elastic Fracture Mechanics. 111

LCF Low Cycle Fatigue. 106

LOM Laminated Object Manufacturing. 5

LPBF Laser Powder Bed Fusion. xvii, 2, 8–11, 14, 15, 18, 21, 37, 52, 86

NIST National Institute of Standards and Technology. 21, 22, 26, 41, 86, 98

PBF Powder Bed Fusion. 7–9

SGC Solid Ground Curing. 5

SLM Selective Laser Melting. 9, 63

SLS Selective Laser Sintering. 5

STL Stereolithography. 6, 18

USA United States of America. 126

USSR Union of Soviet Socialist Republics. 126

UTAF Advanced Manufacturing Processes Unit. 1

WEDM Wire Electrical Discharge Machining. xx, 22, 86, 124, 125, 127

List of Symbols

β	Fracture correction factor
Δa	Crack extension
δ_5	Crack opening displacement
δ_m	Crack mouth opening displacement
δ_t	Crack tip opening displacement
η	Isoparametric coordinate, analogous to the y direction
Γ	Closed contour path
γ	Element-dependent constant
ν	Poisson's ratio
Ω_e	Element's domain
ϕ_x	Rotation about the positive y axis
ϕ_y	Rotation about the negative x axis
ψ_j	Shape function defined in node j
ψ_m	Crack tip opening angle
ρ	Density
σ_a	Stress amplitude
σ'_f	Fatigue strength coefficient
σ_f^{co}	Corrected fatigue strength
σ_m	Mean stress
σ_r	Stress range
σ_t	True stress
σ_{fo}	Fatigue limit
σ_{max}	Maximum stress
σ_{min}	Minimum stress

σ_{ts} Ultimate tensile strength

σ_y Yield strength

ε'_f Fatigue ductility coefficient

ε_i Strain along i direction

ε_{45} Strain 45° off the z direction

ε_e Elastic strain

ε_{inh} Inherent strain

ε_p Plastic strain

ε_{tot} Total strain

ε_T Thermal strain

ε_t True strain

$\boldsymbol{\sigma}$ Cauchy stress tensor

$\boldsymbol{B}$ Deformation matrix

$\boldsymbol{C}$ Fourth order elastic stiffness matrix

$\boldsymbol{f}$ Nodal force vector

$\boldsymbol{K}$ Stiffness matrix

$\boldsymbol{T}$ Tensile vector

$\boldsymbol{u}$ Nodal displacement vector

ξ Isoparametric coordinate, analogous to the x direction

ζ Isoparametric coordinate, analogous to the z direction

a Effective crack length

a_0 Unstrained lattice parameter

a_i Unit cell parameter along direction i

AR Aspect Ratio

b Fatigue strength exponent

c Fatigue ductility exponent

c_p Specific heat

D Plate's bending stiffness

d_{hkl} Lattice interplanar spacing

ds Infinitesimal contour element

E	Young's modulus
E_t	Tangent modulus
E_v	Deposited energy
EQ	Element quality
G_I	Strain energy release rate
h	Hatch distance
k	Thermal conductivity coefficient
K'	Cyclic strength coefficient
K_f	Practical stress concentration factor
K_I	Fracture toughness
K_t	Theoretical stress concentration factor
LF	Lumping Factor
M	Unitary moment
N	Number of cycles
n'	Cyclic strain hardening exponent
N_f	Cycles until failure
N_n	Number of nodes
P_b	Beam power
Q	Heat source
q	Notch sensitivity factor
R	Stress range
SSF	Strain Scaling Factor
T	Temperature
t	Plate thickness
T_m	Melting temperature
t_{layer}	Layer thickness
t_{num}	Numerical layer thickness
V	Volume
v_s	Scanning speed
W	Strain energy density
Y	Geometry and loading function

Chapter 1

Introduction

1.1 Framework and motivation

Metallic Additive Manufacturing (AM) has experienced a significant rise in its popularity since its inception: the ability to produce parts with almost no geometrical limitations [1] is remarkably valuable [2], specially with the emergence of numerical methods such as topology optimisation that generate structures according to specified objective functions [3]. These methods are able to significantly reduce the component's mass while simultaneously maintaining structural integrity, at the cost of generating extremely complex geometries that no other technological process could manufacture with the same ease [2, 4]. Additionally, several materials common in the realm of additive manufacturing, such as Maraging steel [5] and 17-4PH stainless steel [6] which are characterised by their high tensile strength and toughness, see their use outside AM often limited, further fuelling an interest in its technologies.

Although there are multiple advantages to AM technologies beyond geometrical flexibility, like the need for little to no human interaction during the process and reduced design cycle times [1], it inherently introduces defects that must not be ignored: excessive surface roughness [7], dimensional imprecision owing to the heat cycles during layer deposition [8], microstructural defects due to the part's interaction with the surrounding atmosphere and rapid cooling [9], and residual stresses that arise from plastic deformation induced from localised material expansion and contraction between different layers [10, 11, 12] are all problems that must be accounted for during the design period of a product and its production stage.

With this increase in additive manufacturing's popularity, and due to the growing use of AM produced parts in structural applications, several commercial software packages have been developed with the objective of predicting these defects and studying their implications. Accurate numerical solutions bring considerable value to the design table: despite not completely replacing experimental data, they can provide insights to the engineer on how a fully printed component behaves [2]. Hence, knowledge that encompasses the finite element method's particular formulation in the AM problem, more specifically the origin of residual stresses and the multiple parameter's influences on their magnitude, is this thesis' motivation.

The developed work, present in this thesis, is incorporated in the ongoing *Add.Strength - Enhanced mechanical properties in additive manufactured components* project, aimed at studying and understanding the mechanical behaviour in parts produced through metallic Additive Manufacturing processes. This project is integrated in the Advanced Manufacturing Processes Unit (UTAF), within the Institute for Science and Innovation in Mechanical

and Industrial Engineering (INEGI), a research centre situated inside the Faculty of Engineering of the University of Porto (FEUP)'s campus, ensuring a strong bond between these two institutions. The *Add.Strength* project is focused in the study of fatigue, characterising materials used in the context of Additive Manufacturing through both experimental testing and numerical simulations. This thesis was funded by the Foundation for Science and Technology (FCT) through a Initiation in Science Scholarship (BIC) scholarship.

Initially, this thesis' objective was the experimental determination of the distortions and the residual stress state of a component produced by Laser Powder Bed Fusion (LPBF), complemented by a fatigue analysis of the component. However, due to the unfortunate circumstances of the COVID-19 global pandemic and the subsequent restrictions on industrial and academic activity, the thesis' main goal shifted towards a more numerical approach that could nevertheless be developed. Hence, the developed work fits the objectives set by the *Add.Strength* project, by providing an insight into the available numerical software packages that allow the determination of the macroscale variables, such as the displacement field and the subsequent residual strains and stresses.

1.2 Objectives

The main goal of this dissertation is to gain insight into the commercially available finite element packages that simulate the displacement and residual stress fields in components manufactured by Laser Powder Bed Fusion. This is achieved by analysing the existing literature on numerical calculation of distortions in parts produced by AM, the performance of both parametric and convergence studies where the influence of mesh refinement and process parameters are measured. A comparison with experimental data is also conducted for multiple scenarios, where the physical workpiece and its material varies.

The outline of the executed simulations is as follows:

- Mesh convergence studies, in which a component's in-plane mesh fineness (elements per numerical layer) is increased through user-controlled parameters;
- Mesh convergence study where the out-of-plane fineness (number of numerical layers) is increased;
- Comparison between the in-plane and out-of-plane mesh fineness in result convergence and construction of three dimensional convergence curves;
- Baseplate studies, where the thickness of the rigid baseplate that holds the part during the printing process is modified;
- Hatch space, laser speed, preheat temperature and cooldown temperature parametric analysis;
- Comparison between the two used software packages through a single layer, 316L stainless steel component that allows material definition validation;
- Comparison between the two used software packages through a prism component and a benchmark component, providing an insight in the difference of thermomechanical formulations;
- Part removal simulation, in which the benchmark component's removal from the baseplate is simulated, in order to determine the progressive distortions that occur;

- Simulating the printing process of the Benchmark bridges according to the known process parameters, using meshes that converged in previous simulations, subsequently comparing with known experimental data;
- Simulating the printing and removal process of the Benchmark bridges, and comparison to experimental values.

1.3 Layout

This dissertation is subdivided into five chapters:

- Introduction: the thesis' framework and motivation are explained, through a Framework and *Motivation* section that delves into the applications of the conducted study, an *Objectives* section that furthers the goals of the dissertation and the *Layout* section that outlines how the information is organised.
- Theoretical Review: a chapter dedicated to exploring the necessary concepts to grasp the developed work, with these being additive manufacturing and the finite element method;
- Simulation Details and Methods: the developed simulations are outlined and explained, mentioning the used software package, the process parameters, material definition and component geometry.
- Results and Discussion: the numerical solutions to the simulations mentioned in the previous chapter are detailed, and the respective discussion is carried out.
- Conclusions and Future Work: final remarks on the developed work are made, as well as possible future works that further the knowledge of additive manufacturing simulation;
- Appendix A: theoretical review of fatigue subjects, accompanied by an outline of the developed work previous to the COVID-19 pandemic that forced the alteration of the work's topic, and preliminary results;
- Appendix B: a work plan proposal regarding the initial dissertation's topic to serve as a future work, and a theoretical review on electrical discharge machining.

Chapter 2

Theoretical Review

2.1 Additive Manufacturing

2.1.1 Introduction and Definition

Additive Manufacturing (AM), 3D printing or rapid prototyping are all terms that describe the process by which a three dimensional part is built through the successive overlap of two-dimensional layers, materialised by a wide variety of constructive solutions. It contrasts against subtractive manufacturing, which encompasses processes that remove excess material to shape a workpiece into a final part [13].

Initially restricted to the production of prototypes and models with no mechanical purpose, additive manufacturing is witnessing a growing amount of interest in the production of structural components [4], a topic this dissertation focuses on. The amount of post-processing a component needs to go through depends on the stage of development of the part, with final versions of a workpiece needing a combination of heat treatments and subtractive manufacturing processes [2].

2.1.2 Developments

The idea and concept behind building a layered component is not exactly new; the first patent behind a similar approach can be found in 1902, for a laminated horse shoe; in 1952, Kojima demonstrated the benefits of layer manufacturing processes. The concept was further pushed and developed in the following decades, gaining rising amounts of traction; in the late 80s and early 90s, the first physical machines capable of producing parts by additive manufacturing processes came to the market. 3D Systems launched its first every system - the SLA-1 - in 1987, in the field of stereolithoraphy. Soon followed a collaborative effort between 3D Systems and Ciba-Geigy, introducing acrylate resins, that, to this day, are still used in Vat-photopolymerisation processes. Between 1991 and 1993, five different technologies entered the AM market: Fused Deposition Modelling (FDM) from Stratasys, Solid Ground Curing (SGC) from Cubital, Laminated Object Manufacturing (LOM) from Helisys in 1991; soon afterwards came Selective Laser Sintering (SLS) from DTM and Direct Shell Production Casting (DSPC) from Soligen. The two last technologies to be mentioned are now the largest sections in the AM market, as new and more advanced technologies are being developed [4].

Furthermore, it is important to highlight that without Computer Aided Design (CAD), there would be no Computer Aided Manufacturing (CAM), and without CAM, there would be no AM: the limitations of the process, therefore, are often related to numerical control,

software and hardware interaction. In addition, the progress of AM is not limited to the world of mechanical engineering [2].

2.1.3 Description of a generic AM process

Generally, the conception of a model through Additive Manufacturing can be described and categorised into eight major steps [2]:

1. CAD: a three dimensional model that describes the geometry of a part is made through CAD or by optical scanning of an existing workpiece;

2. Conversion to Stereolithography (STL): .STL has become the *de-facto* universal standard for input 3D files containing the necessary information describing the printing method. This step essentially forms the basis for computation of the several layers of which the final product is comprised of;

3. Transfer to AM machine: the file is transferred to the machine's environment, where final tweaks and repairs can still be performed;

4. Machine settings: the parameters of the process, such as layer thickness, hatch spacing and laser speed are set up;

5. Build: the component is produced. Even though it is mainly an automated process, it is still wise to routinely check if the printing procedure is processing without errors;

6. Removal: the system is removed from the machine environment;

7. Post-processing: some parts may require additional handling, such as cleaning and support removal;

8. Application: components may be ready or may otherwise warrant priming, painting or additional finishing modes.

The mentioned format, known as .STL, consists of the most widespread file format within the industry of Additive Manufacturing. It describes the geometry of a surface through the use of triangular facets, whose resolution is usually a user-controlled parameter in CAD software packages [2], and store this information through the use of the triangle's vertices and respective normal vectors. Furthermore, Figure 2.1 displays a schematic representation of how a 3D model is recreated through triangle faces, characteristic of a .STL file.

Furthermore, .STL files do not contain any information regarding the part's units, materials, colours or any information regarding the process parameters [2]: these limitations associated with the format have bolstered the push towards the adoption of the .AMF, the Additive Manufacturing File Format (AMF), which in turn is internationally registered as a standard file by ISO/ASTM [14].

2.1.4 Design for AM

Even though additive manufacturing does not share the same geometrical restrictions with other technological processes, there is still a set of conditions that should be kept in mind while designing parts to be manufactured through AM, present in this Section.

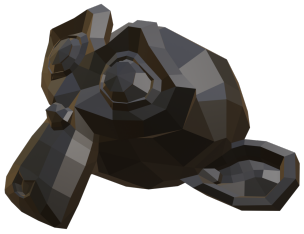

(a) 3D modelled object

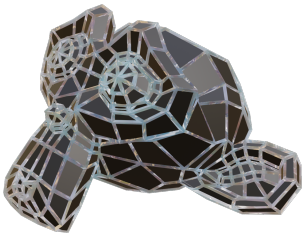

(b) Wireframe of 3D model

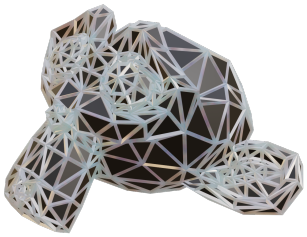

(c) .STL wireframe of 3D model

Figure 2.1: Schematic representation of .STL wireframe.

Build orientation

The geometric disposition in which the component is printed within the powder bed affects the part accuracy and its mechanical properties: an example would be the same cylinder design printed both horizontally and vertically, as Figure 2.2 schematically suggests, in which the vertical arrangement favours smoother edges as opposed to the horizontal layout, which would clearly present stair-step patterning on the sides [2].

Additionally, the boundaries of the component's surface affect the overall product and finishing quality: parts manufactured by PBF, whose surfaces are in contact with air instead of unmelted powder, display better roughness [2].

Figure 2.2: Schematic representation of same cylinder design printed with two distinct orientations.

Support removal

Even though the use of support structures is often unavoidable, as unsupported overhang sections of three dimensional components are likely to collapse [15], it is generally advisable to reduce these areas, since they require more material to be manufactured [15] and more post-processing associated with their removal [2]. In order to reduce the need for supports, several methods have been proposed and developed, such as optimising the build orientation [16], segmenting the component into smaller support-free structures [17] and optimising the design of the support structure's itself [15].

In technologies and build setups where supports are imperative, their removal must be planned ahead. Often, these can be situated in difficult-to-access regions of the workpiece, and features such as access holes, which may be eventually plugged, must be designed to allow the support's removal [2] (in the case of non-metallic methods, such as Vat polymerisation, these can also function as drain holes for trapped liquid resin) [2].

Topology optimisation

Due to the geometrical freedom allowed through AM processes, several methods have been developed to procedural optimise a structure according to certain user-controlled principles: these methods fit in the category of optimisation design [3]. There are three main categories in which optimisation design fits in: *(i) size optimisation*, which primarily varies the area or volume of a certain part; *(ii) shape optimisation*, which alters the specified geometrical parameters of an already established shape; *(iii) topology optimisation* changes structural topology while satisfying the constraints of the problem [3]. In Figures 2.3a-2.3f, a schematic representation of these methods is displayed. Out of all the mentioned methods, topology optimisation presents the greatest potential [18], finding the optimal distribution of material (and lack thereof) within the design space while attempting to maintain structural integrity [18].

Topology optimisation operates within a design space, in which the design variables are chosen: through these variables, functions can be established and subjected to restraints. An objective function that guides the optimisation process through a series of iterations is also defined, and the optimisation process is complete when this objective is fulfilled [3]. Moreover, there may be additional geometric restrictions applied, such as *frozen* areas, where the volume remains untouched, as well as final topology symmetry requirements. The general workflow of a topology optimisation process is schematically represented in Figure 2.4 for a static, structural case.

The synergy of these methods and AM technologies arises precisely in its ability to produce optimised components, despite their remarkable complexity. Therefore, it is difficult to talk about the present day state of AM without speaking about optimisation, and more specifically topology optimisation.

2.1.5 Metallic AM processes

As the objective of this thesis focuses on simulating the manufacturing process through metallic AM, only methods relevant to this solution will be analysed, despite the fact that the world of AM extends far beyond the mentioned processes. In this Section, Direct Energy Deposition and Powder Bed Fusion are described, providing greater detail for Laser Powder Bed Fusion (LPBF), since the studied specimens and simulations are manufactured through this process.

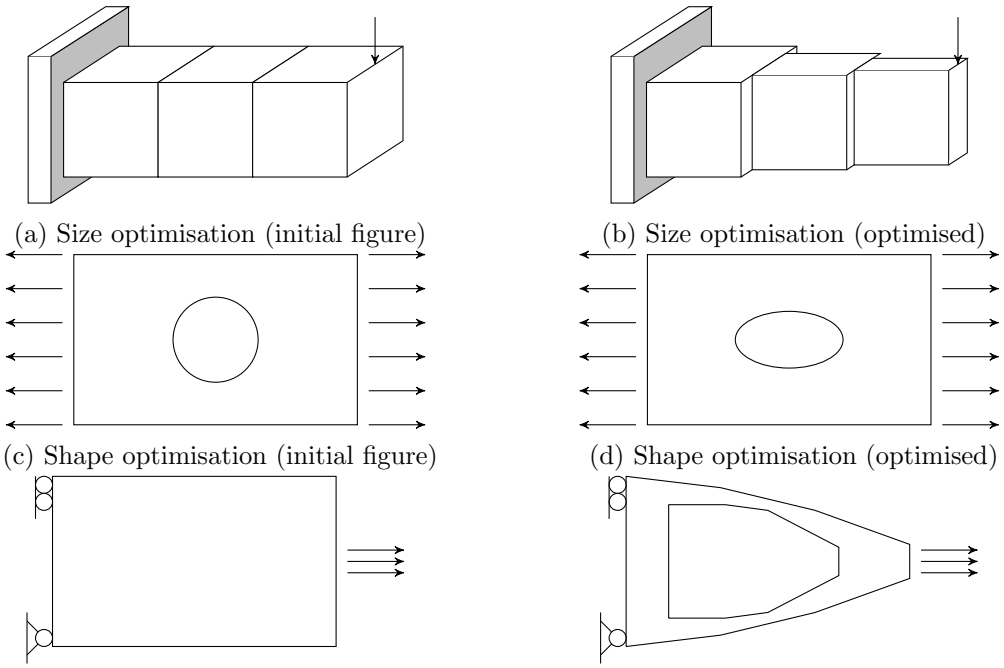

(a) Size optimisation (initial figure)

(b) Size optimisation (optimised)

(c) Shape optimisation (initial figure)

(d) Shape optimisation (optimised)

(e) Topology optimisation (initial figure)

(f) Topology optimisation (optimised)

Figure 2.3: Schematic representation of structural improvement through size, shape and topology optimisation.

Direct Energy Deposition

Direct Energy Deposition (DED) is a process characterised by the simultaneous deposition of material and its fusion into a layer. A schematic representation of the DED process can be found in Figure 2.5. It is common for the powder to be deposited alongside the introduction of inert gases, to minimise the oxidation rate [19], and there can be multiple nozzles ejecting material at the same time [20].

When compared to Powder Bed Fusion (PBF) processes, DED generally requires larger powder sizes and, therefore, higher energy densities [21], which consequently means the builds are printed faster. Another difference comes from the virtually non-existent use of support structures employed in DED, a practice common in PBF [22].

Powder Bed Fusion

Powder Bed Fusion processes were among the first commercialised AM processes [2]. All PBF methods include a heat source responsible for the induced fusion between the powder particles, a system to control the powder fusion to an assign region, as well as a mechanism that guarantees the smoothing of layers [2].

Powder Bed Fusion can be divided into two different types: Selective Laser Melting, also known as Laser Powder Bed Fusion, and Electron Beam Melting (EBM): the difference between them lies in the heat source, as the former uses a laser and the latter an electron beam [23]. LPBF functions according to the described workflow of a generic AM process, introduced in the beginning of this Section, in which the component's CAD file is sliced into layers, positioned within the powder bed, machine settings are defined, and the build process initialises; then, the component is created by the successive spread of powder, and its fusion into a coherent layer through a heat source, subsequently solidifying until the

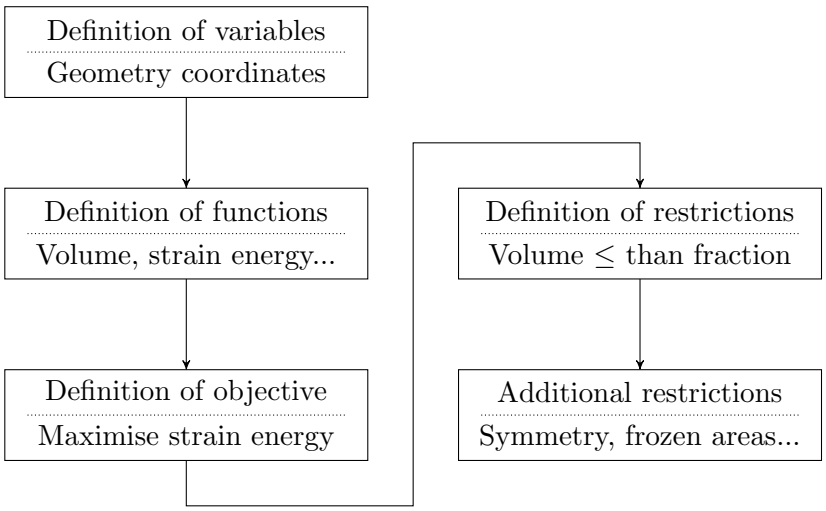

Figure 2.4: Representation of a topology optimisation workflow for a structural example.

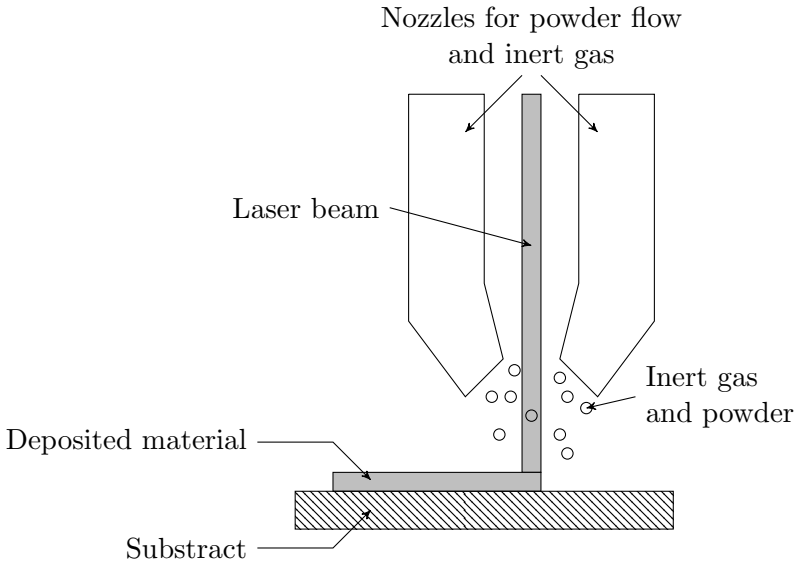

Figure 2.5: Schematic representation of DED process (adapted from [22]).

process is repeated [23]. EBM required two different stages to process the powder, firstly lightly sintering each layer of powder to prevent electrostatic charging and repulsion of powder particles, with complete fusion occurring in a second beam pass [23]. Additionally, EBM must be employed in a vacuum.

2.1.6 LPBF process parameters

The process parameters of any technological process play a crucial role on the final output it produces. The main process inputs that characterise the LPBF process can be subdivided intro four main categories [2]:

- Laser-related: laser power, spot size, pulse duration, pulse frequency;
- Scan-related: scan speed, scan spacing, scan pattern;

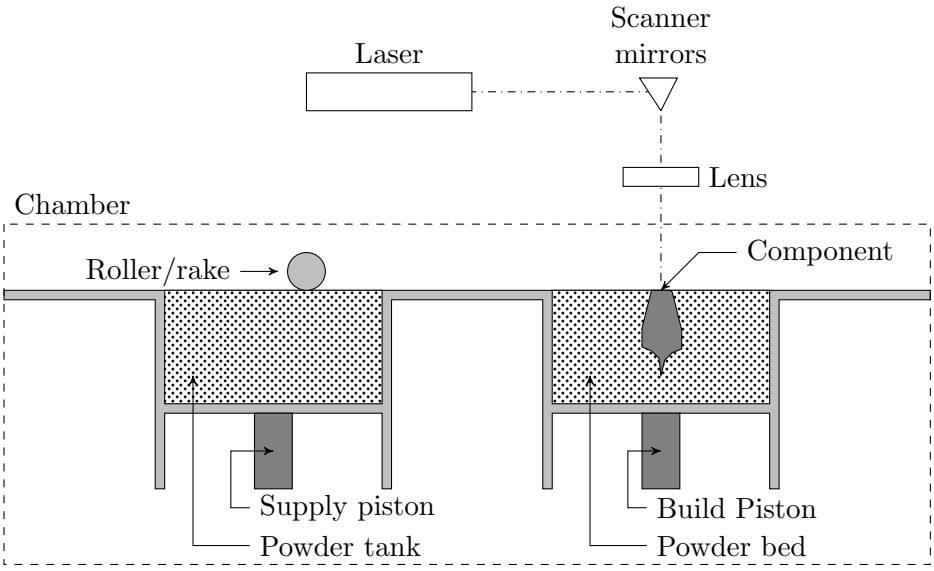

Figure 2.6: Typical LPBF machine setup (adapted from [13]).

- Powder-related: Particle shape, size and distribution, powder bed density, layer thickness, material properties;
- Temperature-related: Powder bed temperature, powder feeder temperature, temperature homogeneity.

The scanning pattern generally involves two different modes: *contour* mode and *fill* mode. The former is responsible for the outline and it is mostly done for dimensional control reasons, while the latter fills the actual section area of the item. In some cases, it is convenient for the fill to be subdivided into different zones with their own filling directions in order to prevent preferential residual stress directions.

The spatial configuration of the parts within the powder bed also affects the quality of the final part: the changes in laser path may provoke distortions that compromise the completion of the piece [2].

Powder size, shape and distribution across the powder bed strongly affect how the powder absorbs the energy provided by the laser; additionally, powder bed temperature, laser power, scan speed and remaining machine settings must be adjusted to improve the part's precision, surface finish, mechanical properties and at the speed at which the part was manufactured [2].

2.1.7 Mechanical considerations

Residual stresses

Residual stresses develop and remain present within a workpiece at equilibrium after all forms of technological processes have been performed [12]. They are of crucial importance in components made through AM, as a layer undergoes multiple thermal cycles during the deposition stages, characterised by rapid heating and cooling rates [10].

In parts manufactured by AM, residual stresses appear through two different phenomena: *(i) temperature gradient* mechanism, in which the upper layers are subjected to steep heat gradients owing to the laser, causing rapid expansion that induces compressive strains until the yield strength is reached; then, as the layer is starting to cool, the plastically

compressed layers start to shrink, inducing tensile strain; *(ii) cool-down phase*, where the underlying solid material prevents the shrinkage of the top layer, inducing tensile stresses [24]. Both of these stages are schematically shown in Figures 2.7a-2.7b.

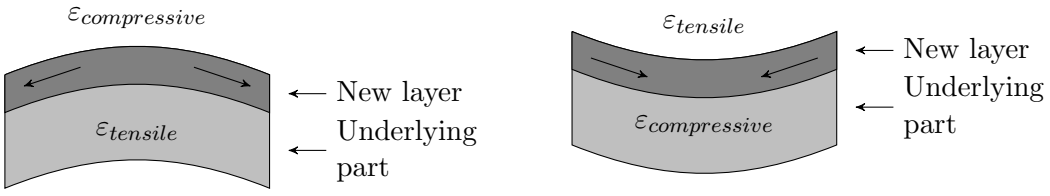

(a) Material expansion

(b) Material contraction

Figure 2.7: Basic mechanisms of stress and plastic deformation evolution (adapted from [24]).

Due to the anisotropic and non-instantaneous nature of material heating/cooling, allowing sections to behave independently usually lead to in-plane stresses to be of larger magnitudes than out-of-plane stress [12].

Although residual stresses can be improved through heat treatments, its subsequent excessive distortion can be proved too harmful and lead to failure; furthermore, there is an incentive to reduce the amount of post-processing a component built through AM needs to be subjected to, as it further raises the monetary cost on an already expensive process [12]. It is worth mentioning that residual stress mechanisms in the additive manufacturing process and welding processes are largely the same [25].

Residual stresses can be subdivided into different types: *(i) type I*, which are the origin of the bulk of fatigue research, which are macroscopic-scale defects responsible for the geometric distortions on a component; *(ii) type II*, acting on an individual grain scale, that happen due to microstructural defects such as differences in slip behaviour between grains; *(iii) type III*, being residual stresses originated at an atomic scale [12].

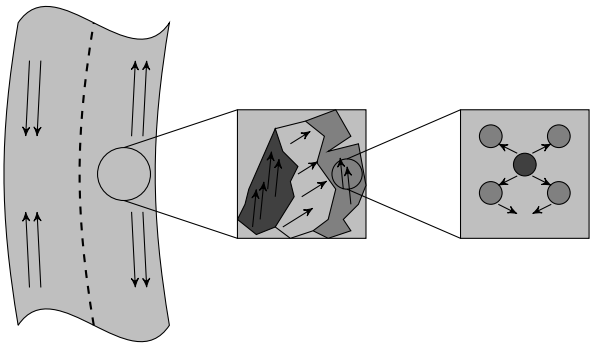

Figure 2.8: Examples of residual stress types into three categories.

A topic of equal importance in the study of additive manufacturing processes and further improvements is the ways information is extracted from existing physical models, that guides the engineer into making important conclusions about the specimen. There is a considerable amount of methods used for the measurement of residual stresses, but only three are going to be mentioned to their close ties to the work developed, namely neutron diffraction, X-ray diffraction and image correlation.

2.2 Finite Element Method

2.2.1 Introduction

The Finite Element Method (FEM) is a mathematical framework used to provide approximate solutions to differential equations [26]; as with many other methods, it grew in interest with the increase and vulgarisation of computational methods capable of handling the calculation workload that would otherwise be highly time-consuming or impossible, even though it is by no means a novelty in the world of mathematics.

While analytical methods provide "exact" solutions to a certain equation, numerical methods grant approximate solutions usually by relaxing specific considerations, or by transforming the governing mathematical expressions into a set of algebraic equations, dependent on a finite set of parameters [26].

Additionally, FEM requires a discretisation process that subdivides the problem's domain into several parts or elements, whose behaviour is characterised by a finite set of parameters [27] that simultaneously describe the particular element and the whole system's behaviour.

The particular way the elements are mapped to the problem's geometry is named a *mesh*. Meshes can be finer or coarser, influencing the accuracy and the convergence of the problem's solution [26].

Through a variational principle, the initial equation that describes the problem at hand is transformed into its *weak form*: a broader mathematical statement that decreases the order of the partial differential equation by multiplying it by a test function and integrating it over the domain, transforming a differential formulation into an integral one [28]. These test functions are then replaced by shape functions that interpolate the set of nodal variables, which constitute the unknowns of the problem.

These interpolating functions are named *shape functions*, which are mathematical expressions that map the nodal values into the problem's domain: these can be defined for the whole geometry - such is the case in *Rayleigh-Ritz* or *Galerkin*'s methods - or for each individual element, as is the case for FEM. A schematic representation of the computational model's structure of a typical finite element method solver is presented in Figure 2.9.

Shape functions need to fulfil two mathematical conditions: *(i):* they must be defined unitary at their respective node, and zero in all remaining nodes; *(ii):* the sum of all shape functions must equal to the unit in every point of the domain. These two realities are mathematically represented in Equations (2.1) and (2.2), respectively [27]

$$\psi_j\left(\xi_i, \eta_i, \zeta_i\right) = \begin{cases} 1, & \text{if } i = j \\ 0, & \text{if } i \neq j \end{cases} \tag{2.1}$$

$$\sum_{j=1}^{N_n} \psi_j\left(\xi_i, \eta_i, \zeta_i\right) = 1, \ \forall\ i \in \Omega_e \tag{2.2}$$

, where ψ is a shape function, the subscript j is the node at which the shape function is defined to be unitary, the subscript i is a generic node, N_n is the total number of nodes and Ω_e is the shape function's domain; ξ, η and ζ are local coordinates.

Shape functions and element types are intrinsically linked, as higher order shape functions generally require additional nodes for appropriate definition. The finite element periodic table [29] is a graphical representation that unites used elements and their equivalent degrees of freedom, weight functions, notation and shape, allowing for easy visualisation

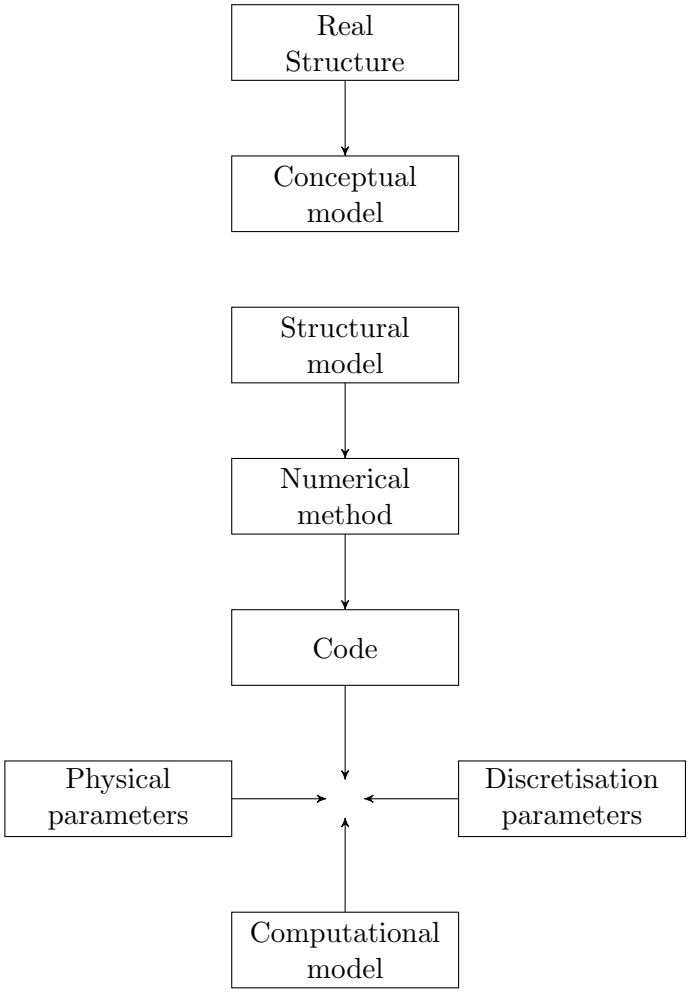

Figure 2.9: Schematic representation of the Finite Element Method computational model's structure

of the existing elements and their respective applications. Furthermore, there has been an increase in *meshless* or *mesh-free* methods, where nodal parameters are interpolated through areas of influence, allowing for greater flexibility at the cost of increased computing power [30]. More on the subject of discretisation techniques can be explored in the literature [26, 31].

2.2.2 FEM within AM

The finite element method has been progressively used for analysing the additive manufacturing process, from the interaction between the heat source and the material, to the subsequent heat transfer of the melt pool to the solidified part, attempting to accurately predict microstructural changes and defects, to the final distortions, stresses and strains related to the completed part. Even by modern standards, the mathematical treatment of the AM process, as a whole, is too complex to realistically model each interaction, and therefore compromises between reality and the physical considerations must be adopted.

Considerable research has been conducted within the context of modelling the process of LPBF, and it can be categorised into two main focuses: *(i) microstructure prediction*, which as the name implies, apply thermal loads to analyse metallurgical phenomena in the

micro and meso scales, exploring type II and type III residual stresses. These simulations therefore deal with phase transitions, micro defects, powder wetting/dewetting and molten pool dynamics. Examples of research in this area are the prediction of microstructure, hardness, residual stresses and strain in parts produced by LPBF by Yang et al. (2018) [32]; Kelly (2004) developed a model for multilayered Ti-6Al-4V deposits in the laser metal deposition process [33]; Smith et al. (2016) analysed microstructural development, thermal deformation, thermal stress and residual stresses through computational phase diagram thermodynamics [34]; *(ii) distortion*, which centres on macroscopic phenomena regarding layer-by-layer solidification and subsequent cooling often at the expense of laser-powder interactions and scanning trajectories. This method will be the one applied in this research for distortion prediction and residual stress calculation. Cao et al. (2016) developed a coupled thermomechanical model to study the effect of preheating on the final distortion of electron beam additive manufactured plates [35]; Mukherjee et al. (2017) [36] modelled a three dimensional heat transfer model to study the influence of scanning speed and layer height in the final model; Ueda (1989) implemented a discretisation method to substitute a thermal simulation step with an equivalent plastic strain vector [37], a method that became known as *inherent strain*, later adapted to AM by Keller et al. (2014) [38], mentioned in the following subsection. The interaction between these focuses - microscale, mesoscale and macroscale - is schematically shown in Figure 2.10.

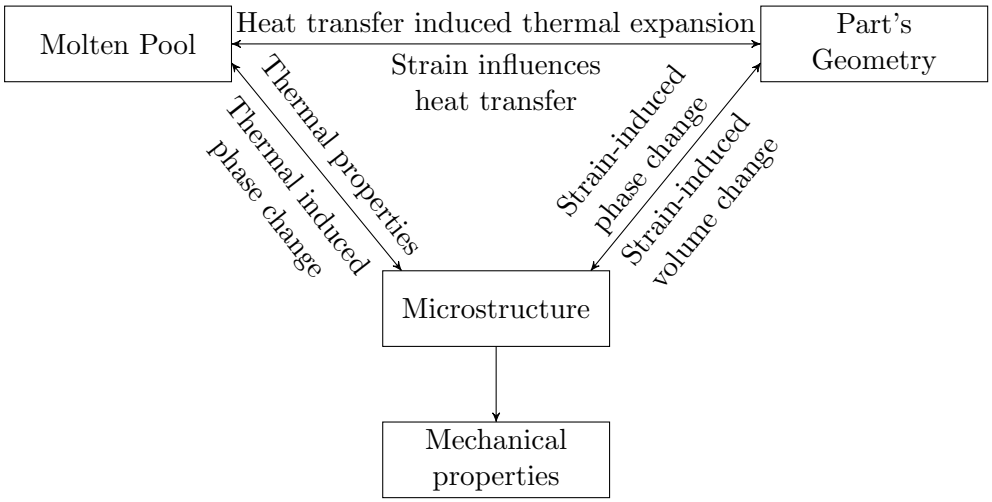

Figure 2.10: Interaction between phenomena in the LPBF process (adapted from [11]).

In the following paragraphs, the different formulations regarding the AM physical and mathematical model are discussed, along with fundamental equations and FEM implementation in commercial software packages.

Inherent strain

As previously mentioned, inherent strain is the name given to a numerical simulation technique which was first implemented for a faster, less computationally intensive method to determine the distortion of welded structures [39]. There are two ways to apply this method: the *(thermal strain* method, which is based on a purely thermal analysis with the same boundary conditions as the real model is conducted on a small geometry. The objective is determining the plastic strain this component experiences, and using it as an analogous to the actual workpiece geometry: orthotropic thermal expansions are calculated based on the plastic strain and subsequently applied to the whole model [39]. This

method comes with its problems, as pointed out by Bugatti et al. (2018), who concludes that this method becomes increasingly flawed as its geometry becomes more complex and requires further calibration [40]. The equations formulated by Ueda (1989) to allow the computation of residual stress via the plastic strain vector within FEM are displayed in Equations (2.3)-(2.7)

$$\boldsymbol{f} = \int_V \boldsymbol{B}^T \boldsymbol{D} \boldsymbol{\varepsilon}_{inh} dV \tag{2.3}$$

$$\boldsymbol{u} = \boldsymbol{K}^{-1} \boldsymbol{f} \tag{2.4}$$

$$\boldsymbol{\varepsilon}_{tot} = \boldsymbol{B} \boldsymbol{u} \tag{2.5}$$

$$\boldsymbol{\varepsilon}_e = \boldsymbol{\varepsilon}_{tot} - \boldsymbol{\varepsilon}_{inh} \tag{2.6}$$

$$\boldsymbol{\sigma} = \boldsymbol{D} \boldsymbol{\varepsilon}_e \tag{2.7}$$

in which $\boldsymbol{f}$ is the nodal force vector, $\boldsymbol{B}$ the deformation matrix, $\boldsymbol{D}$ the constitutive matrix, $\boldsymbol{u}$ the displacement vector, $\boldsymbol{K}$ the stiffness matrix, $\boldsymbol{\sigma}$ the nodal stress vector and ε_{tot}, ε_e and ε_{inh} are the total, inherent and elastic strain [37].

The second method of performing an inherent strain analysis is through the *strain scaling factor*, which aims at being more tailored to a machine's settings through a factor named Strain Scaling Factor SSF. This constitutes the simplest and fastest simulation by assuming a predefined isotropic plastic strain field in each voxel element [41], although software packages such as ANSYS allow the definition of additional Anisotropic Strain Coefficients (ASCs) which significantly improve the accuracy of the simulation [42]. The calculation of the inherent strain vector is shown in Equation (2.8):

$$\boldsymbol{\varepsilon}_{inh} = SSF \cdot \frac{\sigma_y}{E} \tag{2.8}$$

$\boldsymbol{\varepsilon_{inh}}$ is the inherent strain vector, SSF is the strain scaling factor, σ_y is the yield strength and E is the Young's modulus.

It is important to note that this method cannot be considered a thermal-structural analysis method, although an initial thermal analysis can be used to determine the inherent strain vector $\boldsymbol{\varepsilon}_{inh}$. This method can, nonetheless, provide an early estimate of the residual stress field for a component without requiring temperature-dependent variables [41].

Thermal analysis

All modelling procedures for AM simulation consist of non-linear thermomechanical analysis [39], and can be subdivided into two main categories: *fully coupled* thermomechanical simulations and *weakly coupled* thermomechanical simulations. The former are characterised by a structural assessment after every thermal analysis step. This implies the geometry is updated at every time step and its displacements influence the temperature field of the workpiece [39]. The latter are defined by a complete thermal simulation before any structural analysis, meaning that the thermal field is independent of the mechanical response of the component [39]. The weakly coupled thermomechanical simulation is the usual method used in commercial simulation packages for its lower computational intensity for acceptable results [43].

The heat transfer analysis is conducted through the conservation of energy equation, shown in Equation (2.9)

$$Q\left(x,y,z,t\right) - \rho c_p \frac{\partial T}{\partial t} + \nabla \left[k\left(T\right) \cdot T\left(x,y,z,t\right)\right] = 0 \tag{2.9}$$

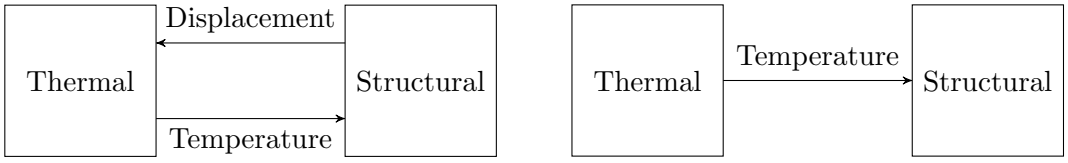

(a) Fully Coupled (b) Weakly Coupled

Figure 2.11: Schematic representation of thermomechanical coupling.

where Q represents the body heat source, ρ the material density, c_p the specific heat, T the temperature and k the thermal conduction coefficient. The body heat source Q, a function of both time and spacial coordinates, contains the thermal boundary conditions including losses through conduction, convection and radiation, and additionally could include the laser's heat distribution (usual descriptions for laser heat flux are Gaussian distributions or Goldak's double ellipsoidal model [8]). As this increases the problem's complexity, generally commercial software packages establish a new layer to be at melting temperature.

With the temperature history established, the nodal temperatures are applied as thermal loads, satisfying Hooke's law and the equilibrium condition for solid mechanics [39], allowing the determination of the displacement field, although hardening laws are too included to account for plastic behaviour during the process [43]

$$\nabla \boldsymbol{\sigma} = 0 \tag{2.10}$$

$$\sigma = \boldsymbol{C}\left(\boldsymbol{\varepsilon}_{tot} - \boldsymbol{\varepsilon}_p - \boldsymbol{\varepsilon}_T\right) \tag{2.11}$$

where $\boldsymbol{C}$ is the fourth-order elastic stiffness matrix and $\boldsymbol{\varepsilon}_{tot}$, $\boldsymbol{\varepsilon}_p$ and $\boldsymbol{\varepsilon}_T$ are the total, plastic and thermal strain tensors, respectively. Considering the temperatures and the nature of the problem, both temperature-dependent properties and a well-defined plasticity law are encouraged for better results [39].

Activation methods

As explained in the beginning of this section, FEM requires a mesh responsible for both mapping the geometry's coordinates into nodes and interpolating the nodal variables across their domain. However, in the case of AM in which the material is incrementally deposited, not all nodes are initially active, hence needing an algorithm responsible for nodal activation when its respective layer has been created. There are three well-established techniques to ensure this process: *quiet elements* activation, *inactive elements* activation and *hybrid* activation.

The first method - quiet elements activation - creates the entire mesh before the simulation begins: however, the nodes pertaining to non-deposited material see their properties scaled down in a manner that their influence is negligible [39]. In the inactive elements method, non-deposited elements are added at an appropriate step, requiring iterative remeshing and node renumbering. This comes at the cost of computational power, but it solves the problem of ill-conditioned stiffness matrices that the quiet elements introduce. The third method attempts to solve both problems by generating a mesh at each deposited layer, and scalling down the properties of the inactive nodes until a heat source interacts with them [44].

Commercial software packages

Several software developers have created commercial modules especially crafted with additive manufacturing in mind: Additive Works by Amphyon, Additive Print and Suite by ANSYS, Netfabb by Autodesk, Simufact by MSC, Simcentre 3D Additive Manufacturing by Siemens, 3DExperience by Dassault Systemes and ESI Additive Manufacturing by ESI.

These packages are in different stages of development and offer different functionalities, but they are mostly centred around distortion simulations for metallic AM. Some packages also possess topology optimisation modules, an area of numerical simulations that is intrinsically related to AM due to its complexity and otherwise impossibility to produce by other processes [2]. A brief description of the mentioned softwares is given next:

- Additive Works by Amphyon: this package offers functionalities aimed at optimising a part's build process according to the customer's needs, such as minimising build time, support creation and distortion management. One of its main selling points is the adaption of the .STL file via deformation calculation;
- Additive Manufacturing Suite by ANSYS: ANSYS has produced two solutions for AM, with one being an addition to the traditional ANSYS workbench that introduces the necessary modules to simulate the LPBF process, and the other one being a stand-alone product intended for tweaking build process variables;
- Netfabb by Autodesk: a complete package capable of residual stress determination, alongside support calculation, lack-of-fusion spots and failure prediction. This package allows the simulation of DED processes, besides LPBF;
- Simufact by MSC: a package that allows the determination of residual stresses during the build process. This software allows the simulation of diverse laser and deposition processes, and it promises the addition of binder jetting methods in the future;
- Simcenter by Siemens: a solution that offers deformation and distortion calculation for metallic AM processes based on laser heat transfer, through a weakly-coupled thermomechanical method;
- 3DEXPERIENCE by Dassault Systemes: a package capable of macroscopic distortion calculation, as well as preliminary fatigue analysis that provide information regarding crack initiation and propagation;
- Additive Manufacturing by ESI: a software that processes a distortion module that allows the determination of residual stresses, as well as a heat treatment module aimed at stress relaxation calculation.

In this thesis, two software packages were used to conduct the proposed simulations. Their names, however, remained undisclosed due to non-disclosure agreements, and were named Software #1 and Software #2. Their respective methods, simulation parameters and additional information important to their understanding are mentioned in the following subsections.

Software #1

Software #1 does not perform a weakly-coupled thermal analysis, as it avoids performing a full thermal simulation by instead solving the initial thermal problem through setting the deposited layer's temperature to the material's melting temperature. The previous layer

to the one being deposited is considered to be at chamber temperature, a user defined temperature that is maintained as a thermal boundary condition throughout the build process. Previous versions of the program allowed the definition of a gradual cooling law, in which a user-controlled number of layers beneath the deposited one could re-heat and undergo another thermal cycle, but this option was not explored, meaning that solidified layers do not re-heat. The software then applies the governing differential equations to the deposited layer, until it cools to the chamber temperature and subsequent distortions are calculated, and the process is repeated for the following layer of material until the geometry is fulfilled.

This software presents three distinct simulation stages: the *build* stage, consisting of the material's deposition until the final geometry is achieved; *release* stage, in which the baseplate is removed from the machine; *removal* stage, where the workpiece is detached from the baseplate. Figure 2.12 schematically displays these three simulation stages.

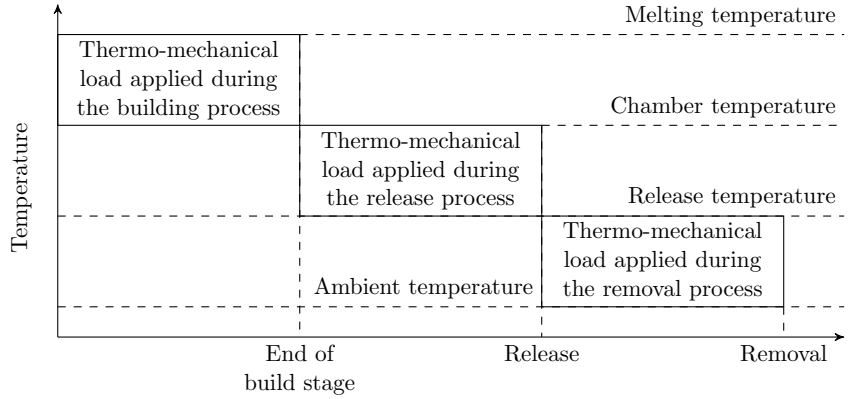

Figure 2.12: Software #1's simulation stages.

Regarding meshing, Software #1 allows the definition of the mesh size in the three directions: the *mesh fineness* parameter defines the in-plane element size, while the *lumping factor* characterises the out-of-plane dimension by increasing the size of the numerical layer by its' value. An example would be a workpiece with layer thickness of 5 µm and a lumping factor of 10, meaning the element height would become 50 µm. The software allows both conform and non-conform meshing, although the latter was not explored in this research work.

This software features an internal library with already defined properties for most widely used materials in the AM world, although its temperature dependent properties aren't available on its distortion module, which greatly hinders the accuracy of results.

Software #2

Software #2 is based on a weakly-coupled thermomechanical formulation, although the user has greater control over the temperatures involved: the gas, preheat, powder and cooldown temperatures are all user-controlled, as well as the thermal boundary conditions, which can be temperature- or convection-based and applied to different areas of the component. Additionally, the convection coefficient of the gas and the powder are also user-defined properties.

Software #2's standard settings allow layer re-heating after it has been deposited, and the temperature and nodal variable histories can be retrieved during post-processing, a valuable asset used several times in this research. Figure **??** aims at displaying how

Software #2 solves the FEM problem, with the respective temperatures and build stages.

The geometry could be meshed either by layered cubic hexahedral or tetrahedral elements, although only the latter allows out-of-plane dimension definition. In either case, the out-of-plane length behaves the same way as Software #1's lumping factor, in which a set of physical layers is lumped into one numerical layer and its thermal history calculated which later serves as thermal load in the structural analysis [41].

Software #2 features a considerable amount of temperature-dependent properties for materials that are usually used in AM.

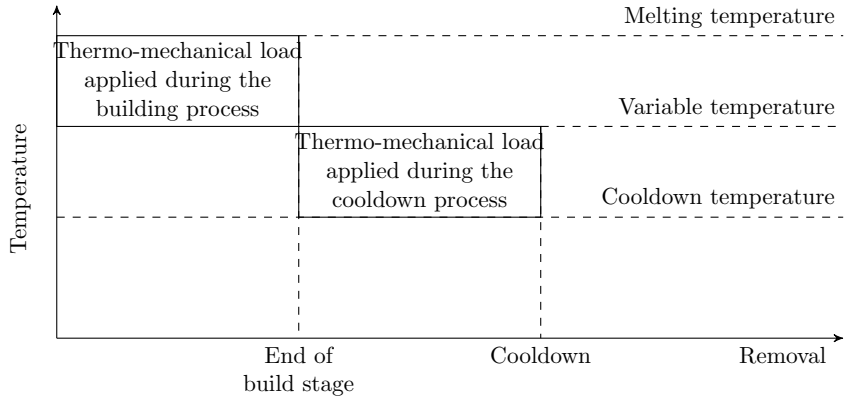

Figure 2.13: Software #2's simulation stages

Chapter 3

Simulation Details and Methods

As aforementioned in the introductory section of this research work, this thesis' main goal is the establishment of a numerical framework within an existing FEM commercial package to reasonably predict distortions and residual stresses in parts produced by additive manufacturing, and more particularly by LPBF. In this Chapter, the performed simulations are explained and presented alongside their defining parameters and context. Relevant decisions regarding the simulation's setup are shown, observations are made, although results will be presented in Chapter 4 and concluding remarks are found in Chapter 5.

The objective of this Chapter is the exposition of all used parts and materials in both software packages, as well as the outline of all simulation parameters and objectives, so that the reader could replicate these results with ease. Therefore, this Chapter is divided into three main parts:

1. Physical specimens - Section 3.1 - In this Section, the three physical specimens in which simulations were conducted are introduced, along with their respective geometries and manufacturing processes;

2. Material definition - Section 3.2 - All of the different materials used in the numerical studies are introduced, as well as their mechanical, thermal and physical properties;

3. Simulations - Sections 3.3-3.6 - Each individual simulation *group* (meaning one or more numerical studies that share the same purpose) is detailed, in which their objectives, geometries, materials and software packages are specified.

The software packages that were used remain undisclosed to protect non-disclosure agreements in place and are named Software #1 and Software #2, as mentioned in Subsection 2.2.2.

3.1 Physical specimens

3.1.1 Introduction

There are three different specimens in which simulations were conducted: a quadrangular right prism ($50\,\text{mm} \times 10\,\text{mm} \times 20\,\text{mm}$), found in Figure 3.1a which will be named *prism* for practicality's sake, and two components based on the same geometry - an AM benchmark piece - represented in Figure 3.1b, which from now on will be referred to as *benchmark bridges*.

The latter's dimensions have been proposed by the United State's National Institute of Standards and Technology (NIST), which documented the entire process and compiled it in

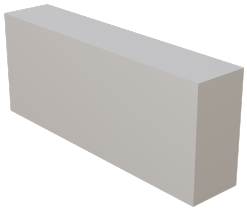

(a) 50 mm × 10 mm × 20 mm prism

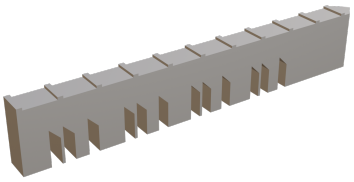

(b) Benchmark bridge

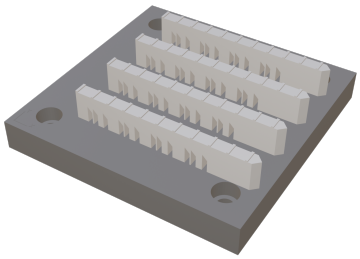

(c) Benchmark bridges printed on the same baseplate

Figure 3.1: Schematic renders pertaining to the components subjected to study.

a small report [45]. This document's main goal is to thoroughly describe the manufacturing process of the benchmark bridges, whose design is specially conceptualised, as the report puts it, "(...) to investigate residual stress within the structure, the part distortion which occurs after a section of the part is cut via Wire Electrical Discharge Machining (WEDM), and the microstructures that develop in geometrically distinct locations in the part" [45].

Due to INEGI's participation in the *Add.Strength* project, a component with the same geometry as these benchmark bridges, but different manufacturing parameters, is in its possession. Information regarding the manufacturing process of INEGI's bridges is detailed in Subsection 3.1.3, while the process parameters of NIST's bridges is presented in Subsection 3.1.4. It is important to highlight the fact that although their geometries are the same, their manufacturing process differ; despite this fact, using this component as a study subject maintains its relevance due to its complexity, underlining distortions in the build stage.

Each of the component's manufacturing processes are detailed in Subsections 3.1.2, 3.1.3 and 3.1.4.

3.1.2 Prism

As the name implies, the prism is a simple cuboid construction, whose dimensions are shown in Figure 3.2. Its simple geometry makes it the ideal component to use in most parametric and convergence simulations for several reasons: *(i) meshing,* as the prism's simple geometry allows for simple and computationally expedient discretisation, with both coarser and finer inputs being able to accurately describe it; *(ii) lack of support structures,* in which the usual concerns that require support geometries - providing additional thermal sinks and structural support to hanging or angles features [2] - are not present; *(iii) avoids large thermal boundaries*, in which small cross-section areas are deposited in the early stages of the build; *(iv) highlights parametric variables,* as the objective of parametric simulations is emphasising a variable's influence in the residual stress field, minimising

external errors induced by unwanted factors.

Regarding the physical specimen possessed by INEGI, its material is maraging steel, a precipitation-hardened steel that offers an unusual combination of high tensile strength and high fatigue strength, making it a valuable choice for demanding applications [5].

This prism's manufacturing process abides by the variables presented in Table 3.1, pertaining to the machine settings. The scanning strategy of the prism consists of a striped method (also called island scanning): individual stripes with repeating orientation every three layers, implying patterns with a lag of 120° between them.

The sample is still attached to the baseplate to avoid added complexity in the analysis. The experimental values extracted from this prism are detailed in Chapter 4, in Figure 4.1.

Table 3.1: Some machine settings used in the AM process of the prism.

Layer thickness	**Laser Power**	**Scan Speed**	**Laser Diameter**	**Hatch Space**
0.040 mm	400.0 W	860.0 mm s^{-1}	0.175 mm	0.095 mm

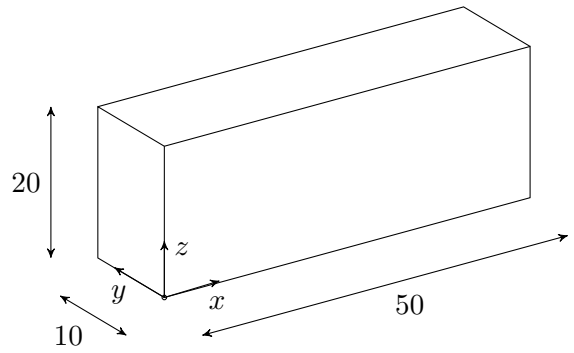

Figure 3.2: Prism dimensions and coordinate system (dimensions in millimetres).

3.1.3 INEGI's benchmark bridges

The benchmark bridge component is a bridge structure in which a total of twelve legs - four repetitions of three legs with different widths - is supporting a bulk volume measuring $75 \times 5 \times 5$ mm, with additional small prominences measuring $1 \times 5 \times 0.5$ mm. At one of the extremities, the structure features a 2.5 mm chamfer. The dimensions of the component are given by Figure 3.3a.

One of the main obstacles in the printing process of the benchmark bridge and its simulation are the benchmark bridge's very narrow section areas: the smallest bridge *leg* is only 0.5 mm thick, which means a relatively fine mesh is needed to accurately define this particular region. Figure 3.3b attempts to highlight this detail.

The benchmark bridges were manufactured by *EROFIO*, a company based in Leiria, Portugal, specialised in thermoplastic injection and manufacturing solutions, according to the following considerations:

- Workpieces were printed in numerical order, from number one (#1) to number four (#4), as shown in Figure 3.4;
- None of the four bridges is contoured nor post-processed;

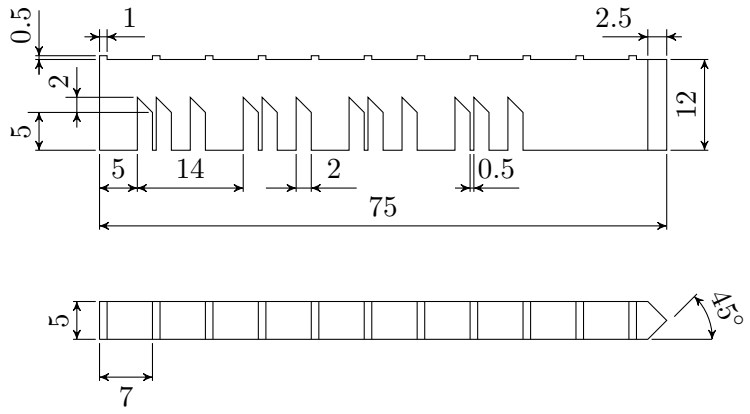

(a) Benchmark bridge (dimensions in millimetres)

(b) Narrow details in benchmark bridge's legs

Figure 3.3: Dimensional properties and geometrical details regarding thin legs and slanted corners pertaining to the benchmark bridges.

- Each individual bridge's first layer is initiated from bottom to top, from left to right;
- Bridges #1 and #2 were printed using a continuous line strategy, where even layers were vertically scanned, starting from the point closer to the origin of the coordinate system, from bottom to top, and uneven layers were scanned horizontally starting from the point closer to the origin of the coordinate system, from left to right, as shown in Figures 3.5a, 3.5b;
- Bridges #3 and #4 were printed using a striped method, meaning that each layer was subdivided into multiple stripes that were constructed sequentially. Even layers were horizontally scanned, starting from the point closer to the origin of the coordinate system, from left to right, and uneven layers were scanned vertically, starting from the point closer to the origin of the coordinate system, from top to bottom, as shown in Figures 3.5c, 3.5d;
- The remaining parameters are shared across all bridges, and are further displayed in Table 3.2;
- All bridges are made of maraging steel, while the baseplate is made of a carbon steel.

Table 3.2: Additional machine settings used in the AM process of the benchmark bridges.

Layer thickness	**Laser Power**	**Scan Speed**	**Laser Diameter**	**Hatch Space**
0.030 mm	200.0 W	950.0 mm s^{-1}	0.175 mm	0.110 mm

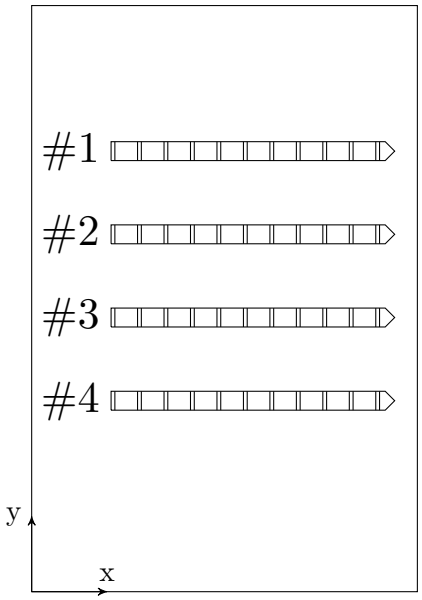

Figure 3.4: Benchmark bridges' layout within the baseplate, numeration and coordinate system.

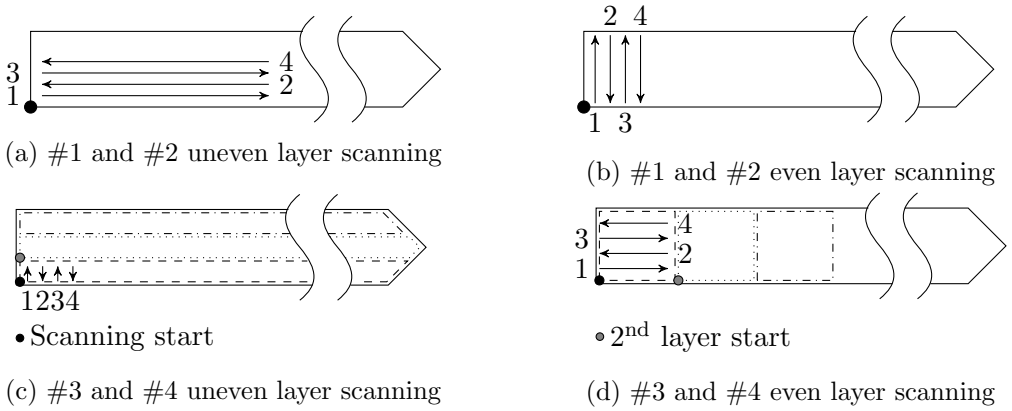

(a) #1 and #2 uneven layer scanning

(b) #1 and #2 even layer scanning

(c) #3 and #4 uneven layer scanning

(d) #3 and #4 even layer scanning

Figure 3.5: Scanning strategies of the benchmark bridges, printed by *EROFIO*.

3.1.4 NIST's benchmark bridges

Simulations were also conducted with the simulation parameters pertaining to the NIST benchmark, as explained in Subsection 3.6.

Due to the fact that the document details the complete manufacturing process of the workpiece and its respective parameters so thoroughly - total number of layers, layer thickness, hatch spacing, laser speed, laser power, time between scans, powder geometry, amongst other parameters outlined in the document - it is an ideal piece for third parties to attempt to replicate its production. Adding to the process explanation, NIST shares the experimental measurements regarding the component's distortions, strains and residual stresses.

3.2 Material definition

3.2.1 Introduction

There are several materials used in the proposed simulations, and their definition across multiple finite element solutions is important to clarify.

It is noteworthy to highlight the fact that the used material in a conducted simulation does not necessarily match the existing physical component's material, but rather chosen according to a particular simulation's goal. The outline of the conducted simulations, alongside their parameters and goals, is found in Sections 3.3-3.6.

3.2.2 Software #1

316L Stainless Steel In most convergence and parametric simulations, 316L stainless steel is used, and it constitutes a dominant material in metallic AM's universe. It is a version of the regular 316 stainless steel, but with lower levels of carbon and sulphur [46]. The lower carbon percentages result in extra resistance against carbide precipitation at grain boundaries, a problem aggravated when the material is heated to temperatures of around $500\,°C - 800\,°C$: at these temperatures, chromium precipitates in grain boundaries, depleting certain areas that suddenly become corrosion prone, a problem molybdenum is known to hinder [47].

Austenitic stainless steels are generally favoured over other austenitic varieties as a structural material for two main reasons: *(i)* they display better corrosion resistance, and *(ii)* they possess superior mechanical properties both at high and low temperatures [48]; furthermore, austenitic steel has the advantage of not phase changing in the heating process [48]. This brings several advantages, mainly meaning that no additional energy is wasted in phase transformations during the multiple heating cycles, ensuring that specific cooling rates to achieve a certain phase configuration are not an immediate concern.

The mechanical, thermal and physical properties of the used 316L stainless steel match the defined material in the internal library of Software #1's Additive Manufacturing Suite, and are shown in Table 3.3. 316L's chemical composition can be found in Table 3.4. In contrast to other software programs, Software #1's isotropic plastic curve is multilinear, meaning it can be subdivided into multiple linear segments within the plastic regime, and can be found in Figure 3.6a. A multilinear flow rule means the value interpolation can be more well defined, at the cost of greater computational power.

Furthermore, Software #1's framework does not allow property definition as a function of temperature for distortion calculations, being reserved to other functions the package offers: this fact is unfortunate, as mechanical and physical properties experience a significant

change with temperature [46].

Iconel 625 Iconel is a material that is a part of the larger subset of nickel-based alloys named *superalloys* [49]. These materials combine high strength with good creep and corrosion resistance, making them common in application such as fuel cells, nuclear power plants and gas turbine engines [50]. There are several factors that contribute to nickel-based superalloys' exceptional mechanical characteristics: *(i) microstructure:* its Face-Centred Cubic (FCC) crystal structure means that the rates at which thermally-activated creep mechanisms are activated are low [51]; *(ii) phase stability:* the mentioned FCC crystal structure is maintained from ambient temperature to Iconel's melting point, meaning that no thermal energy is spent in phase changes [51, 52]; *(iii) solubility:* alloying elements are easily soluble in the nickel matrix, favouring the creation of a γ phase. Hence, elements like chromium (Cr) and cobalt (Co) improve oxidation and corrosion behaviour, while aluminium (Al) and titanium (Ti) improve the flow stress and ultimate tensile strength [51]; *(iv) hardening:* the intermetallic phases γ can be made to precipitate through solid solution hardening, carbide precipitation or precipitation hardening [52]. For the case of solid solution hardening, the material is heated to temperatures around 60% of the alloy's melting temperature, a temperature at which the strengthening process that is undergone is diffusion dependent [52].

Iconel 625's chemical composition is found in Table 3.4, in which the *Bal* nomenclature means that the quantity of nickel (Ni) is the remaining percentage of the material. Mechanical properties as defined in Software #1 are displayed in Table 3.3, and the material's plasticity curve is outlined in Figure 3.6b.

Table 3.3: 316L and Iconel 625's properties, as defined by Software #1's internal library.

Material	**Melting temperature T_m**	**Exp. Coeff. α**	**Young's modulus E**	**Poisson's ratio ν**
316L	1673.15 K	$1.990 \times 10^{-5}\,\mathrm{K}^{-1}$	195 GPa	0.29
Iconel	1563 K	$1.280 \times 10^{-5}\,\mathrm{K}^{-1}$	205 GPa	0.278

Table 3.4: 316L and Iconel 625 chemical compositions.

Material	**C (%)**	**Cr (%)**	**Ni (%)**	**Mn (%)**	**Mo (%)**	**Nb (%)**
316L	0.02	16.4	10.5	1.8	2.1	-
Iconel 625	0.05	21.5	Bal.	-	9.0	3.6

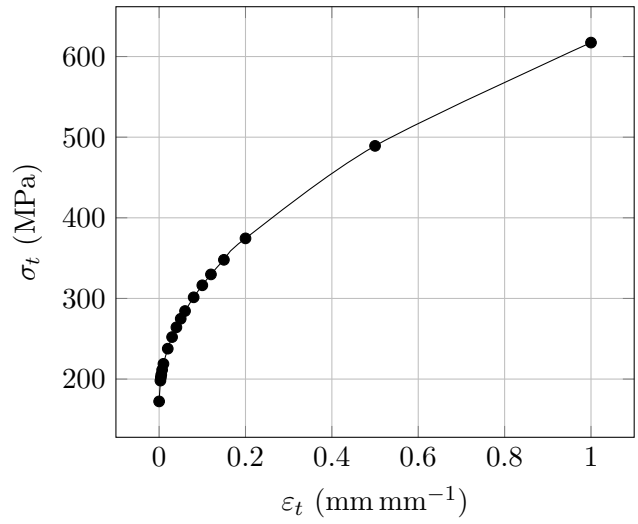

(a) 316L

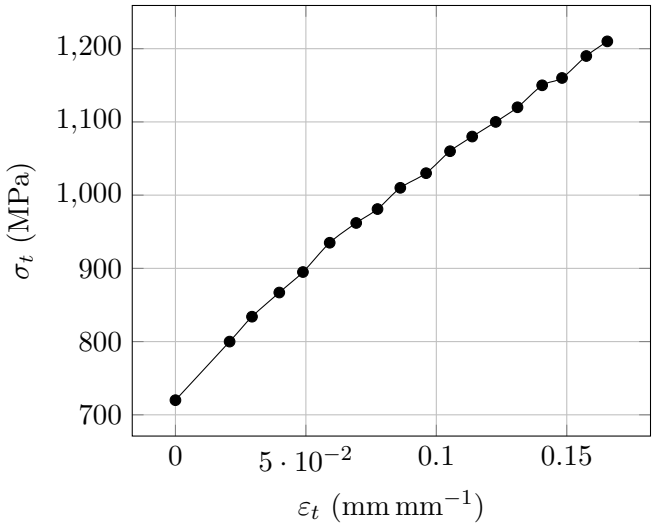

(b) Iconel 625

Figure 3.6: 316 stainless steel properties as functions of temperature, as defined in Software #1's internal libraries.

3.2.3 Software #2

Software #2's internal library contains several of the most widely used materials in AM, and in the following paragraphs, the materials' definition and properties will be explored.

316L Stainless Steel Software #2's internal library does not contain 316L stainless steel, therefore it had to be user-defined. Due to the weak thermal-mechanical coupling of Software #2's solutions, there were additional parameters that needed to be introduced for the simulation to be possible in regards to Software #1, namely the material's density ρ, thermal conductivity k and specific heat c_p. These values were chosen to be the same as Software #2's 316 Stainless Steel at the lowest temperature setting, and are presented in Table 3.5; the other properties common in both software packages were defined identically. The choice for these parameters to be temperature independent is two-fold: *(i):* as this material is purposely created to establish a comparison within programs, there seems to be

no incentive to over-complicate a property that is solely requested in one of the programs; *(ii):* variables represented by laws or tables, rather than fixed independent values that need no interpolations, require more computational power.

Table 3.5: 316L thermal properties, as user-defined in Software #2.

Density ρ	**Thermal Conductivity** k	**Specific Heat** c_p
$7954\,\mathrm{kg\,m^{-3}}$	$13.44\,\mathrm{W\,m^{-1}\,K^{-1}}$	$498.37\,\mathrm{J\,m^{-1}\,K^{-1}}$

316 Stainless Steel Unlike 316L, this steel was exclusively used in parametric studies to analyse the input variables' impact on the simulations' results. All properties were left intact for simplicity's sake, and all properties' evolution's in function of temperature are displayed in Figures 3.7a-3.7f; the only stationary property is its melting temperature T_m, which is fixed at 1643.15 K, and the plasticity curve, present in Figure 3.9a.

Software #2's internal library uses an isotropic, bilinear hardening law to represent 316's plasticity, described both by the Young's modulus E, the Tangent modulus E_t and the Yield Strength σ_{ys} for each temperature T.

Iconel 625 The physical properties of Iconel are displayed in Table 3.6, as defined in Software #2. The mechanical and thermal properties whose values are defined as functions of temperature are displayed in Figures 3.8a-3.8e, while the plastic curves as functions of temperature are present in Figure 3.9b.

Table 3.6: Physical properties of Iconel 625, as defined in Software #2

Material	**Density** ρ	**Melting temperature** T_m
Iconel 625	$8440\,\mathrm{kg\,m^{-3}}$	1563.15 K

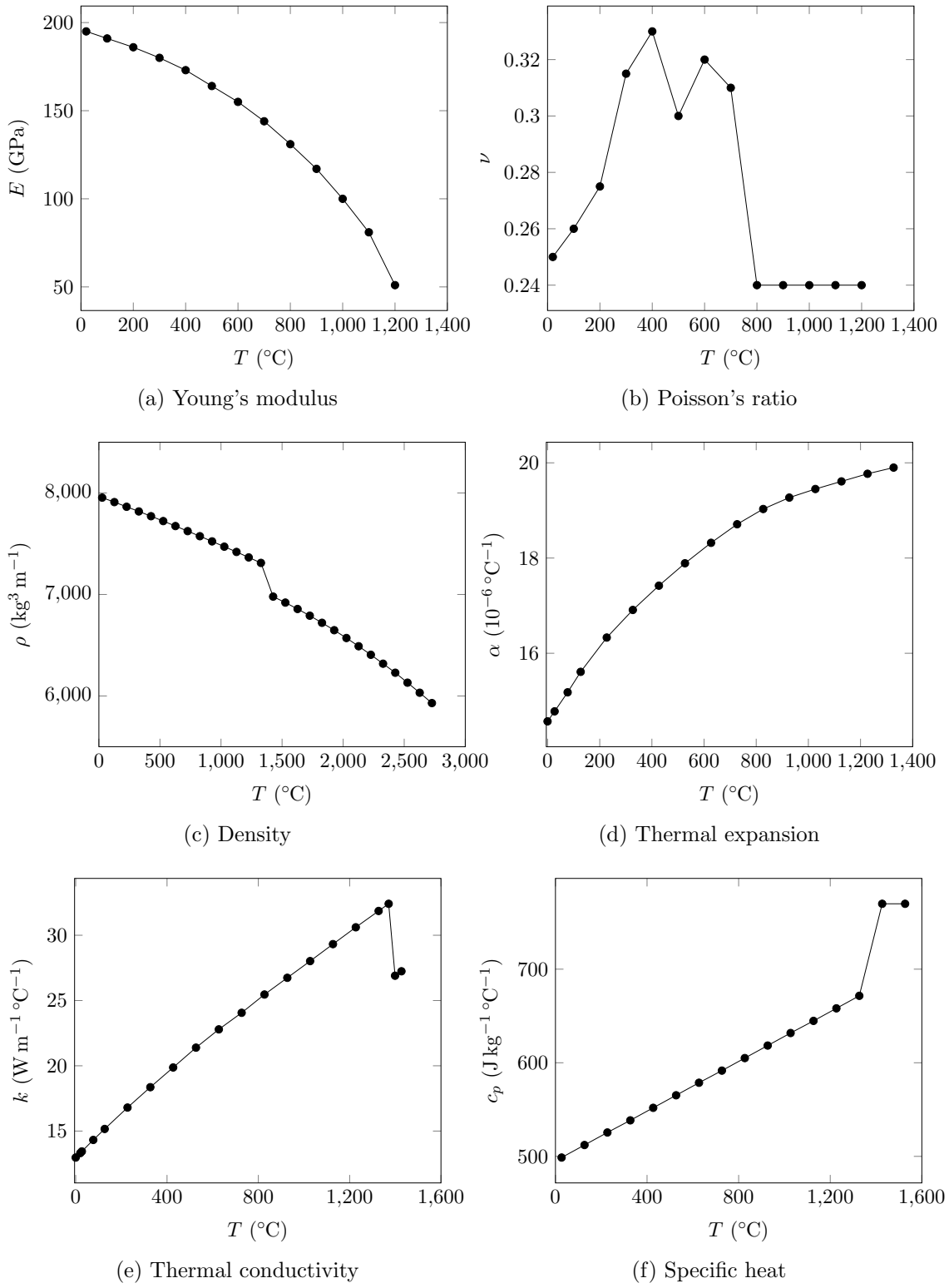

(a) Young's modulus

(b) Poisson's ratio

(c) Density

(d) Thermal expansion

(e) Thermal conductivity

(f) Specific heat

Figure 3.7: 316 stainless steel properties as functions of temperature, as defined in Software #2's internal libraries.

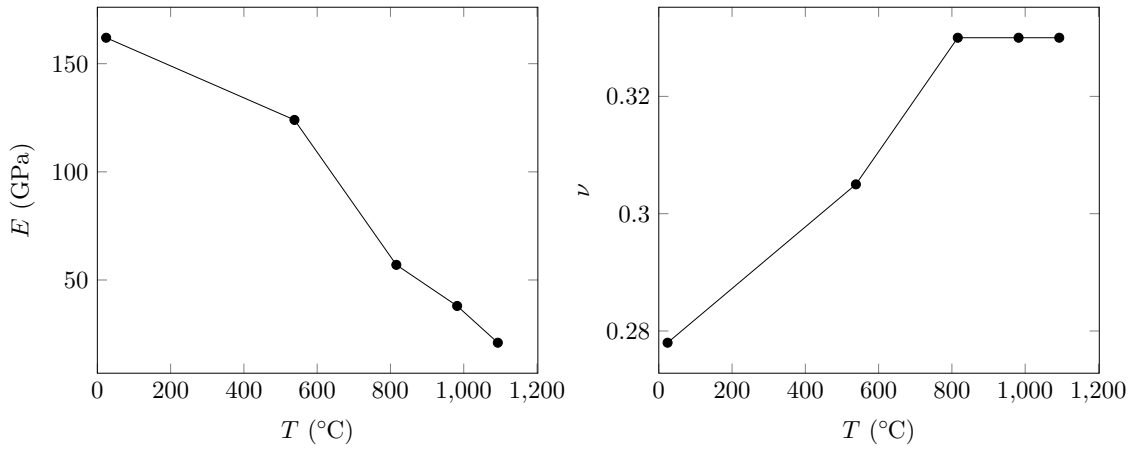

(a) Young's modulus

(b) Poisson's ratio

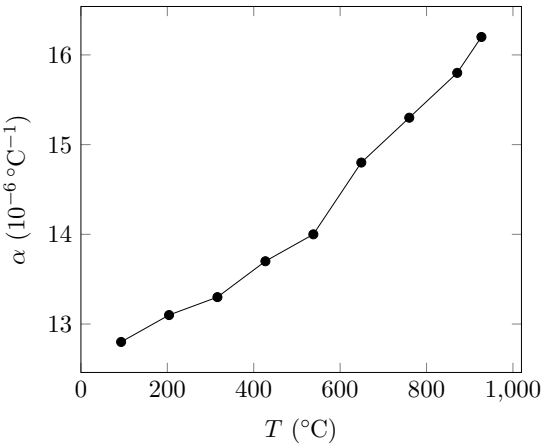

(c) Thermal expansion

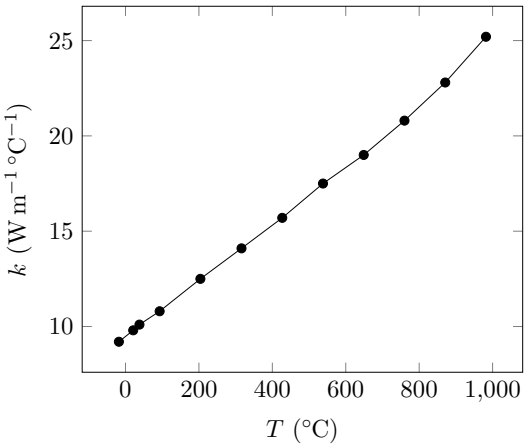

(d) Thermal conductivity

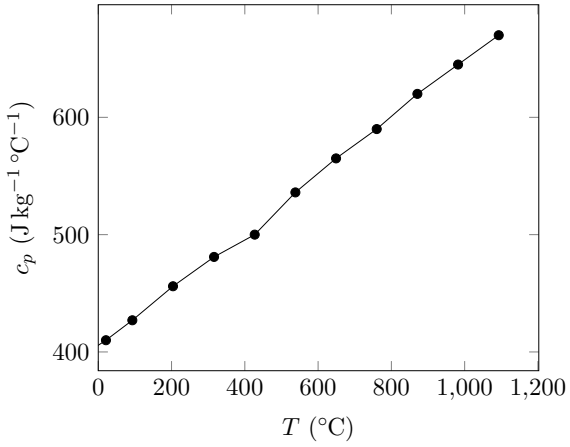

(e) Specific heat

Figure 3.8: Iconel 625 properties as functions of temperature, as defined in Software #2's internal libraries.

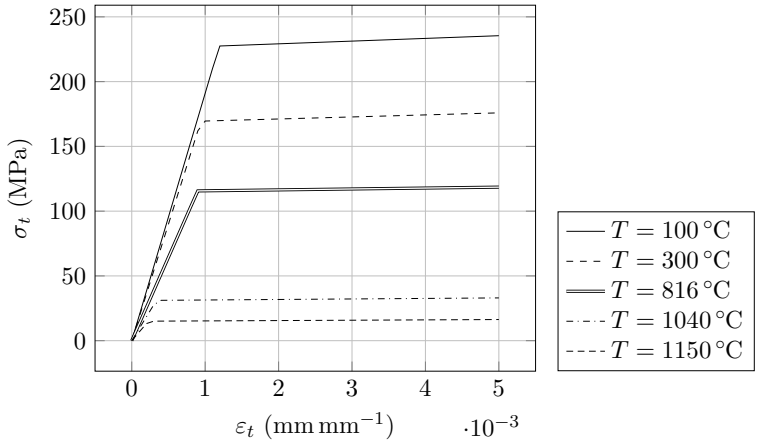

(a) 316 Stainless Steel

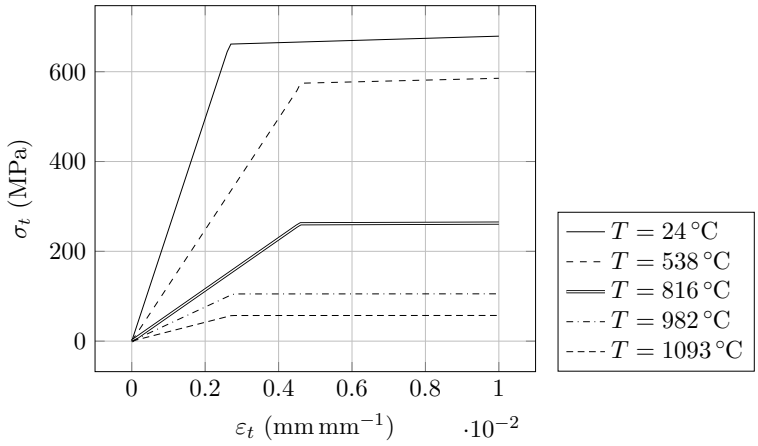

(b) Iconel 625

Figure 3.9: Plasticity laws in function of temperature, as defined in Software #2's internal library.

3.3 Parametric analysis

3.3.1 Introduction

Parametric simulations are simulations whose goal is maintaining the same parameters except one, in order to analyse the final result's sensitivity to the input variation.

Parametric studies are of utmost importance when dealing with commercial software packages, as without a substantiated idea regarding the impact of a simulation's user-controlled parameters, reasonable conclusions cannot be taken from the simulation's solutions. Additionally, this analysis allows the establishment of the minimum parameters that guarantee the convergence of the solution while minimising computational effort.

Some of the parameters were explained in Subsection 2.2.2, as introduced in the software's user guide. In this Section, the conducted simulations and their chosen parameters are explored in detail.

3.3.2 Software #1

Within the environment of Software #1, the main objective was the study of three simulation conditions:

1. The study of mesh refinement;
2. The analysis of improving the *lumping factor*, that is, the factor that relates the numerical layer's thickness with the number of simulated layers, as defined in Equation (3.1);
3. The effect of the baseplate thickness.

The different simulations were grouped in simulation sets, where their respective mesh size dimensions varied from 5 mm to 0.5 mm, as outlined in Table 3.7. These simulations were conducted in the prism.

Table 3.7: Parameter simulation groups.

Simulation Group	**Number of simulations**	**Mesh size** (mm)	**Lumping Factor**
1st Group	7	5	125, 50, 25, 10, 5, 2, 1
2nd Group	7	2.5	125, 50, 25, 10, 5, 2, 1
3rd Group	7	1	125, 50, 25, 10, 5, 2, 1
4th Group	6	0.5	125, 50, 25, 10, 5, 2

The common parameters across all the mesh and lumping factor simulations are outlined in Table 3.8.

Mesh size

Software #1's internal meshing strategy is mainly defined by four parameters, as explained in Subsection 2.2.2: *(i) boundary refinement,* the measured in millimetres of the element's dimensions; *(ii) background fineness,* a parameter suited to adjust the cell sizes at the boundaries of the workpiece; *(iii) lumping factor,* that corresponds to the number of processed layers that are fused to be simulated as one layer; *(iv) subdivisions per layer,* the minimum number of elements considered in a simulated layer.

Table 3.8: Simulation properties common in all mesh size and lumping factor parametric studies, for Software #1.

Parameter	**Definition**	**Value**
Materials	Component	316L Stainless Steel
	Baseplate	316L Stainless Steel
Workpiece	Prism	$50 \times 10 \times 20$ mm
Baseplate	Custom	$100 \times 40 \times 20$ mm
Mesh	Powder thickness	0.04 mm
	Subdivisions per layer	1
	Background fineness	0.25 mm
Temperatures	Build	30 °C
	Release	30 °C
	Removal	30 °C
	Shrinkage Law	Not applicable
Other	Finite strains	No

The mesh size is the target of the first round of simulations in order to determine Software #1's residual stresses' sensibility to the mesh size, as well as the convergence of results and the respective simulation time. The graphical representation of the mesh refinement for the same lumping factor is shown in Figures 3.10a-3.10d.

Lumping factor

After measuring the influence of the mesh size in residual stresses in the prism's surface, the lumping factor also presents itself as a valuable simulation parameter. Its relation to the numerical layer thickness and the deposited powder is given in Equation (3.1):

$$t_{num} = LF \cdot t_{layer} \tag{3.1}$$

, where t_{num} is the numerical layer's thickness, LF is the lumping factor and t_{layer} is the deposited layer's thickness.

Each numerical layer is used to simulate the cooldown and solidification of the powder, so it is intrinsically linked to the additive step and therefore it is expected to largely affect both the overall results as well as the simulation run-time.

Table 3.9 explores the developed numerical simulations aimed to measure the impact the lumping factor possesses on the evolution of stresses around the part, and Figures 3.11a-3.11c serve as visual representation of the mesh as the lumping factor decreases. Other remaining parameters are displayed in Table 3.8.

Baseplate thickness

The baseplate is responsible for the prevention of excessive distortions during the build process, as previously explained in Section 2.1. Therefore, the analysis of how the reduction in the baseplate's stiffness impacts the part's behaviour is of great interest.

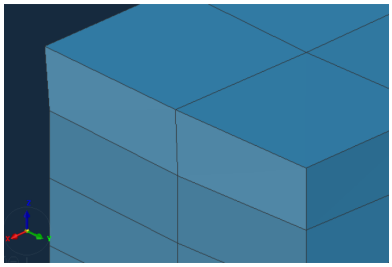

(a) Mesh size of 5.0 mm

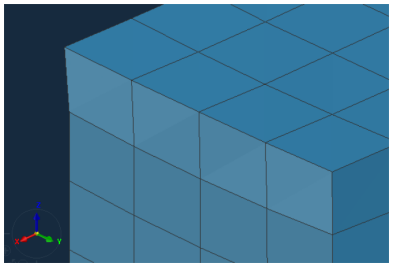

(b) Mesh size of 2.5 mm

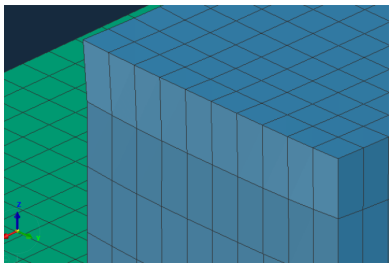

(c) Mesh size of 1.0 mm

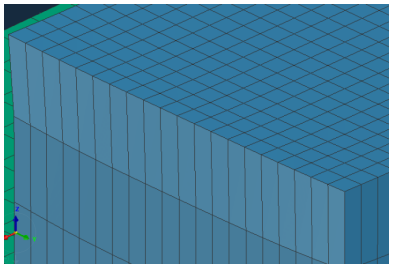

(d) Mesh size of 0.5 mm

Figure 3.10: Mesh size evolution within the 2nd Group of simulations using Software #1, with lumping factor of 50.

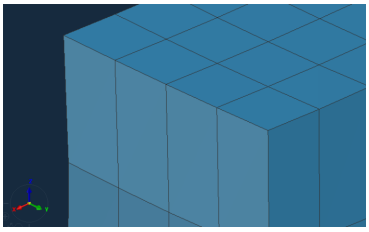

(a) Lumping factor of 125

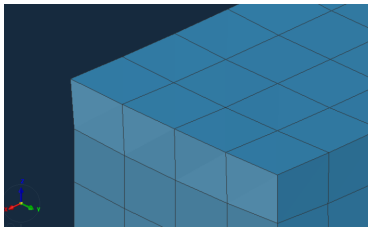

(b) Lumping factor of 50

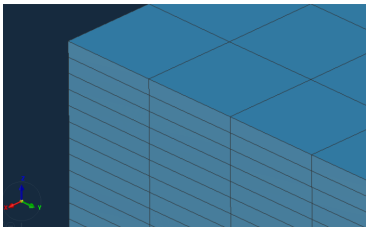

(c) Lumping factor of 10

Figure 3.11: Mesh size evolution within the 2nd Group of simulations using Software #1, with a mesh size of 2.5 mm.

The simulation of the alteration of the thickness of the baseplate raises a key aspect of how Software #1's meshing algorithm works, and it is important to reiterate the explanation given in Subsection 2.2.2. Essentially, Software #1 offers two meshing strategies within conform meshes: *(i) exact plate definition,* where the meshing algorithm favours the dimensions of the baseplate; *(ii) workpiece meshing strategy,* where the main objective is remaining as close as possible to the part dimensions. Figure 3.12 schematically demonstrates this difference.

Additionally, this simulation was an opportunity to measure the difference in results if the large displacement hypothesis is activated, which allows for non-linear mechanics. *Finite strain theory*, or *large strain theory*, is a realm of continuum mechanics that deals with displacements that would otherwise invalidate the assumptions inherent to infinitesimal strain theories [53]. One widely used strain tensor is Green's strain tensor, shown in Equation (3.3.2).

$$\varepsilon_{ij} = \frac{1}{2}\left(\frac{\partial u_i}{\partial x_j} + \frac{\partial u_j}{\partial x_i} + \sum_{k=1}^{3} \frac{\partial u_k}{\partial x_i}\frac{\partial u_k}{\partial x_j}\right) \tag{3.2}$$

Table 3.9: Developed numerical simulations to measure the effect of the lumping factor.

Mesh size	**Lumping factors (Numerical layer's thickness** (mm)**)**						
5.0	125 (5)	50 (2)	25 (1)	10 (0.4)	5 (0.2)	2 (0.08)	1 (0.04)
2.5	125 (5)	50 (2)	25 (1)	10 (0.4)	5 (0.2)	2 (0.08)	1 (0.04)
1.0	125 (5)	50 (2)	25 (1)	10 (0.4)	5 (0.2)	2 (0.08)	1 (0.04)
0.5	125 (5)	50 (2)	25 (1)	10 (0.4)	5 (0.2)	2 (0.08)	-

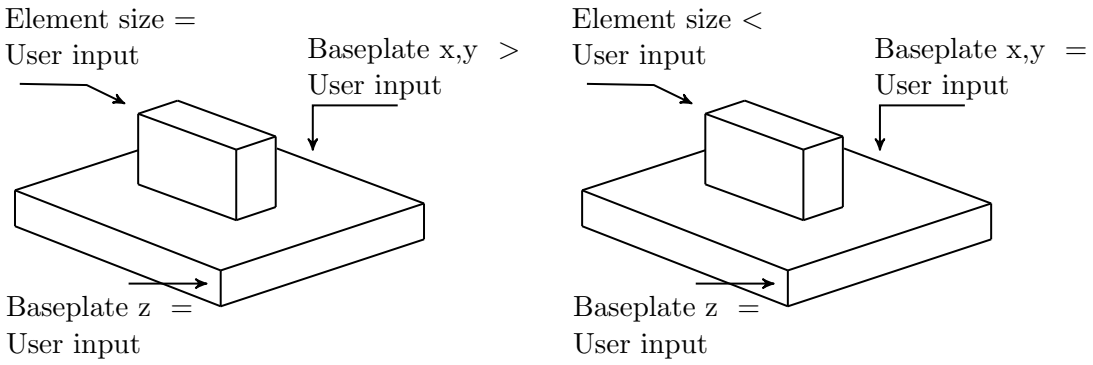

(a) Workpiece strategy (b) Baseplate strategy

Figure 3.12: Software #1's meshing strategies.

where the notations u_i and x_i, $i = 1, 2, 3$ are purely used for the sake of simplicity, meant to represent u_x, u_y, u_z, x, y and z, respectively. A purely linear analysis disregards the sum component in the strain calculations, as it is obviously a second order term. Not much attention will be given to finite strain theory, and further reading is encouraged in literature [53].

Lastly, Table 3.10 outlines the conducted simulations and Table 3.11 presents the parameters common in these simulations.

Table 3.10: Developed numerical simulations to measure the effect of the baseplate thickness.

Simulation group	**Baseplate thickness** (mm)				**Large strain**
5^{th} Group	20	10	5	2	No
6^{th} Group	20	10	5	2	Yes

Table 3.11: Simulation properties common in all baseplate thickness parametric studies, for Software #1.

Parameter	**Definition**	**Value**
Materials	Component	316L Stainless Steel
	Baseplate	316L Stainless Steel
Workpiece	Prism	$100 \times 40 \times 20$mm
Mesh	Mesh size	2.5
	Lumping Factor	25
	Powder thickness	0.04
	Subdivisions per layer	1
	Background fineness	0.25
Temperatures	Build	30
	Release	30
	Removal	30
	Shrinkage Law	Not applicable

3.3.3 Software #2

Software #2 brings different capabilities to the table: its formulation is within the realm of weakly coupled thermal-structural analysis, but as previously mentioned, its capacities to handle temperature-dependent properties makes the simulation assumptions more reasonable; additionally, and the most valuable aspect within the parametric context of this particular software, is its automatised parametric module, where one can insert the desired inputs and directly obtain custom outputs, requiring minimal post-processing.

This software has a larger set of features than Software #1, specifically the temperatures associated with the powder and the baseplate preheat, cooldown temperatures after the build process is carried, as well as the machine setting. Therefore, it was of interest to see how these new aspects influenced the final results. The chosen simulations are presented in this Section, as well as the reasoning behind their choice. Moreover, the common features shared by all simulations are presented in Table 3.12.

Laser Speed

Due to the additional machine settings allowed by this software package, it was of interest to analyse the laser speed. In the real world process of LPBF, low scanning speeds are associated with higher porosity and evaporation defects if the laser power is too elevated [54], while increasing the laser speed for the same laser power reduced the maximum reached temperature, actually reducing residual stresses [55]. However, as laser power is not a simulation parameter due to the fact that the software does not model the physical interaction between laser beam - powder, the expected result of increasing the scanning speed is a smaller time step between layer deposition.

In order to analyse laser speed's effect and take full advantage of automatic parametric simulations, fifteen values were chosen, as presented in Table 3.13.

Table 3.12: Simulation properties common in all parametric studies, for Software #2.

Definition	Value	Definition	Value
Component	316 Stainless Steel	Pre heat temperature	100 °C
Baseplate	316 Stainless Steel	Gas temperature	100 °C
Prism	50 × 10 × 20mm	Powder temperature	100 °C
Custom	100 × 40 × 20mm	Gas convection coefficient	10 W m^{-2} °C^{-1}
Part mesh size	1 mm	Powder conv. coeff.	10 W m^{-2} °C^{-1}
Baseplate mesh size	2.5 mm	Powder property factor	0.01
Projection factor	0	Room Temperature	30 °C
Powder thickness	0.04 mm	Gas Powder temperature	30 °C
Laser speed	variable	Powder temperature	30 °C
Hatch distance	variable	Gas convection coefficient	10 W m^{-2} °C^{-1}
Time between layers	10 s	Powder conv. coeff.	10 W m^{-2} °C^{-1}
Dwell time multiplier	1	Build boundary temp.	100 °C
N. of heat sources	1	Cool down temperature	30 °C

Table 3.13: Laser speed parameter values.

L. S. (m s^{-1})	0.1	0.2	0.3	0.4	0.5	0.6	0.7	0.8	0.9	1	1.1	1.2	1.5	2	5

Hatch Space

The hatch space is the space between two consecutive laser scans in the same layer. This parameter, such as the Laser Speed, is mostly expected to influence the time step between layer deposition, and its values are displayed in Table 3.14.

Table 3.14: Hatch space parameter values.

Hatch Space (mm)	0.05	0.06	0.07	0.08	0.09	0.1	0.15	0.2	0.3	0.4	0.5

Preheat temperature

The Preheat temperature corresponds to the temperature the baseplate is heated and maintained during the build stage of the process. This temperature is important to prevent steeper heat gradients arising from the temperature difference between the metal in its melting state and the environment. Increased pre-heating temperatures are expected to result in lower distortions, and therefore decreased residual stresses. The values are displayed in Table 3.15.

Cooldown temperature

The cooldown stage is a specific stage Software #2 simulates after the build stage, where all layers have been constructed and the workpiece is complete, subsequently cooling down to a user controlled temperature. This is an interesting parameter to review, as it allows the analysis of the residual stress evolution with time, depending on the final temperature. The parametrised values are outlined in Table 3.16.

Table 3.15: Preheat temperature parameter values.

Preheat Temp. (°C)	25	50	75	100	150	200	300	400	500	750	1000

Table 3.16: Cooldown Temperature parameter values.

Cooldown Temperature (°C)	0	25	50	75	100

3.4 Simulations aimed at comparing software

Until this section, the simulations have revolved around understanding the influence of a specific parameter between the same software and paradigm. In this Section, a different approach is chosen, which consists of mimicking the same simulation parameters as close as possible in both Software #1 and Software #2.

3.4.1 One layer

This initial proposal is aimed at reducing the problem to a single unique layer deposited over the baseplate. The reasoning behind this decision is two-fold: *(i) heat transfer between layers:* the fact that the workpiece is exclusively made out of one layer eliminates the effects that arise between the energy transfer between successive layers, a phenomenon that happens in Software #2; *(ii) boundary conditions:* the fact that one layer is being solidified emphasises the boundary conditions between the component and baseplate with the remaining environment.

Numerically, this component is one unique layer, meaning that the software considers only one simulation step pertaining to the addition of new material, and the mesh is only one element thick in the building direction (z): Figure 3.13 showcases the mesh strategy adopted in the simulation. The geometry of the layer is equivalent to an arbitrary cross-section of the prism across a xy plane, while the baseplate's dimensions arise from the workpiece-oriented meshing strategy illustrated in Figure 3.12a.

Both simulation's components are composed of 316L Stainless Steel internally defined in Software #1's library and user-defined in Software #2 accordingly, as explored in Section 3.2.

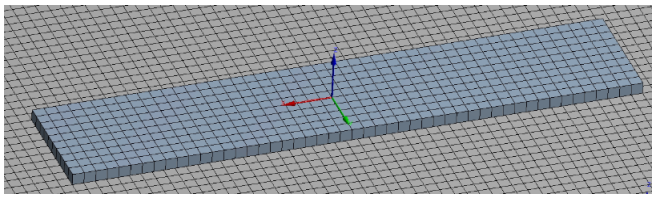

Figure 3.13: One layer meshing strategy.

3.4.2 Prism

After analysing the differences between the results of a single layer, results for the prism's AM process were compared, for the same mesh and material. The only concern in this stage of the simulation was the choice of meshed whose elements were cubic in geometry due to Software #2's limitation in the creation of Cartesian meshes. Therefore, two already developed simulations for Software #1 were found to be suitable, as observed in Table 3.9:

meshes with in-plane mesh size of 5.0 and 1.0 coupled with lumping factors of 125 and 25, respectively.

3.4.3 Benchmark bridges

This final simulation was of interest mostly in order to perform a holistic analysis of the benchmark bridges' residual stress distribution. Although Software #1 only allows regular prismatic meshes, Software #2's Projection Factor parameter can be used to alter the element's cubic nature into more adaptable non-regular prism, as displayed in Figures 3.14a-3.14c. This simulation's objective is, therefore, to measure the influence of this parameter in the global evolution of stresses, particularly around the sharp corners that often lead to numerical singularities.

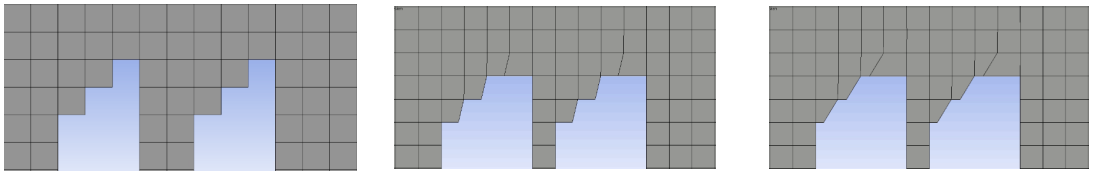

(a) Projection factor of 0 (b) Projection factor of 0.25 (c) Projection factor of 0.75

Figure 3.14: Mesh evolution according to the projection factor.

3.5 Part removal simulation

Parts produced by laser powder bed fusion are built on top of rigid metallic structures to prevent excess distortion in the build process. However, these parts are then removed through an additional technological process, such as electrical discharge machining, which can increase some already developed displacements while reducing the internal stress field's magnitude.

These simulations were conducted using the benchmark bridges as models, due to their geometry which emphasises the vertical displacements that are due to the lack of support at their core. Hence, the concept of this analysis will be removing the boundary conditions of the element nodes pertaining to the part-baseplate interface, one bridge *leg* at a time. Figure 3.15a displays the initial state, in which the part is fully fixed and all nodal degrees of freedom are restricted, and Figure 3.15b shows the third simulation step, in which three bridge *legs* have been *released* - meaning that their degrees of freedom are unrestricted.

This logic applies to the remaining *legs* until all but the last one are still fixed. The residual stresses and strains are subsequently analysed.

(a) Initial conditions (b) 3rd simulation step

Figure 3.15: Evolution of the boundary conditions between the benchmark bridge and the baseplate in the removal simulation.

Software #1 and Software #2 are setup in different manners, in regards to how the part removal is introduced. The former allows the creation of new steps, in which the

user inputs what degrees of freedom it wants to restrict in which respective nodes for each simulation step, while the latter requires two parameters: the removal direction and what distance encompasses the nodes that are detached at each step. This particular aspect of the simulation pre-processing is not too relevant, other than the fact that the removal steps in Software #2 had to be spaced at 0.5mm each, as this is the smallest bridge *leg*'s thickness.

The simulation properties for Software #1 and Software #2 are found in Table 3.17 and Table 3.18, respectively.

Table 3.17: Simulation properties of the benchmark bridge removal simulation, for Software #1.

Parameter	**Definition**	**Value**
Materials	Component	316L Stainless Steel
	Baseplate	316L Stainless Steel
Workpiece	Bridges	$75 \times 5 \times 12.5$mm
Baseplate	Baseplate	$200 \times 200 \times 20$mm
Mesh	Mesh size	0.625 °C
	Lumping Factor	1
	Powder thickness	0.04 mm
	Subdivisions per layer	1
	Background fineness	0.25
Temperatures	Build	30 °C
	Release	30 °C
	Removal	30 °C
	Shrinkage Law	Not applicable

3.6 Comparison between numerical and experimental results

The simulation presented in this Section is aimed at establishing a comparison between results obtained through both FEA and experimental methods. Therefore, the simulation process needed to replicate the component's manufacturing process variables as truthfully as possible, in order to produce results comparable to the ones obtained experimentally. This simulation also took advantage of the gathered knowledge of the previous numerical studies.

The chosen component to simulate was the NIST benchmark bridge, as its manufacturing process is highly detailed and is subject to several published reviews. Moreover, two different instances could be simulated: the residual strain field after the build process, in which the component is still physically attached to the baseplate; a second instance, where the component's multiple legs are progressively removed, and the part's deflection is studied.

In Subsection 3.6.1, the methods in which the attainment of the used experimental values are discussed, and Subsection 3.6.2 introduced the simulation's parameters.

3.6.1 Experimental result attainment

The experimental residual strain fields used in the comparison to the numerical residual strain fields was obtained through X-ray diffraction [56], in the $y = 2.5\,\text{mm}$ plane, schematically represented in Figure 3.16. Each measurement was taken 0.25 mm apart in the bridge legs area, and taken 0.75 mm apart in the remaining structure, according to Figure 3.17.

The chosen setup used by Phan et al. (2017) [56] resulted in the determination of residual strain in three differing directions: longitudinal strain ε_{xx}, vertical strain ε_{zz}, and a strain component 45° off the vertical direction; strains in the transverse direction were not determined due to the inability of X-ray being consistently absorbed along 75 mm of length across the component [56].

One of the advantages of X-ray diffraction is the ability to collect the entire line pattern, allowing a more accurate processing and curve-fitting of the measurement through an automated SMARTSware [57] and General Structural Analysis System (GSAS) [58].

Through the data obtained in this method, strains are then calculated via Equation (3.3):

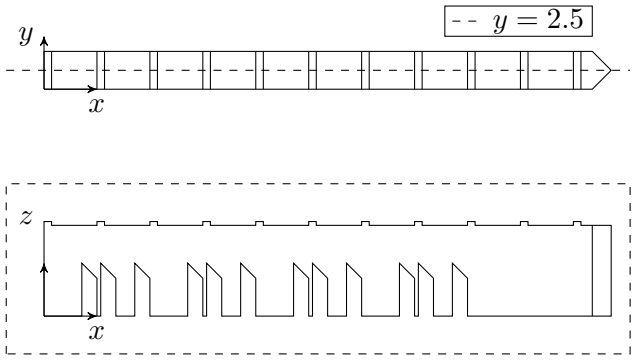

Figure 3.16: Schematic representation of plane in which residual strains were experimentally measured.

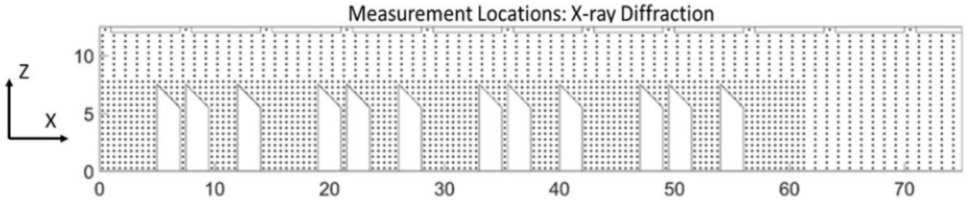

Figure 3.17: Measurement locations, in the Iconel 625 benchmark bridges produced by NIST, for the residual strains using X-ray diffraction.

$$\varepsilon_i = \frac{a_i - a_0}{a_0} \tag{3.3}$$

in which ε_i is the strain along the i direction, a_i is the unit cell parameter and a_0 is the unstrained lattice parameter. The latter consists of a separate measurement of a reference sample, measuring $2 \times 2 \times 3\,\text{mm}$, extracted from an identical part through EDM to ensure no macroscopic residual stress [59]. The tensorial shear residual stress ε_{xz} was determined through Equation (3.4):

$$\varepsilon_{xz} = \frac{1}{2}\left(\varepsilon_{xx} - \varepsilon_{zz}\right) - \varepsilon_{45} \tag{3.4}$$

where ε_{xx}, ε_{zz} and ε_{45} are the longitudinal, vertical and the 45° strains. The experimental uncertainty related to the employed measurement by Phan et al. (2017) is of 1×10^{-4}, derived from the estimated standard deviation pertaining to the performed curve-fitting [56].

3.6.2 Process parameters

The chosen software package for this final simulation group was Software #2 for two distinct reasons: *(i)* this product allows the definition of more simulation parameters, granting a more detailed pre-processing stage to the experimental manufacturing process; *(ii)* the internal network of INEGI suffered problems, rendering Software #1 unusable for a period of time that would be used for obtainig results.

The process variables of this simulation are introduced in Table 3.18. Three different projection factors were employed to expand the established comparison with experimental values, analysing the mesh's effect on accurately reproducing the residual stress field.

Table 3.18: Simulation properties of the benchmark bridge removal simulation, for Software #2.

Definition	**Value**	**Definition**	**Value**
Component	Iconel 625	Pre heat temperature	100 °C
Baseplate	Iconel 625	Gas temperature	100 °C
Bridges	75 × 5 × 12.5mm	Powder temperature	100 °C
Baseplate	100 × 100 × 12.7mm	Gas convection coefficient	$10\,\mathrm{W\,m^{-2}\,°C^{-1}}$
Part mesh size	0.25 mm	Powder conv. coeff.	$10\,\mathrm{W\,m^{-2}\,°C^{-1}}$
Baseplate mesh size	10 mm	Powder property factor	0.01
Projection factor	variable	Room Temperature	30 °C
Powder thickness	0.02 mm	Gas Powder temperature	30 °C
Laser speed	$0.95\,\mathrm{m\,s^{-1}}$	Powder temperature	30 °C
Hatch distance	0.10 mm	Gas convection coefficient	$10\,\mathrm{W\,m^{-2}\,°C^{-1}}$
Time between layers	10 s	Powder conv. coeff.	$10\,\mathrm{W\,m^{-2}\,°C^{-1}}$
Dwell time multiplier	4	Build boundary temp.	100 °C
N. of heat sources	1	Cool down temperature	30 °C

Regarding the component's removal procedure, the three chosen nodes to restrain the body were chosen to have the following coordinates: $(56, 0, 0)$, $(72.5, 5, 0)$ and $(72.5, 0, 0)$, in which the first node restricts all degrees of freedom, the second one restricts movement on the x and z direction, and the last node is fixed solely on the z direction.

Chapter 4

Results and Discussion

In this Chapter, the results of the numerical simulations carried in Chapter 3 are presented and discussed in further detail.

4.1 Parametric simulations

Parametric simulations, as explained beforehand, are responsible for measuring a variable's influence on the numerical results. In most simulations, the nodal variable outputs that were measured are common throughout: in the case of the Prism, the tracked nodal variable outputs were the residual stresses, both in the longitudinal σ_{xx} and transverse σ_{yy} directions. Out-of-plane stresses σ_{zz} were mostly accounted for in nodes within the workpiece-baseplate interface. Three nodes, (A), (B) and (C), were established to measure these variables, as schematically shown in Figure 4.1: in node (C), the longitudinal and transverse residual stresses σ_{xx} and σ_{yy} were determined, while the vertical stress σ_{zz} was obtained in node (A) and (B).

Node (C) was chosen for several reasons: *(i)* it is easy to obtain in the post-processing stage, *(ii)* it highlights the effect of the boundary conditions at the top layer of the prism, and *(iii)* it is distant from any sharp corners or other particularities that would hinder a clear analysis. Node (A) was defined to better account for the interaction between the baseplate and the prism; the reason why node (B) was analysed is later explained, in Section 4.1.

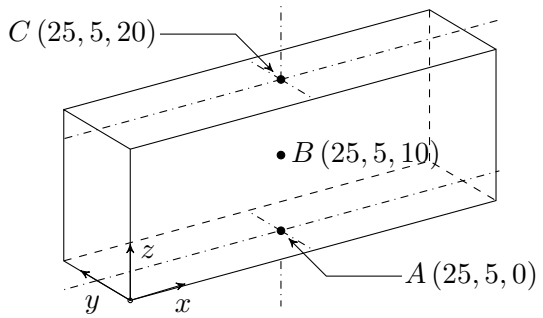

Figure 4.1: Schematic representation of nodes (A), (B) and (C).

4.1.1 Mesh size

In this Subsection, the results regarding the in-plane mesh size's influence in the residual stress is analysed. As explained in Section 3.3, the studied component is the prism, constructed with 316L Stainless Steel whose properties are internally defined in Software #1's internal library and therefore are not temperature dependent. All simulation groups in which the background fineness was improved, that is, the in-plane mesh size was decreased, were composed of four different sizes, as seen in Table 3.7 - 5.0, 2.5, 1.0 and 0.5 mm - with the exception of the latest group, with a unitary lumping factor, in which the prepared simulation resulted in an error by the software, and was therefore abandoned.

The results of each simulation group are presented in two different sets of graphs: Figures 4.2a-4.2g, which explore the data pertaining to the residual stresses in the x and y directions σ_{xx} and σ_{yy} for node (C), and Figures 4.3a-4.3g, which contain the stress in the z direction, σ_{zz}, for nodes (A) and (B).

Using a convergence criteria of 5% in regards to the result obtained with the finest mesh within each lumping factor group, the results show that, generally, the tracked nodal variables did, indeed, converge. Furthermore, the longitudinal and transverse stresses, σ_{xx} and σ_{yy}, of node (C) converged to a 5% difference in comparison to the values corresponding to the most refined mesh of the analysis with a mesh size of 2.5 mm, and converged to a 2% difference with a mesh size of 1.0 mm. Under no longitudinal or transverse stress, a worsening of the difference occurred, and it is observed that, with a decrease of the lumping factor, the sensitivity of the residual stresses in node (C) to the in-plane mesh size decreased.

One of the striking observations that can be made when comparing Figure 4.2a with the remaining graphs in Figures 4.2b-4.2g is based on the considerably smaller transverse stress values σ_{yy} when the lumping factor is 125: this is explained by the lack of simulated numerical layers. In fact, for a simulation with 2000 elements per layer, σ_{yy}, still presented a 65.3% difference in regards to the most rigorous simulation conducted, of mesh size 1.0 mm with a unitary lumping factor.

It can also be seen that, with an increase in simulated layers, the residual stresses σ_{xx} and σ_{yy} increased: the longitudinal stress σ_{xx} in node (C) changed from 211.55 MPa to 249.91 MPa, when the lumping factor decreased from 125 to 2, while the transverse stress σ_{yy} increased from 95.86 MPa to 275.86 MPa under the same conditions. In fact, the increase of the stress was expected considering that the increase in layers model the part deformation due to the cooling cycles.

In regards to the out-of-plane stress results σ_{zz} in nodes (A) and (B), these values still converged, even if at slightly larger differences when compared to the in-plane stress, generally fulfilling the 5% criteria, but failing the 2% difference.

One can observe through Figures 4.3 the consistently poor results for the vertical stress σ_{zz}, in node (B), for any lumping factor with a mesh size of 5 mm. This can be explained through the coarse meshes in the respective simulations: knowing that the width of the Prism is only 10 mm, the mesh contains two elements in the y direction regardless of the lumping factor, as visible in Figure 4.4a. Here, the aforementioned adaptive meshing revealed itself to be useful for the computation of stresses in node (A), as its stresses at this mesh configuration are closer to the convergence values.

Furthermore, the lack of elements covering the prism in the y direction proved to be exceptionally detrimental in the calculation of transverse stress σ_{yy} when coupled with a large lumping factor value: in fact, the increase in the number of elements per layer did not improve the result with a fixed lumping factor of 125, These problems were not as striking in the longitudinal stress, due to the larger number of elements in the x direction.

The justification behind the analysis of node (B) arose due to Software #1's meshing strategy in the interface between the baseplate and the workpiece. Generally, mechanical contact between two surfaces is modelled through the establishment of a *master* and a *slave* surface, enabling the formulation of a stiffness matrix that ties two otherwise incompatible meshes [60]. Because this contact influences the validity of the remaining systems, it is common to perform a mesh refinement near the interface, by increasing mesh fineness, using different shape functions or element types altogether, keeping in mind that the direct transition between different element types introduces numerical *noise* in the contact stress solution [61].

However, a mechanical contact case is not the only scenario in which mesh refinement is advised to take place: in fact, Software # 1 avoids formulating contact entirely by considering the baseplate-component system as one unique part, and modelling the material deposition through nodal activation methods. This approach has the advantage of eliminating the computationally intensive contact analysis, but it is common for very large stress gradients to arise near the interface and geometrical complexities such as sharp corners, as shown in Figure 4.4b, implying the mesh would benefit from a larger number of elements in the region.

Additionally, the resulting meshes are often characterised by elements with varying sizes, as the baseplate is usually significantly larger than the workpiece, thus benefiting from transition elements. Moreover, the objective of the transition elements is ensuring continuity and compatibility conditions between finer meshes and coarser meshes, elements with different shape function orders and/or different types [62]. Furthermore, Figure 4.5 schematically shows the evolution between a coarser mesh, introducing the concept of *hanging nodes*, which consist of nodes that are not shared across all elements within a specific boundary [63]: these may present a problem if the primary nodal variables are not consistent throughout the connected mesh and appropriate formulations have been established [62], but are computationally light alternatives and can assure a mesh subdivision through a direct process.

Matching interpolations between adjacent elements can be created through penalty methods, Lagrange multipliers, Nitsche's method or multi-point constraints [64], but come at the cost of a larger restriction of the solution field [63]. Hence, several developments have been made to formulate transition elements capable of handling the adaption between different elements: Gupta (1995) provided irregular meshing options for two-dimensional problems [65], later extended by Morton et al. (1995) for three-dimensional applications [66]; Provatidis (2006) constructed piece-wise linear functions, cubic B-splines and Lagrange polynomials [67]; Provatidis (2012) also analysed the importance of internal nodes in convergence rates [68]; Baitsch et al. (2009) developed a transition element through piece-wise polynomials [69], while Dohrmann et al. (1999) established transition elements between tetrahedral and hexahedral elements [70].

Therefore, the analysis of node (B) arises as a measurement of residual stress in elements that are relatively distant from the contact surface between the baseplate and prism and the subsequent stress gradient, in an area where numerical noise originated by the presence of hanging nodes is not immediate: Figure 4.4b displays a section cut of the prism, along a xz plane for $y = 5\,\text{mm}$, to highlight the refinement of the mesh.

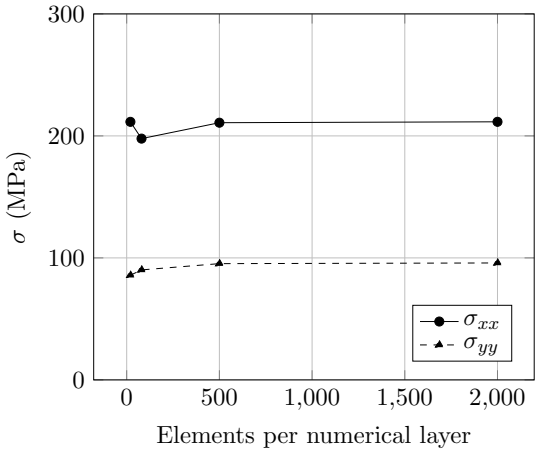

(a) Lumping Factor of 125

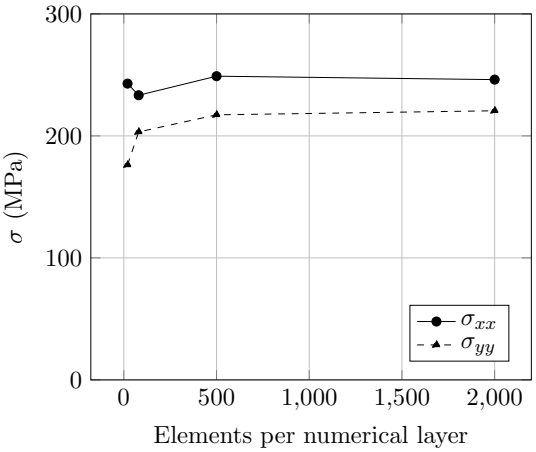

(b) Lumping Factor of 50

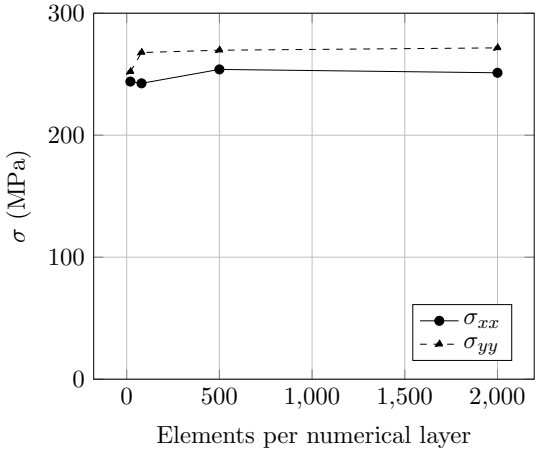

(c) Lumping Factor of 25

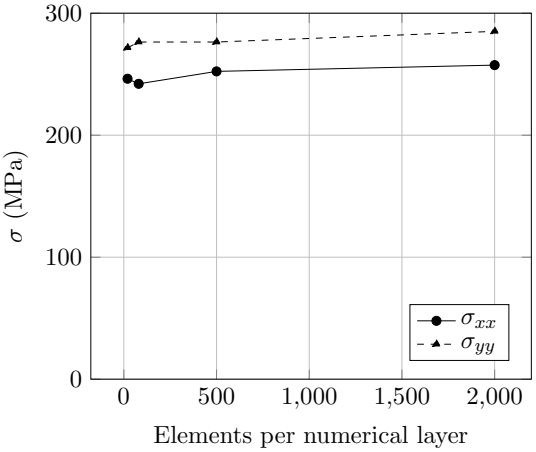

(d) Lumping Factor of 10

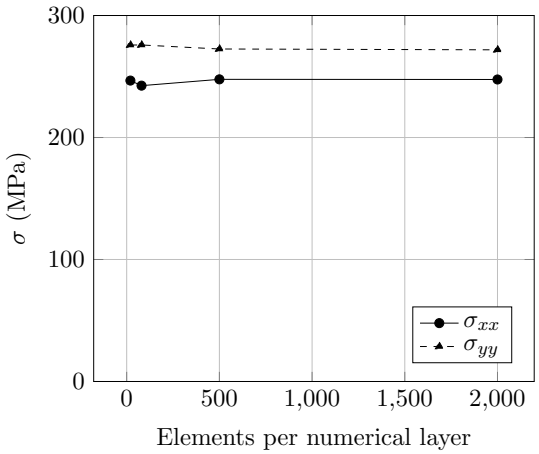

(e) Lumping Factor of 5

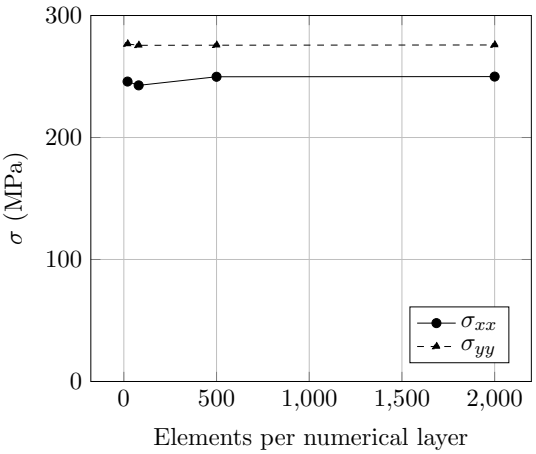

(f) Lumping Factor of 2

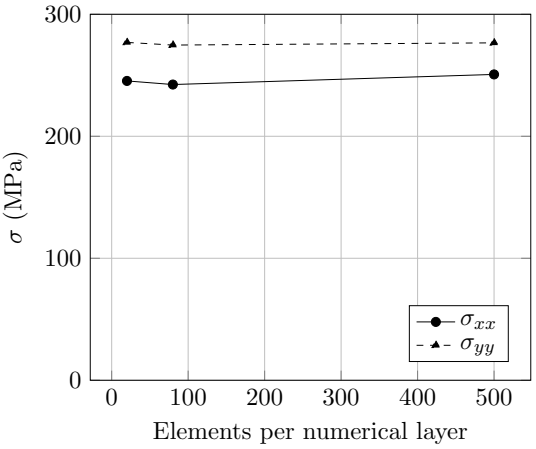

(g) Lumping Factor of 1

Figure 4.2: Evolution of longitudinal σ_{xx} and transverse σ_{yy} stresses in node (C).

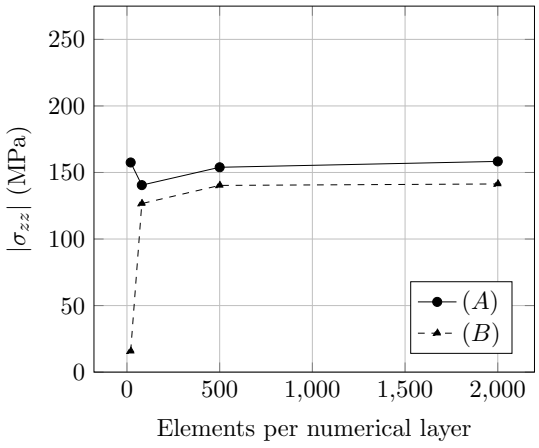

(a) Lumping Factor of 125

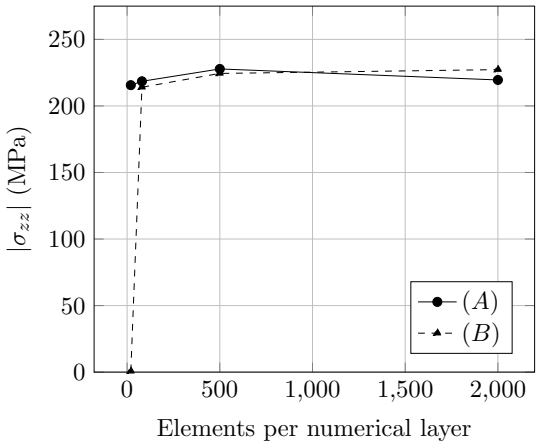

(b) Lumping Factor of 50

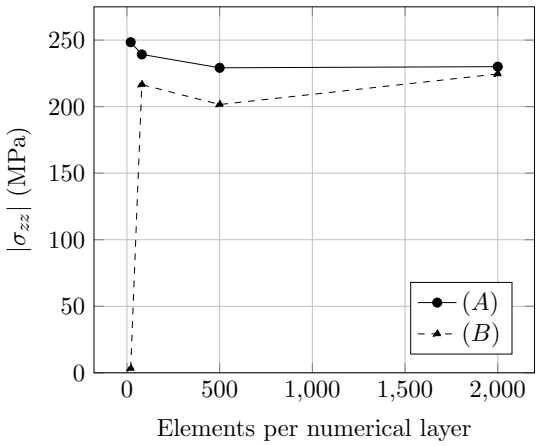

(c) Lumping Factor of 25

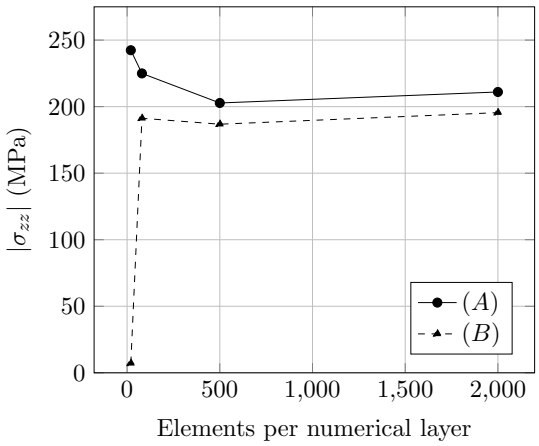

(d) Lumping Factor of 10

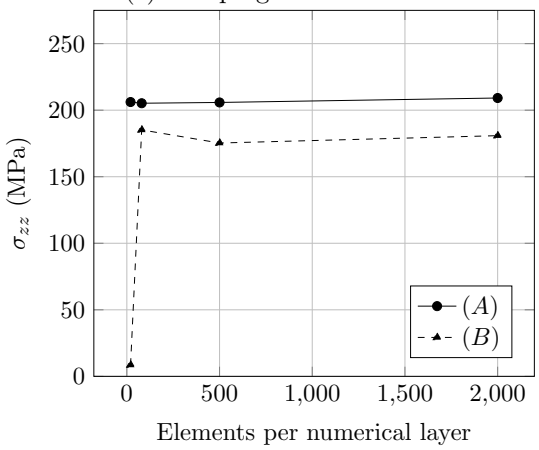

(e) Lumping Factor of 5

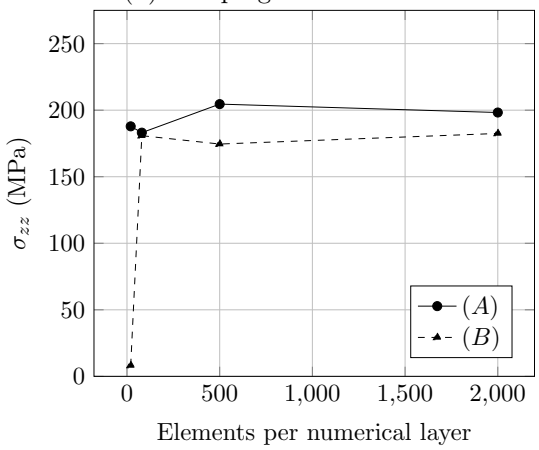

(f) Lumping Factor of 2

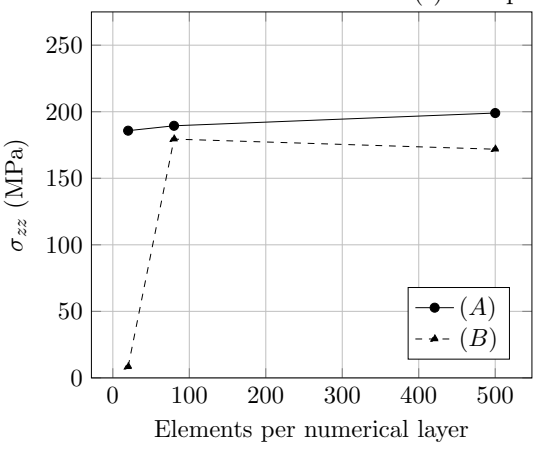

(g) Lumping Factor of 1

Figure 4.3: Evolution of out-of-plane stresses σ_{zz} in nodes (A) and (B).

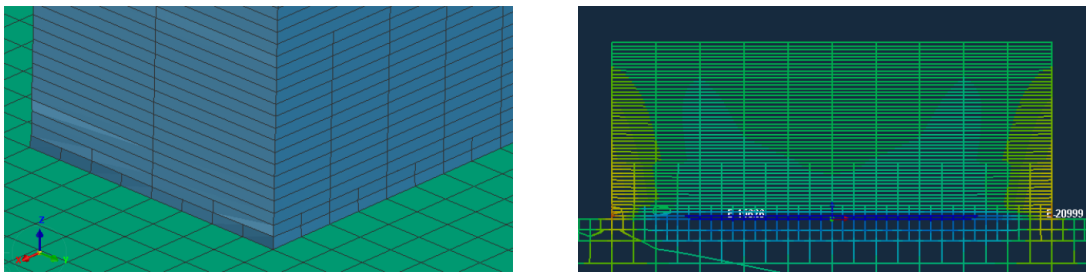

(a) Refinement details

(b) σ_{zz} distribution in wireframe

Figure 4.4: Software #1's mesh refinement in baseplate-workpiece interface, for mesh size of 5 mm and lumping factor of 25.

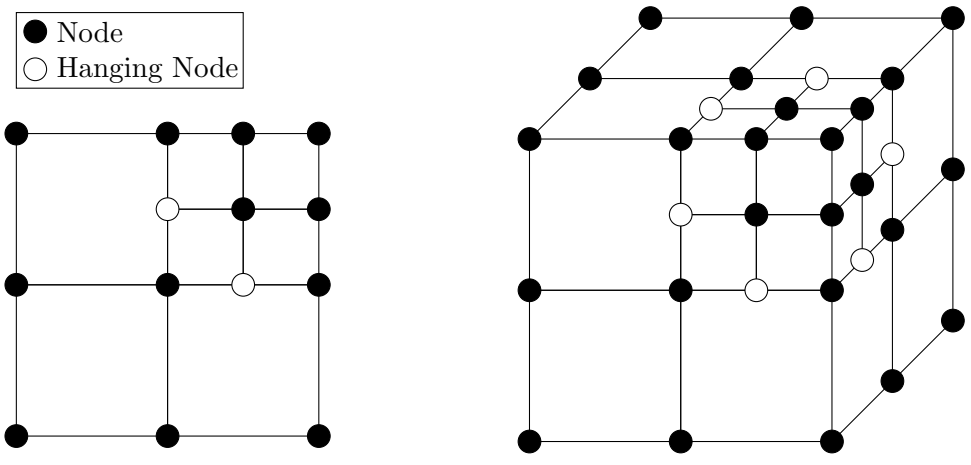

(a) Two-dimensional example

(b) Three-dimensional example

Figure 4.5: Schematic representation of meshes requiring hanging nodes (adapted from [63]).

4.1.2 Lumping Factor

In a similar fashion to the mesh size results, data is presented in Figures 4.6 and 4.7, regarding the evolution of the stresses in node (C) and in nodes (A) and (B), respectively. While in Subsection 4.1.1, the convergence criteria was chosen to be the value for the most refined mesh for each lumping factor, in this Subsection the difference is calculated using the value obtained with the highest number of simulated numerical layers for the same mesh size.

For the longitudinal stress σ_{xx} measured in node (C), results converged remarkably fast: in fact, according to the 5% criteria, results already converged in the second conducted simulation, corresponding to 10 simulated layers. In addition, transverse stresses, σ_{yy}, converged slightly slower, with the results fulfilling the 5% difference from 20 simulated layers onward. Furthermore, it is worth adding that an increase in mesh fineness did not improve the rate at which the transverse stresses converged, with the first and second values featuring percentage differences of around 65% and 20%, respectively.

Additionally, the out-of-plane stress σ_{zz} measurements in node (A), are visible in Figure 4.7b, where the absolute value of the stress σ_{zz} contradicted the trend set by the previous three simulations. This analysis underlines the explanation given in the beginning of this Subsection, where mesh refinement gives way to the appearance of numerical noise, and means that values taken from the interface surface between the baseplate and the component in Software #1 are very susceptible to the adaptive remeshing that takes place. This is further shown to be accurate in the faster convergence rates of the stresses taken in node (B).

Figure 4.7a highlights the aforementioned poor results for σ_{zz} in node (B); furthermore, the convergence curves of the vertical stress in node (A) display the same trend throughout the four mesh sizes, in which an uptick is seen until a lumping factor of 100: this is explained through the lack of numerical layers to accurately portray the stress evolution between the contact with the baseplate and the free surface at the top of the workpiece. In parts manufactured by LPBF, the core of larger deposited geometries tends to experience residual compressive stresses, balancing the tensile stress distributed near the surface area, accounting for the thermal-elastic-plastic deformation [11]: considering that, due to the boundary conditions of the top layer, in which its out-of-plane stress must fulfil $\sigma_{zz} = 0$, there is a significant stress gradient from the part's core in compression to the top layer in which there is an absence of residual stress. For simulations with a low number of simulated layers, there are too few nodes to accurately and smoothly model this evolution, misrepresenting the shape of the compression area in the core of the prism. Figures 4.8 attempt to represent this distribution.

As both the lumping factor and the mesh size contribute to the mesh fineness, three dimensional plots were constructed to provide a general view of how both of these parameters interact and result in a global convergence of values. The graphs shown in Figures 4.2, 4.3, 4.6 and 4.7 can be interpreted as cross-sections of Figures 4.9a-4.9d, in which cross-sections through yz planes match the graphs shown to highlight the mesh's size influence, while xz planes correspond to the lumping factor's impact. The representation is semi-logarithmic, where the x and y axis are logarithmic and the z axis is linear, to improve visibility and prevent a very asymmetrical visual approach.

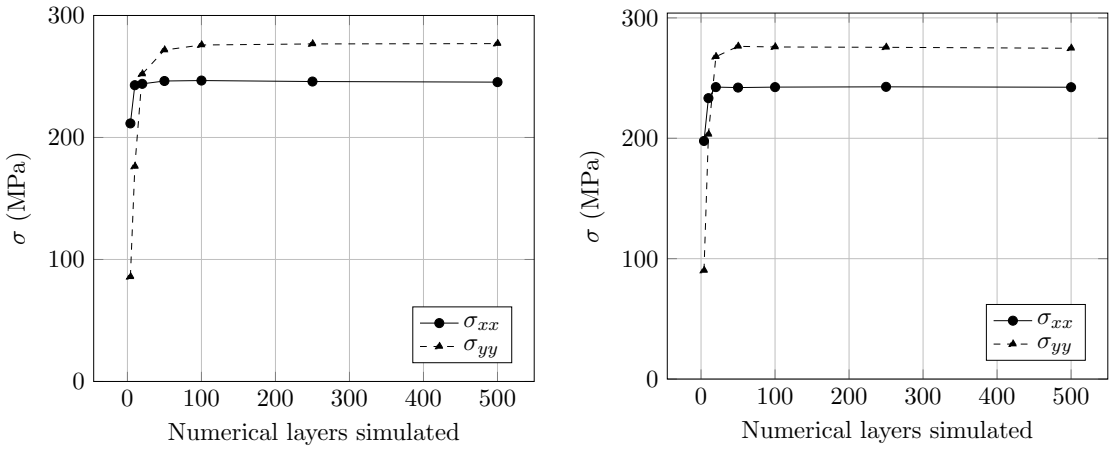

(a) Mesh size of 5.0 mm

(b) Mesh size of 2.5 mm

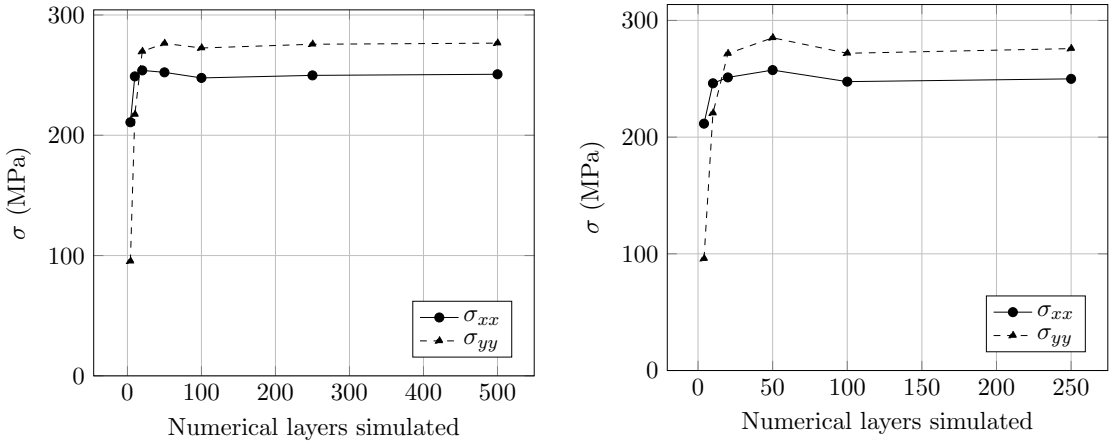

(c) Mesh size of 1.0 mm

(d) Mesh size of 0.5 mm

Figure 4.6: Evolution of stresses in node (C) with an increase in the number of layers that are simulated.

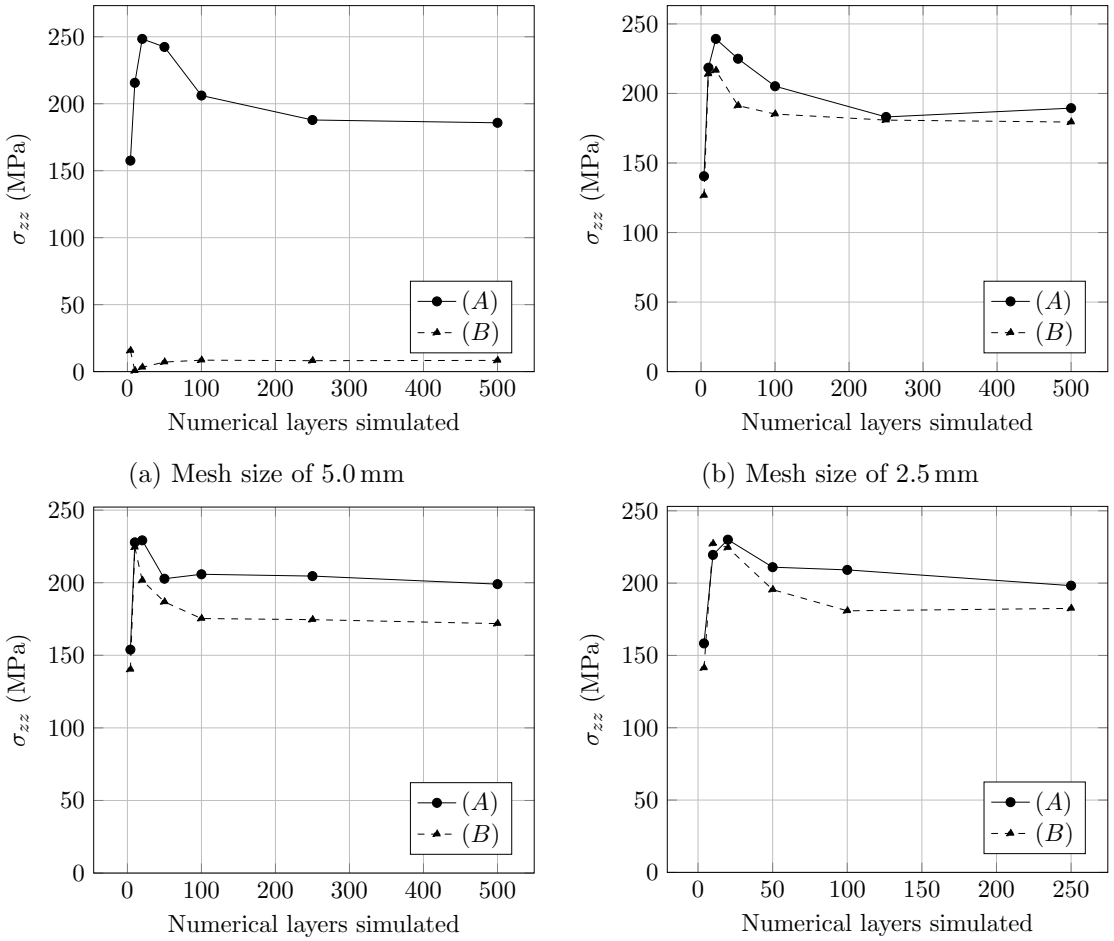

(a) Mesh size of 5.0 mm

(b) Mesh size of 2.5 mm

(c) Mesh size of 1.0 mm

(d) Mesh size of 0.5 mm

Figure 4.7: Evolution of stresses with an increase in the number of layers that are simulated.

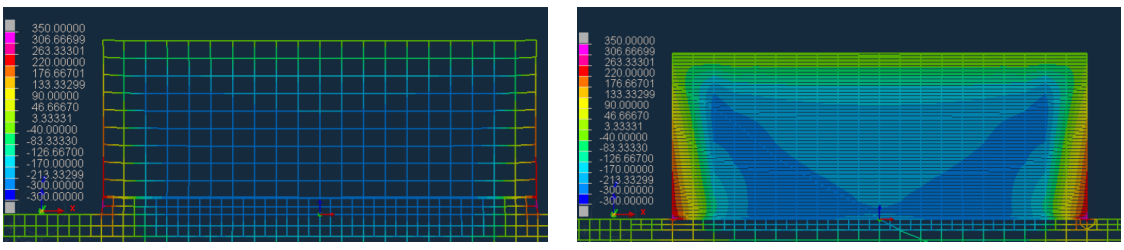

(a) Lumping Factor of 50

(b) Lumping Factor of 5

Figure 4.8: σ_{zz} configuration with a decrease in the Lumping Factor, for the same mesh of 2.5 mm, with section cut at $y = 5$ mm plane.

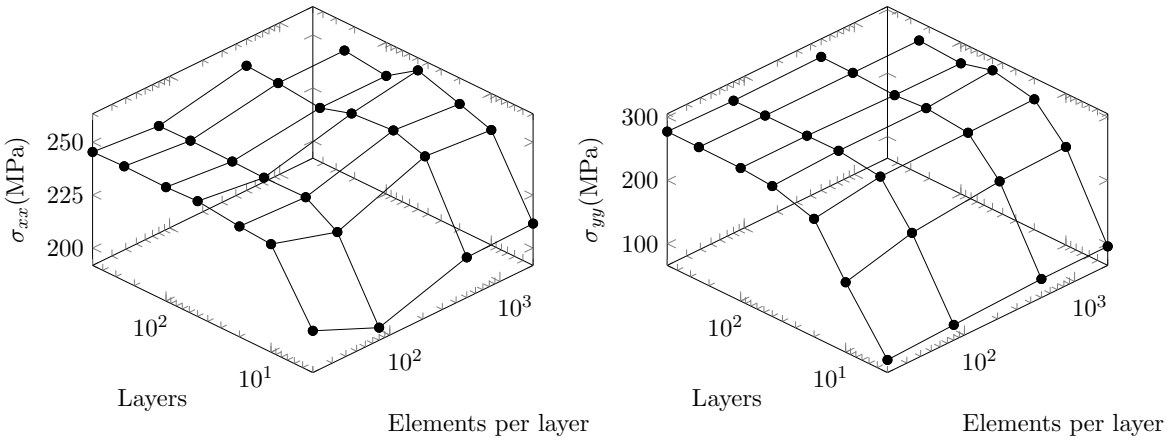

(a) σ_{xx} in node (C) convergence curve

(b) σ_{yy} in node (C) convergence curve

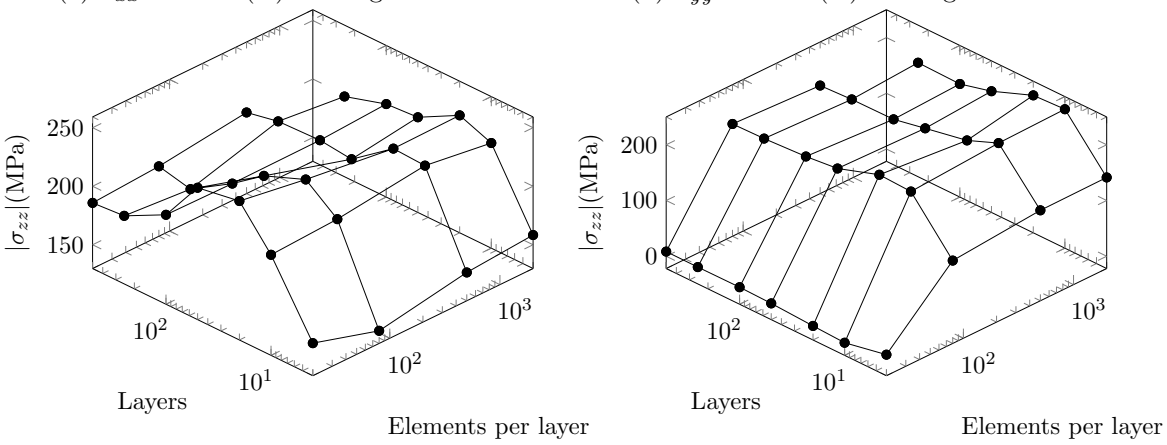

(c) $|\sigma_{zz|}$ in node (A)

(d) $|\sigma_{zz|}$ in node (B)

Figure 4.9: Three dimensional convergence curves.

4.1.3 Baseplate Thickness

This simulation group focused on the influence of the baseplate's thickness in the residual stress field experienced by the component. In fact, the thicker the plate is, the larger its stiffness is going to be, and the more capable it is to restrict the part's distortions during the multiple heating and cooling cycles.

The behaviour of plates - three dimensional solids in which two dimensions are considerably larger than the third - is governed by plate theory. Within plate theories, there are two widely regarded and used in engineering contexts: Kirchhoff's theory, which can be viewed as an extension of Euler-Bernoulli theory to plates, whose validity is considered to be for thickness-length ratios $t/b \leq 0.2$, respectively [71]; the other theory, named *Reissner-Mindlin*'s theory, or First Shear Deformation Theory (FSDT), relaxes the assumption of sections normal to the plate's mid-section remain perpendicular post-deformation, adding two new degrees of freedom. Therefore, the problem is more complex, but applicable to thicker plates (hence why some authors refer to it as *thick plate* theory [71]).

Through the constitutive equations given through FSDT, shown in Equations (4.1.3), the bending stiffness D for each baseplate could be computed for the material properties of 316L Stainless Steel given in Table 3.3. This was done to provide an insight into how the reduction of the baseplate's thickness impacts its ability to sustain small distortions during the imposed thermal stresses prevalent in the additive manufacturing process.

In addition, it should be noted that the software does not model the baseplate using a specific plate FEM formulation: Software #1's formulation is a generalised three-dimensional analysis, as explained in Section 2.2.2. However, a theoretical analysis of plate behaviour proves valuable in interpreting how a plate's thickness impacts its bending stiffness

$$\begin{Bmatrix} M_{xx} \\ M_{yy} \\ M_{xy} \end{Bmatrix} = D \begin{bmatrix} 1 & \nu & 0 \\ \nu & 1 & 0 \\ 0 & 0 & \frac{1-\nu}{2} \end{bmatrix} \begin{Bmatrix} \frac{\partial \phi_x}{\partial x} \\ \frac{\partial \phi_y}{\partial y} \\ \frac{\partial \phi_y}{\partial x} + \frac{\partial \phi_x}{\partial y} \end{Bmatrix}, \; D = \frac{Et^3}{12\left(1-\nu^2\right)} \tag{4.1}$$

, where M_{ij} values are unitary moments, ν is the Poisson's ratio, E is the Young's modulus, ϕ_x is the rotation along the negative y axis and ϕ_y is the rotation along the positive x axis. The stiffness values for the different values of the baseplate's thickness are displayed in Table 4.1. As observable in the constitutive matrix, D is the bending stiffness, as it directly relates the plate's warpage in the principal axis directions to the experienced unitary moments. Due to the fact that the bending stiffness varies with the thickness raised to a power of three, it is expected to see such a distinct difference in the the baseplate's rigidity, an observation highlighted in Figure 4.10a, where the longitudinal stress σ_{xx} increases by a factor of approximately 2.5 with the increase of the baseplate's thickness from its lowest to largest value. This is an expected phenomenon, as a stiffer baseplate is more suited to restricting the workpiece's deformations. Figure 4.11 displays the difference between the residual longitudinal stress field σ_{xx}, for two prisms built on top of two different baseplates with different thickness values.

Additionally, it is seen that the large strain hypothesis further raised longitudinal stresses, an expected phenomenon as the problem's formulation became more capable of handling large displacements associated with a flexible baseplate. Furthermore, as the baseplate's thickness increased, the disparity between the results with and without the large strain hypothesis decreased, which is coherent with the notion that the smaller

the experienced deformation is, the better suited infinitesimal strains are of accurately describing its behaviour.

Lastly, it can be observed that the general trend in stress evolution remained similar in the presence or absence of the large strain hypothesis.

Table 4.1: Baseplate bending stiffness.

Baseplate thickness (mm)	20	10	5	2
Bending stiffness D ($\mathrm{kN\,m^{-1}}$)	141.94	17.74	2.22	0.14

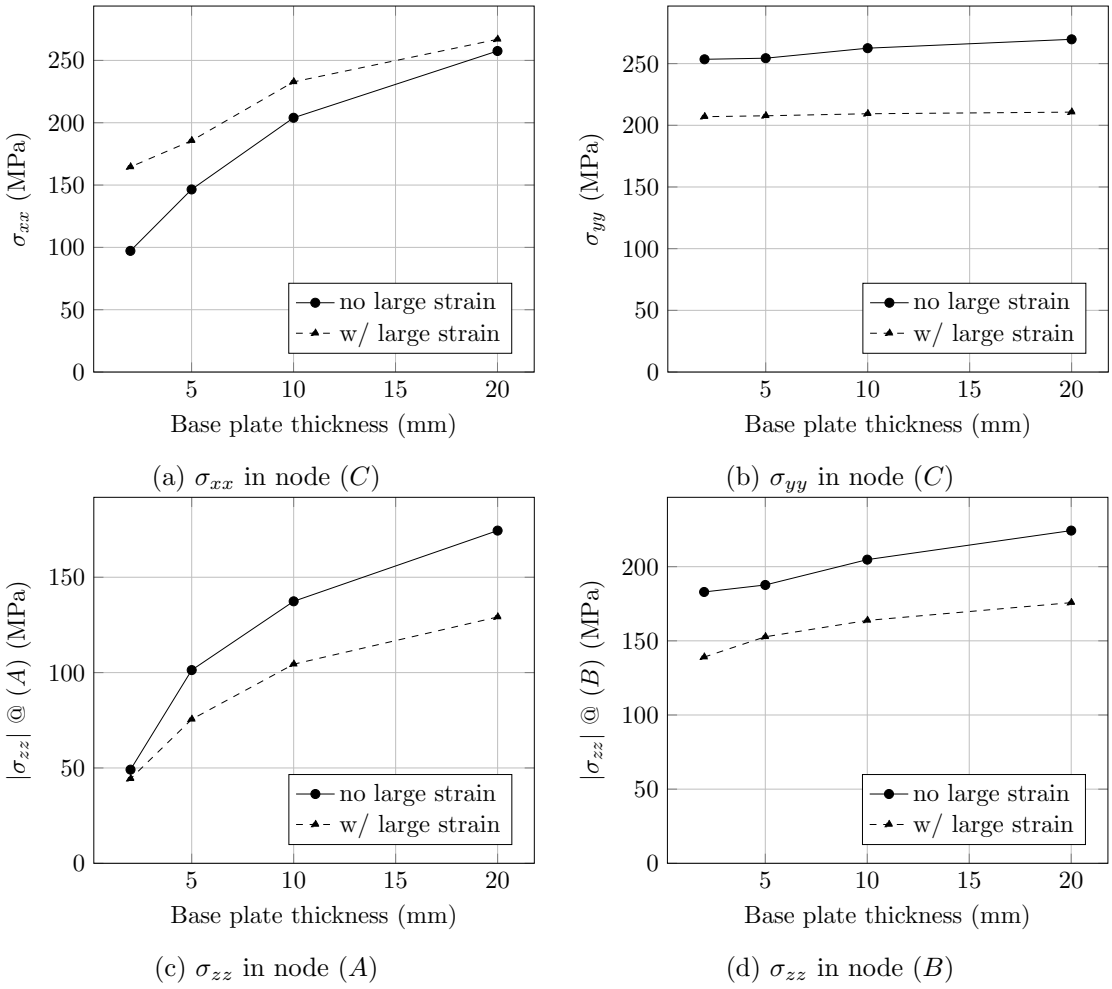

(a) σ_{xx} in node (C)

(b) σ_{yy} in node (C)

(c) σ_{zz} in node (A)

(d) σ_{zz} in node (B)

Figure 4.10: Evolution of stresses with an increase in the baseplate's thickness.

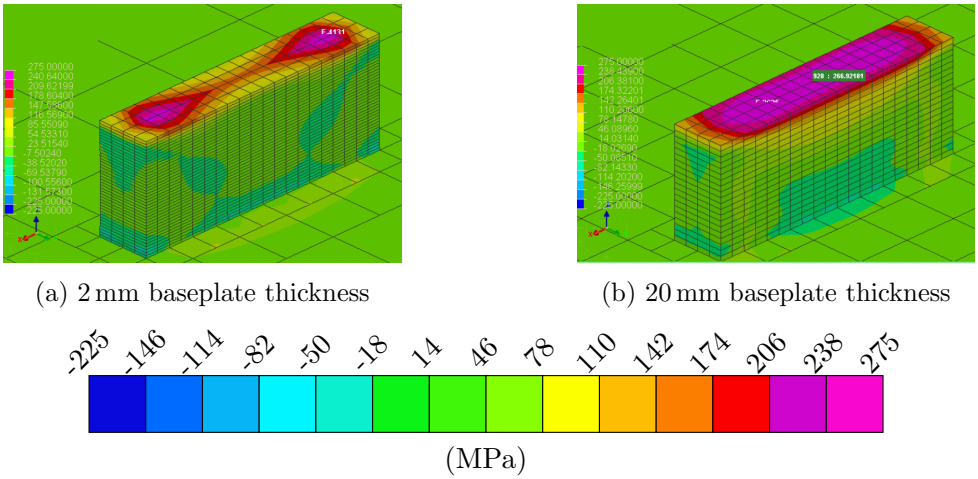

(a) 2 mm baseplate thickness

(b) 20 mm baseplate thickness

Figure 4.11: Longitudinal stress distribution σ_{xx} with large strain hypothesis.

4.1.4 Laser Speed

Laser speed affects the rate at which the metal powder is heated and a new layer is shaped. Together with the hatch space and laser power, the latter not being a process parameter in the simulation since the software in question does not allow the parametrisation of this variable, these variables contribute to how much energy is deposited unto the metallic powder, through Equation 4.1.4.

This Equation, while not a true measure of the actual energy density, gives a rough insight into how these parameters interact [12]. The objective of this simulation was to measure how residual stresses changed with an increase in the laser's scanning speed, taking advantage of the automatic parameterisation of data Software #2 offers, with results being displayed in Figure 4.12. As observed, the vertical stress σ_{zz} barely changes throughout the simulation, and Figure 4.12c attempts to better represent the decrease by showing the results in a smaller y axis scale.

The transverse σ_{yy} and longitudinal σ_{xx} stresses decreased as the laser speed increased, which is coherent with the findings of Mukherjee et al. (2017) that residual stresses are linearly reduced with the increase in scanning speed [36].

$$E_v = \frac{P_b}{v_s \cdot h \cdot t_{layer}} \tag{4.2}$$

where E_v is the deposited energy, P_b is beam power, v_s is scanning speed, h is the hatch distance and t_{layer} is the layer thickness.

While the actual interaction between the laser beam and the powder is crucial in determining the properties of the final workpiece, software aimed at calculating macroscopic phenomena circumvent these microscopical interactions by using the machine settings to determine the time interval pertaining to the build stage. This means that, instead of using the laser speed, hatch spacing and remaining parameters to calculate an energy deposition function, Software #2 instead defines the duration of each time step, controlling how much time each constructed layer has until it cools down and what temperature it reaches before the following layer is built.

With this in mind, the laser speed and the hatch spacing simulations measure the influence of the cooldown time interval in residual stress buildup, maintaining its relevancy

as it is necessary to determine how the machine settings influence this interval. Therefore, the lens through which the results are measured should take into account the decrease in layer build time.

Both the longitudinal and transverse stresses decrease, as previously mentioned, with σ_{yy} experiencing a more significant reduction. Moreover, when the time interval between two consecutive heat cycles decreases, the already deposited layer is prevented from experiencing a steeper thermal gradient by not fully establishing thermal equilibrium with the preheat and environment temperatures, reducing the thermal contraction experienced by a layer. Therefore, the amount of residual stress originated is reduced.

Figure 4.13 shows the evolution of the layer deposition duration with an increase in laser speed.

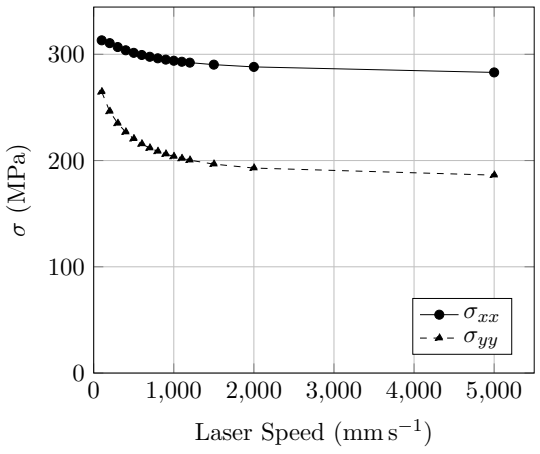

(a) Stresses in node (C)

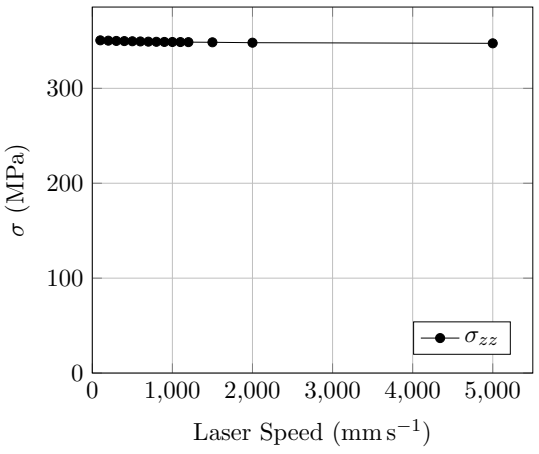

(b) Stresses in node (A)

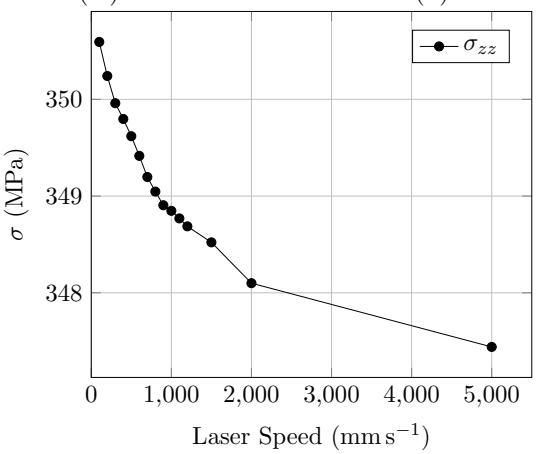

(c) Stresses in node (A), with more fitting scale

Figure 4.12: Evolution of stresses with an increase in laser speed.

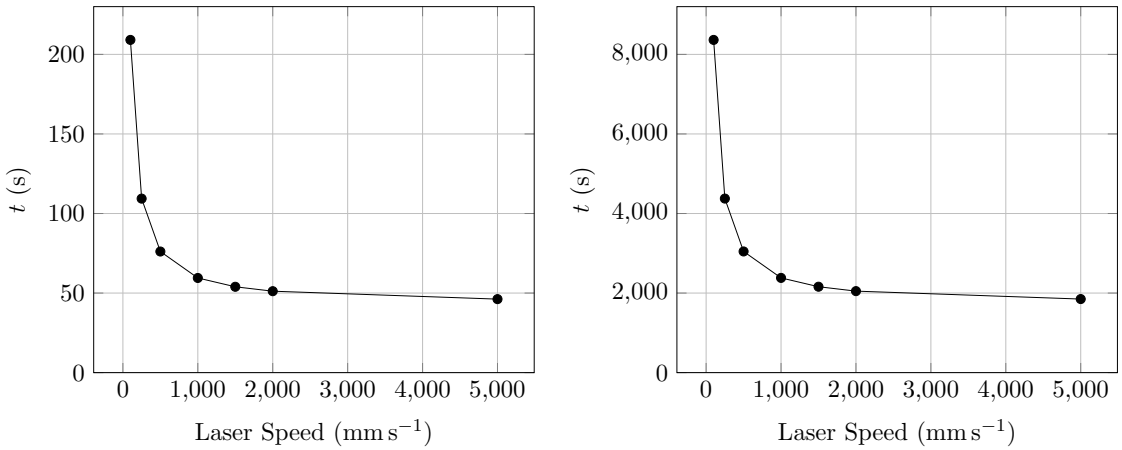

(a) Evolution of layer time steps

(b) Evolution of build stage time

Figure 4.13: Laser speed influence on time step creation.

4.1.5 Hatch Spacing

As observed in Figure 4.14a, the residual stresses too decrease with the increase of hatch spacing, except for the vertical stresses in point (A), in an analogous fashion to the laser speed parametric study.

The transverse stress σ_{yy} experiences a 16.2% decrease, when the hatch spacing is increased from 50 µm to 500 µm, and its configuration can be seen in Figures 4.15a-4.15b.

This underlines the software's use of these simulation variables, along with the other machine settings used in the weakly-coupled thermal-structural analysis, solely in the calculation of the time step between a new layer deposition, its cooldown and subsequent reheating, and not for laser beam-powder interactions. To highlight this decrease of the time step with the increase in hatch spacing, Figure 4.16 is shown, where the thermal history during the build stage for two different hatch spacing values are displayed, complemented by the evolution of the time step in Figures 4.17a-4.17b.

Additionally, the decrease of the residual stresses' magnitude with the cooldown time's diminishing is consistent with the theoretical considerations explored in Subsection 2.1.7, where the decrease of cooldown time diminishes the layer's shrinkage associated with its decrease in temperature, decreasing the amount of induced tensile strain.

As observable in both Figures 4.12b and 4.14b, the vertical stress experienced in node (A) suffered minimum variation throughout the experience, an observation coherent with the theory, as Software #2 does not calculate the thermal energy introduced in the system, but rather defines the deposited layer to be at the material's melting point: therefore, unlike the subsequent layers whose cooldown time reduction decreased the tensile strain, the first deposited layer experienced the usual compressive cycle, causing a negligible difference.

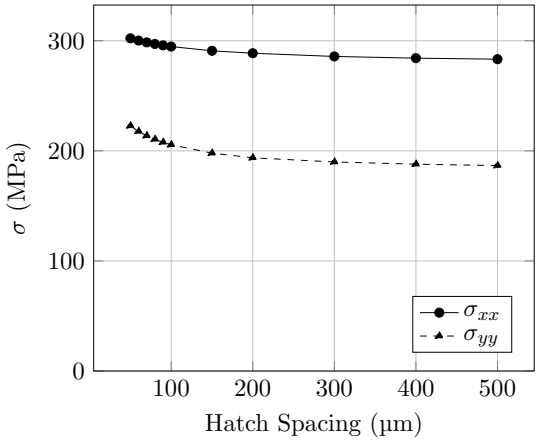

(a) Stresses in node (A)

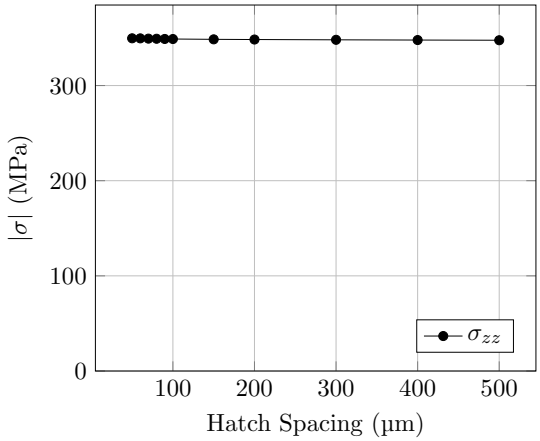

(b) Stresses in node (C)

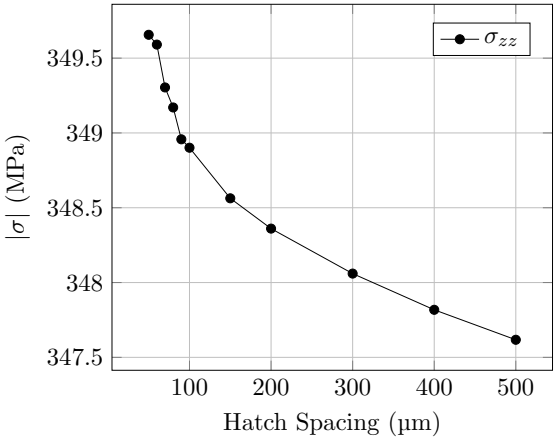

(c) Stresses in node (C), with more fitting scale

Figure 4.14: Evolution of stresses with an increase in hatch distance.

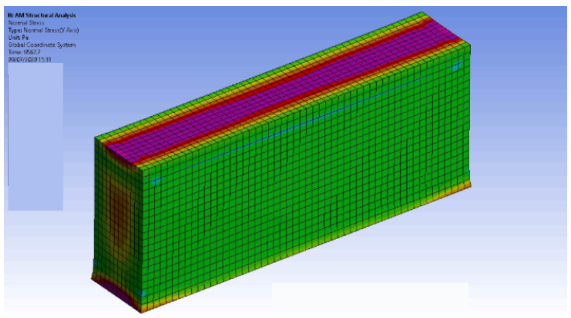

(a) Hatch Spacing of 50 µm

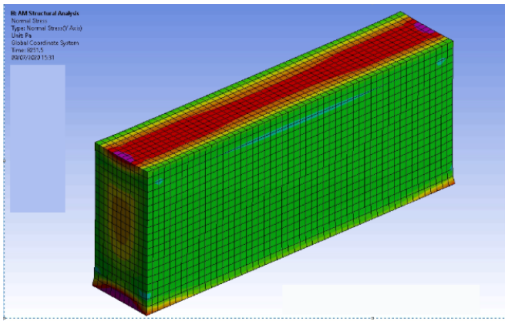

(b) Hatch Spacing of 500 µm

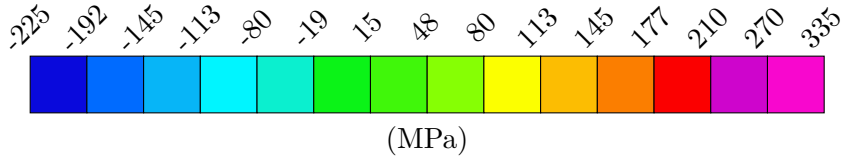

Figure 4.15: Transverse stress σ_{yy} field with different hatch spacing values.

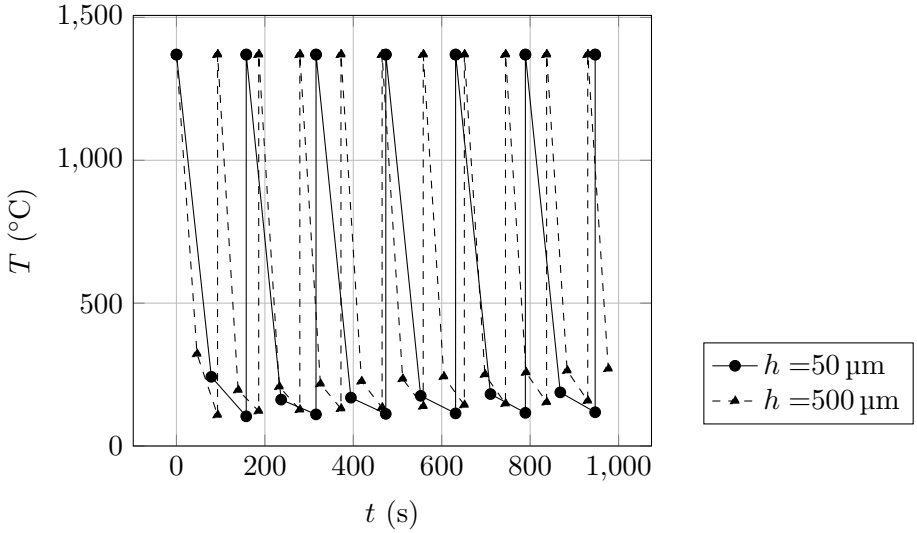

Figure 4.16: Evolution of temperature steps with hatch distance.

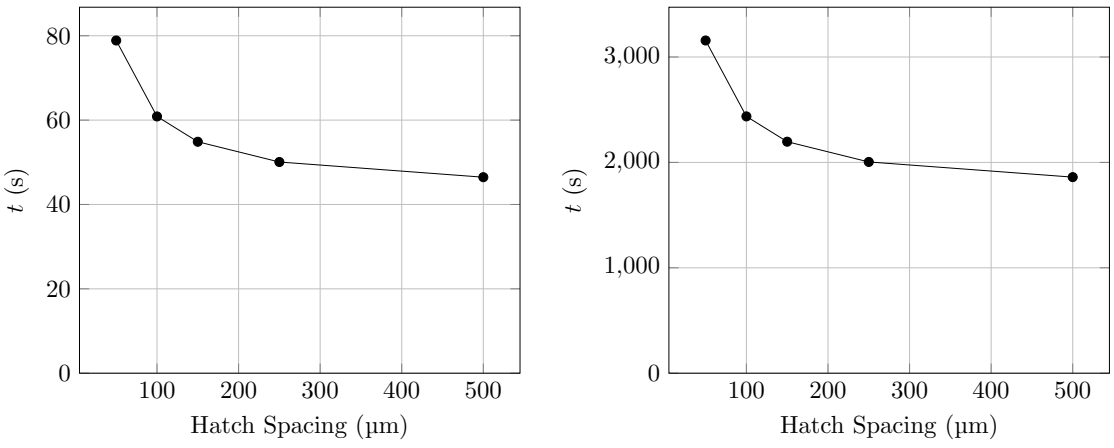

(a) Evolution of layer time steps

(b) Evolution of total build stage time

Figure 4.17: Hatch spacing influence on time step creation.

4.1.6 Preheat temperature

Preheat temperature control is one of the most widely adopted methods of reducing residual stresses during the AM process, as it decreases the thermal gradients between the laser and the workpiece [12]. Buchbinder et al. (2014) experienced a reduction of nearly 10 mm in distortion of SLM aluminium produced parts by baseplate preheating to 250 °C [72], while Shiomi et al. (2014) witnessed reduction of up to 40% in residual stresses by heating the baseplate to 250 °C [73].

In Software #2's framework, this condition is controlled both by the temperature itself, which is a user-controlled variable, and by the geometric boundary it is applied to: all simulations conducted in this software package defined the bottom plane of the baseplate to have a constant temperature, as Figure 4.18 schematically illustrates.

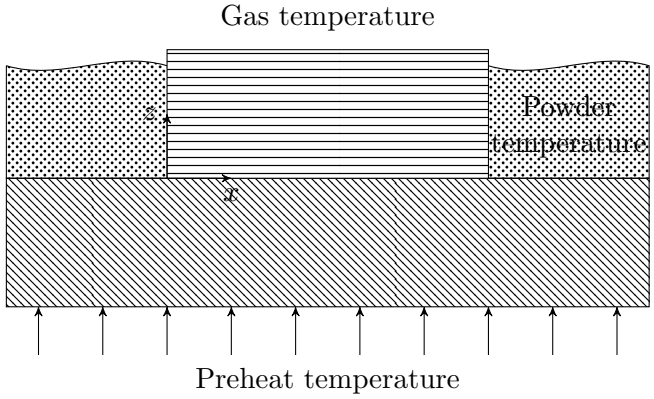

Figure 4.18: Schematic representation of the thermal boundary conditions.

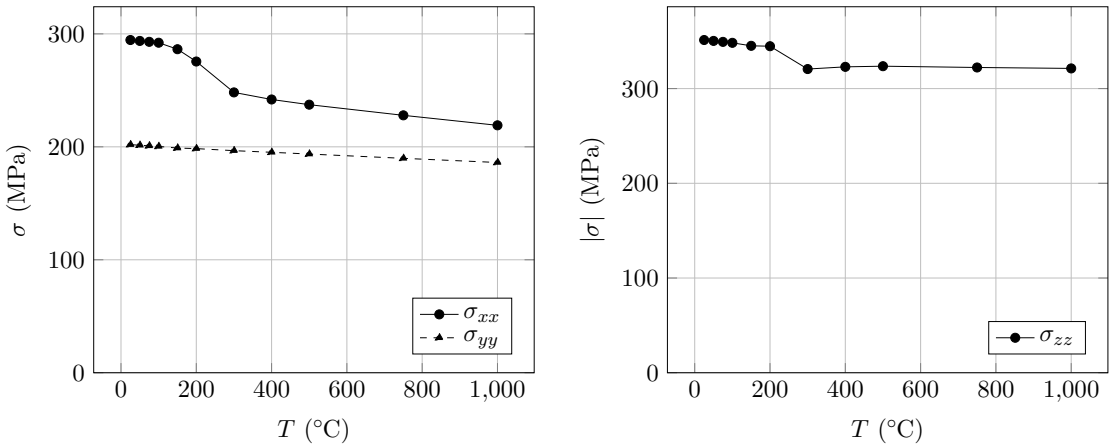

(a) Stresses in node (C)

(b) Stress in node (A)

Figure 4.19: Evolution of stresses with an increase in preheat temperature.

4.1.7 Cooldown temperature

This simulation group was aimed at measuring the effect of the cooldown temperature, which comprises the final steps of the simulation after all the material has been solidified, and achieves thermal equilibrium with the environment. The result of this simulation, unlike other parametric studies, did not display much difference for the discussed temperature values, with the only discernible variation being a slight increase in the longitudinal residual stresses, as observed in Figure 4.20a. The residual stress in the vertical direction can be observed in Figure 4.20b.

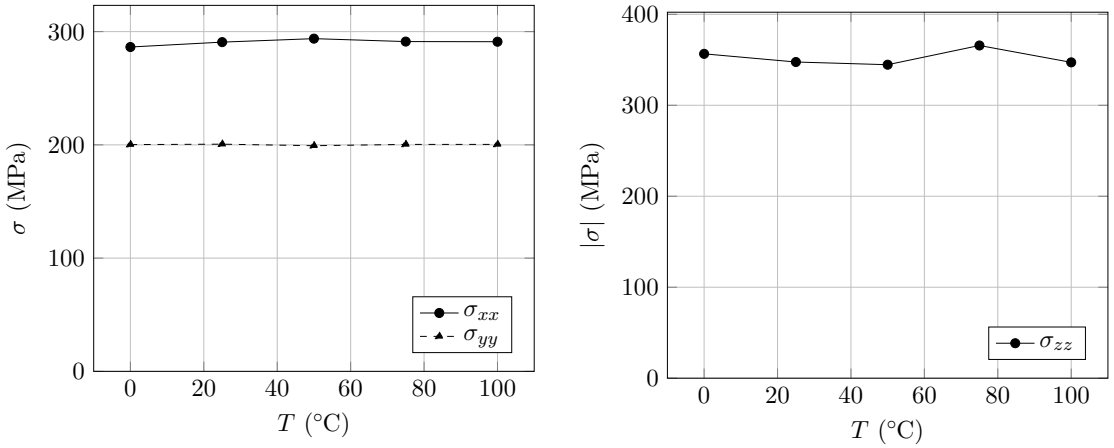

(a) Stresses in node (C)

(b) Stress in node (A)

Figure 4.20: Evolution of stresses with an increase in cooldown temperature.

This slight increase in residual stresses in the longitudinal direction σ_{xx} is explained through the temperature behaviour of the component: the preheat thermal boundary applied directly to the baseplate (which remains the same throughout all conducted simulations, fixed at 100 °C) as explained in Subsection 4.1.7, is maintained throughout the build process until all material has solidified, in which the workpiece is left to cool down until the defined temperature. In this period, tensile stresses develop, as aforementioned in Subsection 2.1.7; however, as the cooldown temperature increases, the global shrinkage of the workpiece decreases and stresses increase.

4.2 Simulations aimed at comparing software

4.2.1 One layer

The initial motivation for the simulation of only one layer was an error in which Software #1's results for the final simulated layer, when measured in an intermediate loading step, appeared inflated in regards to previous layers under the exact same conditions. This error, among other questions regarding the Software that are beyond the scope of this text, prompted a meeting with the development team's representatives, which eventually lead to the solution of the problem: in fact, the initial idea that the residual stresses obtained were artificially enlarged was wrong, but rather the previous values were wrongly calculated. Software #1 handles nodal post-processing through nearby Gauss points, including points currently whose values are not calculated, prompting solutions that are effectively halved.

With this question no longer being relevant, this simulation maintained its significance for the points explained in Chapter 3: it emphasises the problem's boundary conditions,

the way both packages handle the baseplate-component interaction and the user-defined material within Software #2, according to Software #1's internal library. It is important to note that the used material is 316L Stainless Steel according to the properties displayed in Table 3.5, and therefore its properties are not temperature dependent, even though Software #2 allows its definition, as its purpose is creating the conditions as similar as possible, across both packages.

The results for the simulation were extracted from point (D), in coordinates $(25, 5, 1)$, which corresponds to a point at the top of the unitary layer, in the centre of cross-section. Figure 4.21 schematically displays this point.

The results are shown in Figure 4.22 and Table 4.2. A distinction is made between two extracted results: *(i) Build values*, corresponding to residual stresses after the layer has been built, and its temperature has not yet achieved thermal equilibrium with the environment temperature; *(ii) Final values*, in which the entire system has undergone cooldown and reached thermal equilibrium with the remaining environment. The reasoning behind studying these two variables arose from achieving a more accurate comparison between both software packages, knowing both structure the evolution of the thermomechanical conditions differently. While Software #1 considers the build stage to be defined by the layer's thermal contraction with the decrease in temperature from the material's melting point to the chamber's temperature, Software #2 performs an initial build stage where the layer cools from its melting temperature, being at the same time exposed to a thermal preheat temperature and experiencing losses by convection. This build stage ends when all the material has been deposited, regardless of the temperature. The preheat temperature boundary condition is then removed from the baseplate, with the system being left to cool until the cooldown temperature is reached.

To better analyse how stress evolved with the temperature history, Figures 4.23a-4.23b were developed, with the former highlighting the temperature history with time, and the latter showing the evolution of the longitudinal and transverse stresses.

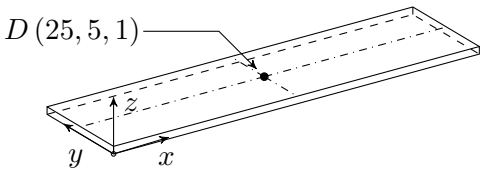

Figure 4.21: Definition of node (D).

Table 4.2: Stress values for the one layer case, for both software packages.

Variable	#1 (MPa)	#2**'s Build** (MPa)	Δ (%)	#2 **Final** (MPa)	Δ **Final** (%)
σ_{xx}	277.75	279.60	0.66	307.75	9.75
σ_{yy}	273.55	263.18	3.94	227.70	20.13

With the simulation setup and objectives outlined, it is noticeable that, despite the attempt to recreate the same conditions across these two platforms, there are still two main factors that differ: *(i)* contact formulation, as Software #1 does not model contact between both items while Software #2 does; *(ii)* the adaptive remeshing experienced in Software #1 that does not occur in #2. Both of these factors must be taken into account when looking at obtained data.

It can be observed through Figure 4.22 that the stresses obtained before the cooldown

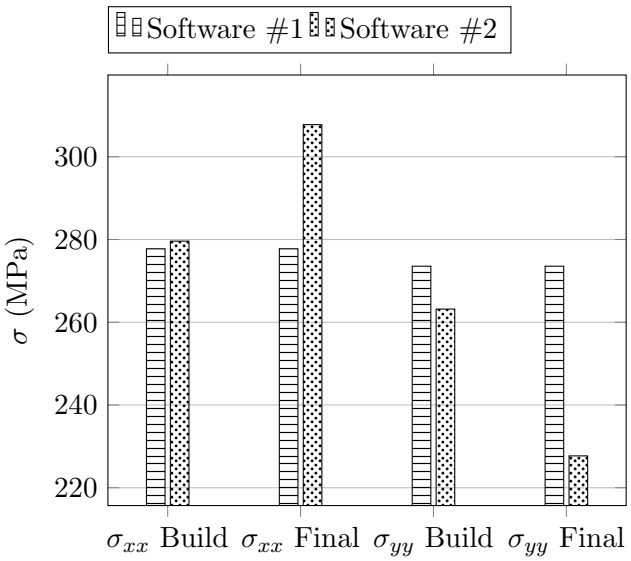

Figure 4.22: Bar plot with stresses obtained in node (D).

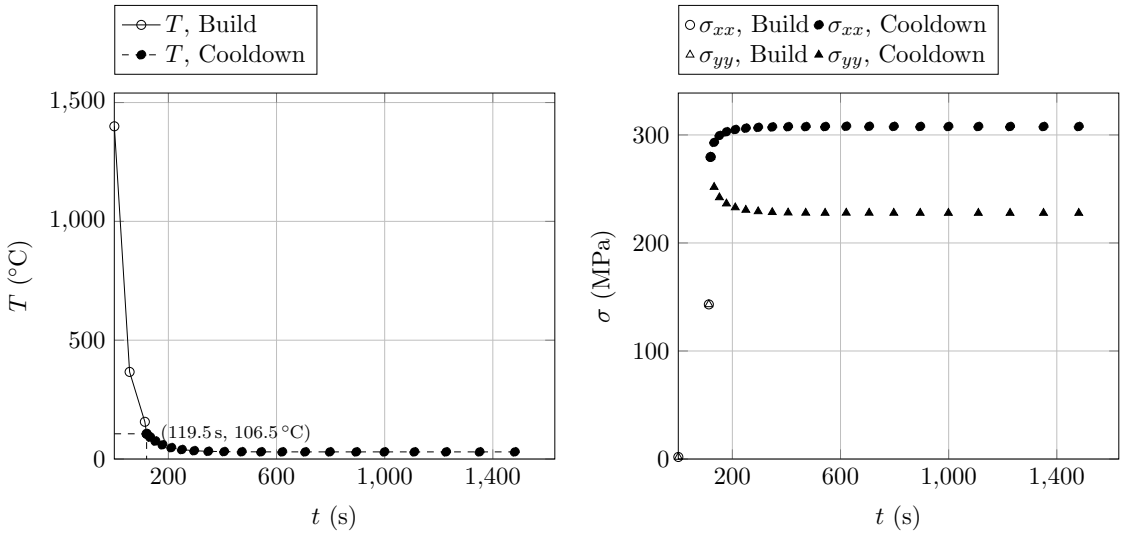

(a) Temperature evolution

(b) Stress evolution

Figure 4.23: Temperature T, longitudinal σ_{xx} and transverse σ_{yy} stress evolution with time, in single layer configuration.

initiated were much closer to Software #1's numerical results. This is expected, as said software does not compute the cooldown stage. However, it would not be expected for Software #2's longitudinal stress σ_{xx} values to be larger, as the temperature corresponding to this stage - $T = 106.5\,°C$ - is larger then Software #1's temperature at this stage - $T = 30\,°C$. Knowing that the thermal gradient relates to the experienced stress through the thermal expansion coefficient α and Young's modulus E, a larger temperature gradient would result in larger stresses. This is a simplistic approach to the problem, as AM simulation in this format is a more complex three-dimensional problem, and a potential explanation arises from Software #2's contact formulation providing a stiffer baseplate that further restricts the component's deformations.

Additionally, it is not expected for the transverse stress σ_{yy} to decrease after the

cooldown step for the same reasons explained in the previous paragraph. As the temperature gradient increases, residual stresses are usually expected to increase, which happens in the case of σ_{xx}.

Although these two aforementioned behaviours were not expected, the simulation's main objective - establishing an analogous case between both software's, with as close a mesh configuration as possible, equal component and baseplate dimensions, and material definition - proved to be successful in retrieving similar results, with the difference between Software #1 and Software #2 being 0.66% and 3.94% for the longitudinal and transverse stresses, respectively. Figures 4.24a-4.24d display the stress configuration evolution, showing the differences between the layer after the build stage and after the cooldown stage.

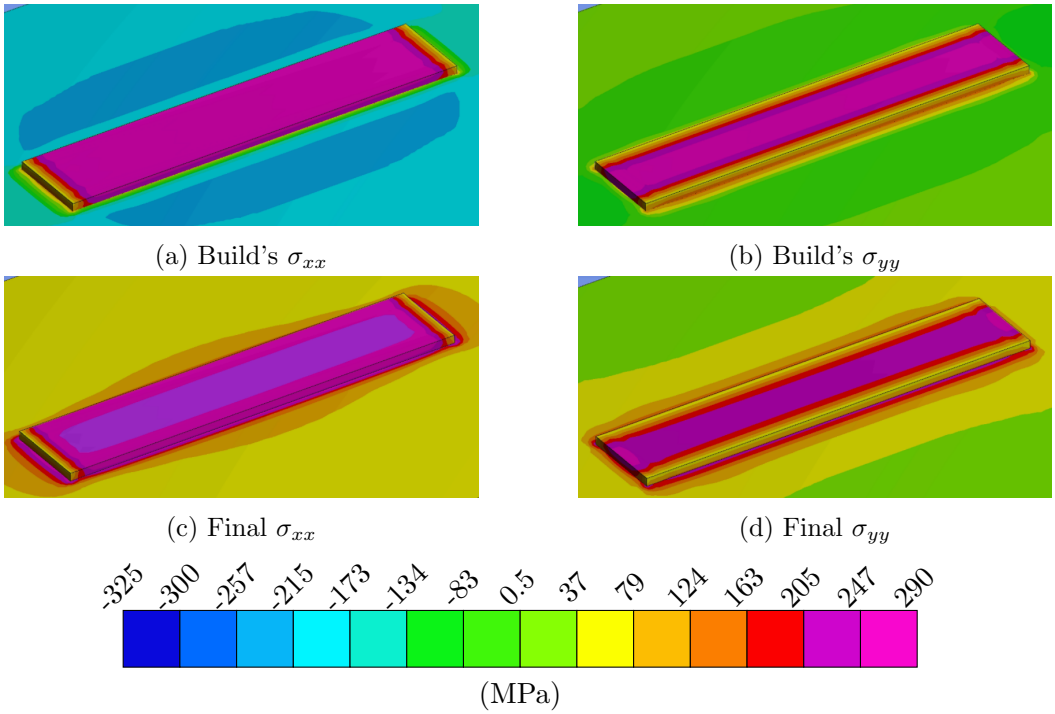

(a) Build's σ_{xx} (b) Build's σ_{yy}

(c) Final σ_{xx} (d) Final σ_{yy}

Figure 4.24: Stress configuration changes for two time steps, for Software #2.

4.2.2 Prism

With regards to the prism, two simulations were developed, both with elements with a cubic geometry: one is a coarse mesh, with a 5 mm mesh size, while the second mesh has a 1 mm mesh size. The choice of two simulations where the mesh features the same sizes in all dimensions was done as Software #2's Cartesian elements measure the same in the x, y and z directions, hence guaranteeing a similar mesh across both software packages. Figures 4.25a-4.25b represent the 5 mm and 1 mm meshes respectively, as defined in Software #2.

The results are shown in Figure 4.26 and 4.27, while overall stress distribution is shown in Figures 4.28a-4.28h.

Several trends can be observed in the direct comparison of values between simulations: firstly, the considerable discrepancy between the transverse stress σ_{yy} for the coarse 5 mm, which is almost null in both time steps of Software #2's simulation. This is expected, as the nodes situated in the middle of the top layer are not subjected to boundary conditions respective to the y direction, largely restraining the solution's variables, specially for the linear formulation of Software #2's elements.

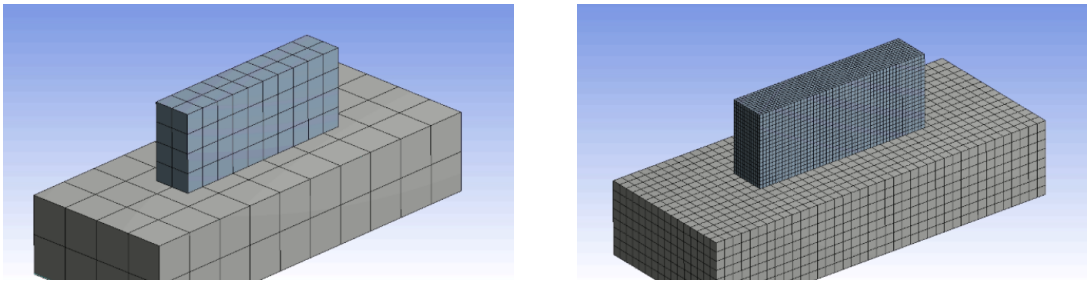

(a) Mesh of 5 mm (b) Mesh of 1 mm

Figure 4.25: Meshes used in prism comparison, as defined in Software #2.

Secondly, the difference between the values after the layer has been built and after the final cooldown step are not as striking as shown in the singular layer case, especially in the finer mesh. In fact, only the longitudinal stress σ_{xx} in this finer mesh has suffered slight compression, as the top layer's temperature decreased into the cooldown temperature of 30 °C.

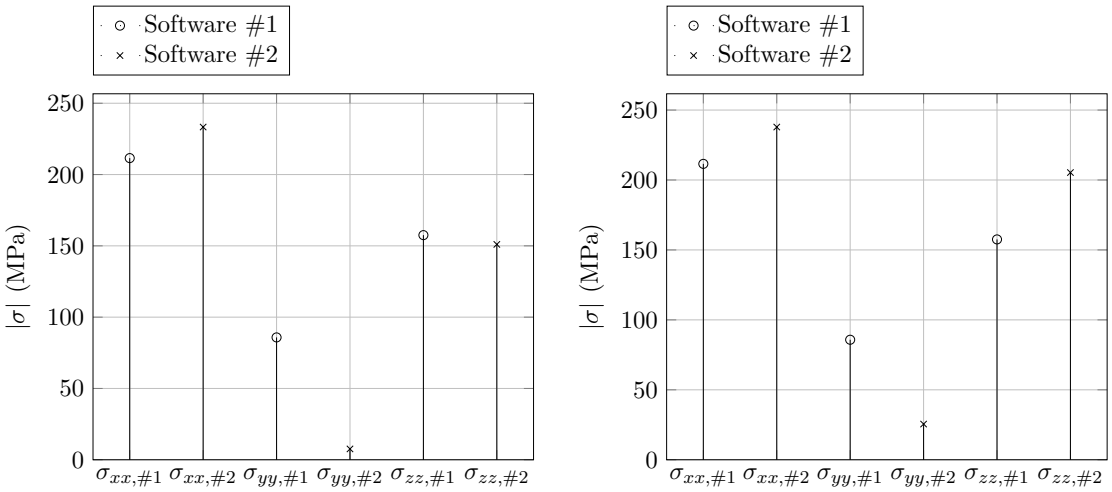

(a) After deposition (b) After cooldown

Figure 4.26: σ_{xx} and σ_{yy} stress values for node (C), and σ_{zz} for node (A), for a cubic 5 mm mesh.

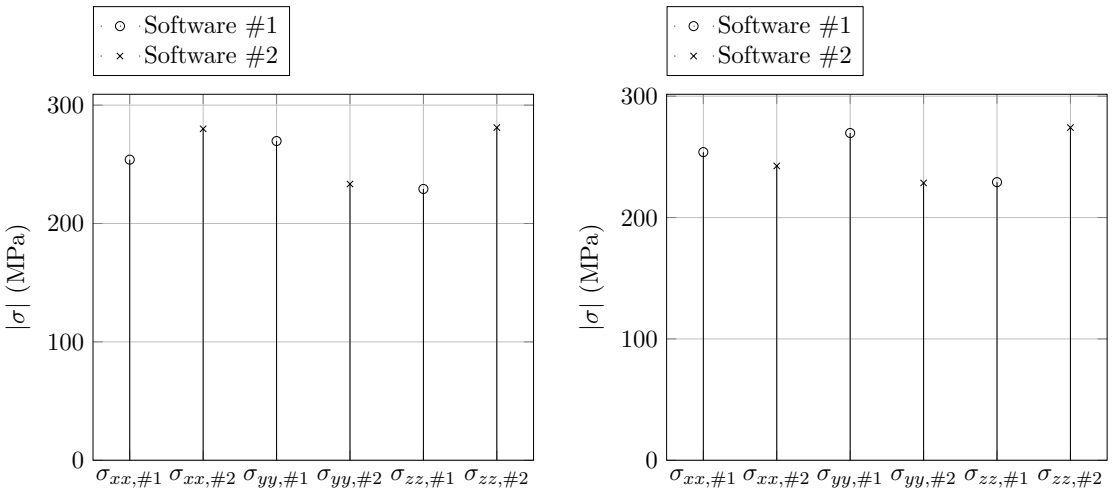

(a) After deposition

(b) After cooldown

Figure 4.27: σ_{xx} and σ_{yy} stress values in node (C), and σ_{zz} in node (A), for a 1 mm mesh.

Lastly, through Figures 4.28e and 4.28f, that detail the contour plot of σ_{xx}'s distribution across the prism, a considerable difference is observed, in which the longitudinal stresses in the surface of the prism, obtained from Software #2, are considerably larger than #1's.

To better understand this difference, a new node, called (E), was defined, situated in the middle of the lateral surface of the prism, as schematically defined in Figure 4.29.

In this node, the stress evolution and temperature evolution in function of time were plotted in Figure 4.30. This plot was chosen to neglect the initial instances in which the layer finds itself at melting temperatures, in order for the y scale pertaining to the temperature not to be widened, hampering the re-heating cycle's analysis, and therefore begins when the layer has been constructed and the second layer's construction is imminent.

As observed in Figure 4.30, the layer is subjected to multiple heating and cooling steps that result in an oscillation of longitudinal stresses by the same trend. Once the temperature decreases with the end of the build stage, there is a decrease in tensile forces, with residual stress reaching its lowest value, in the instant $t = 2259.8\,\text{s}$. This instant corresponds to the latest value before the cooldown stage begins, and residual stresses increase with the rise in the thermal gradient.

Retrieving the longitudinal residual stress field σ_{xx} for instant $t = 2259.8\,\text{s}$, a much closer configuration is achieved, when compared to Software #1. The results are displayed in Figures 4.31a-4.31b.

It is important to note that the conclusion that the longitudinal stress field σ_{xx} is more similar when the value obtained by Software #2 corresponds to the numerical solutions before the cooldown stage is applied, is coherent to the analysis made in Subsection 4.2.1.

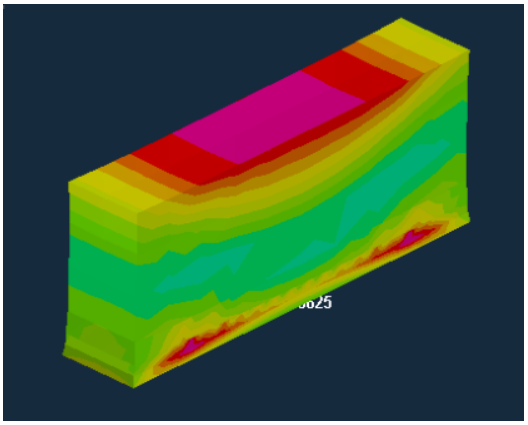

(a) Software #1's 5 mm mesh

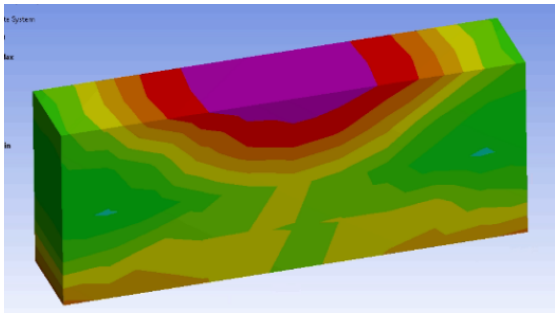

(b) Software #2's 5 mm mesh

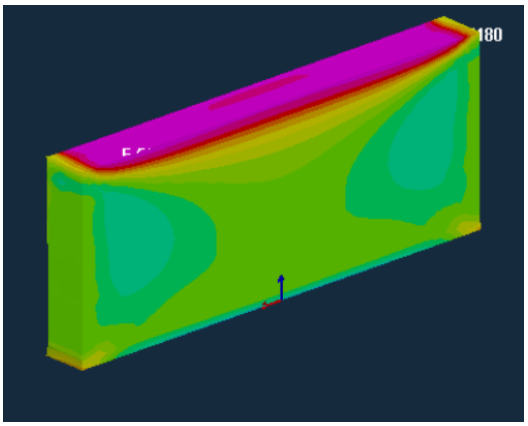

(c) Software #1's 5 mm mesh with section cut

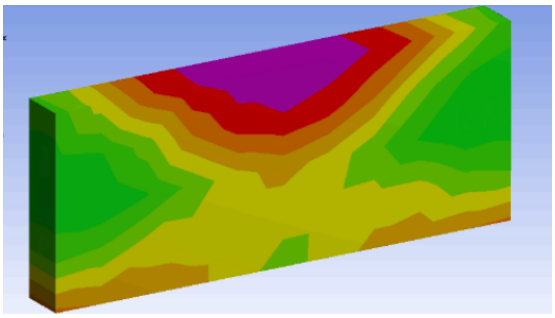

(d) Software #2's 5 mm mesh with section cut

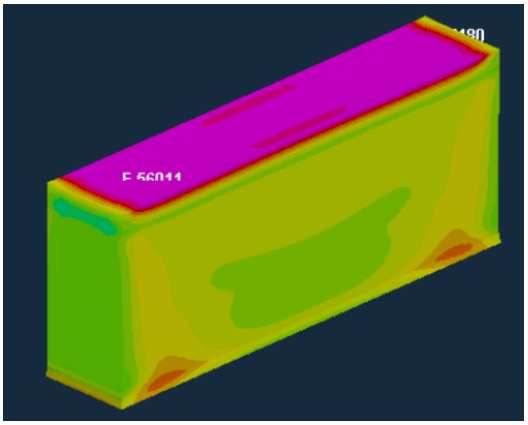

(e) Software #1's 1 mm mesh

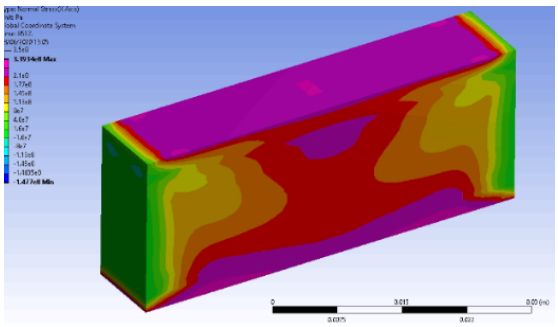

(f) Software #2's 1 mm mesh

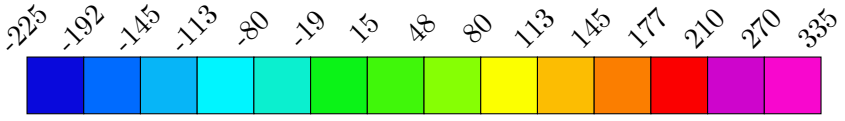

(MPa)

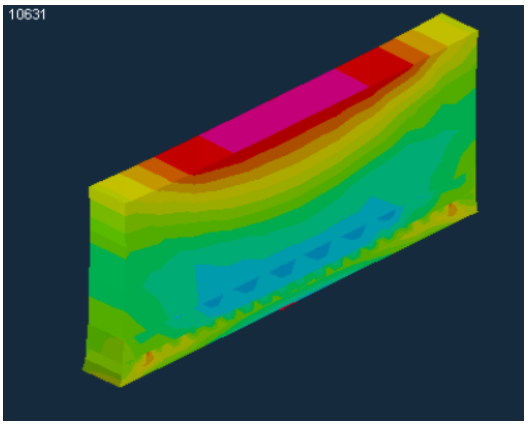

(g) Software #1's 1 mm mesh with section cut

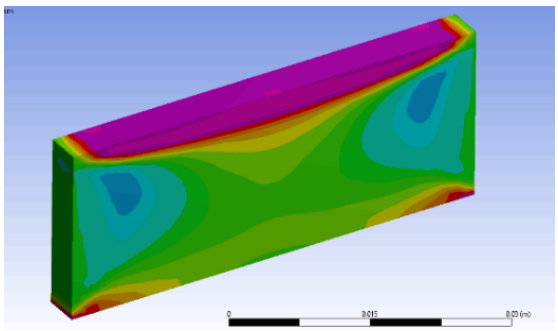

(h) Software #2's 1 mm mesh with section cut

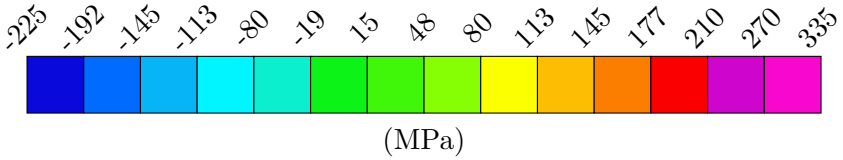

Figure 4.28: Longitudinal stresses σ_{xx} contour plots.

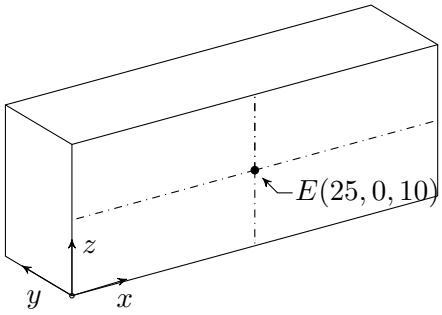

Figure 4.29: Definition of node (E).

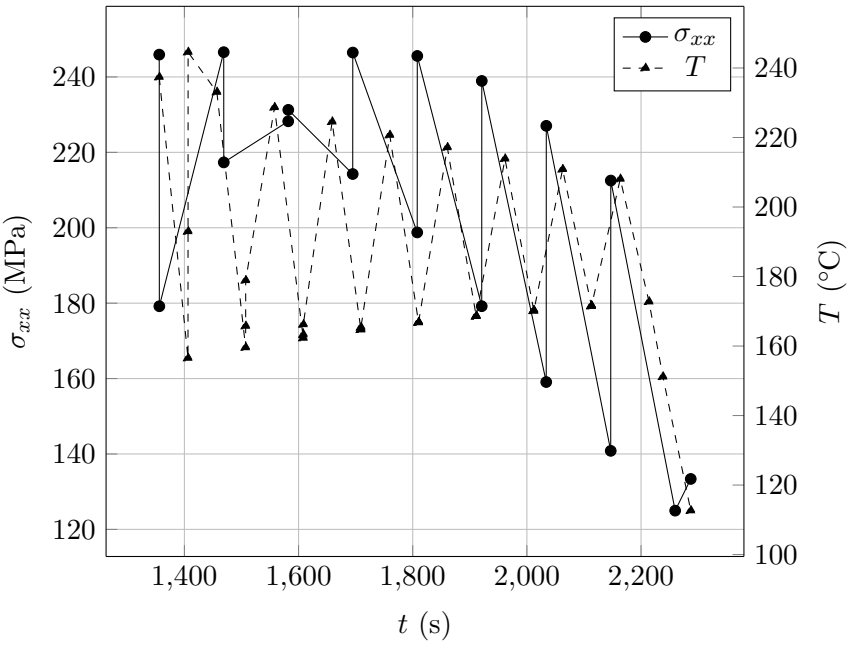

Figure 4.30: Longitudinal stress σ_{xx} and temperature T evolution with time, in node (E).

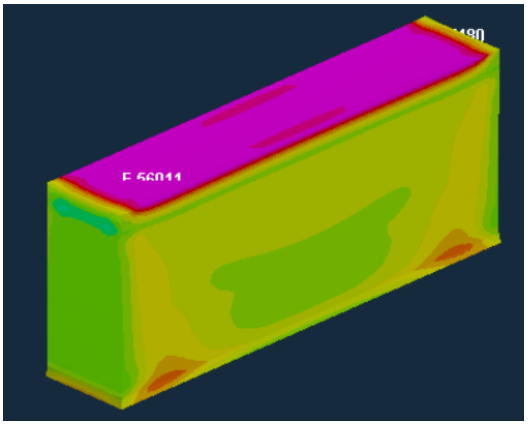

(a) Software #1's 1 mm mesh

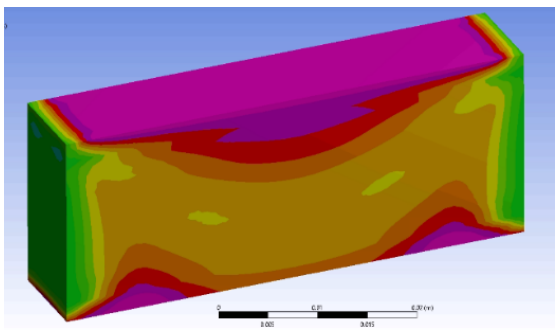

(b) Software #2's 1 mm mesh, before cooldown

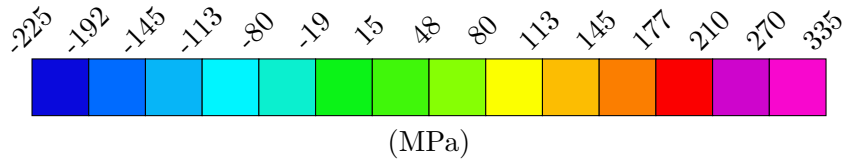

Figure 4.31: σ_{xx} comparison between Software #1 and Software #2, before cooldown.

4.2.3 Benchmark Bridges

The last simulations pertaining to a comparison between software packages was the simulation of the benchmark bridges, a component that encourages distortion due to its thin legs. Its complicated geometry poses a challenge in its meshing, as the thinnest legs measure only 0.5 mm in width, implying that a conforming Cartesian mesh should have a mesh size of the same dimension.

As an initial simulation group, five meshes were chosen to analyse the result convergence, in Software #1, in which both the mesh size and the lumping factor were varied. Table 4.3 shows the mesh properties of this simulation group. The point of analysis was chosen to be node (N), situated in the top of the part, as schematically shown through Figure 4.32.

Table 4.3: Mesh size, lumping factor and total number of elements in part.

Mesh size (mm)	**Lumping Factor**	**Number of elements**
2.5	50	375
1.25	25	3000
0.625	15	20000
0.625	5	60000
0.625	1	300000

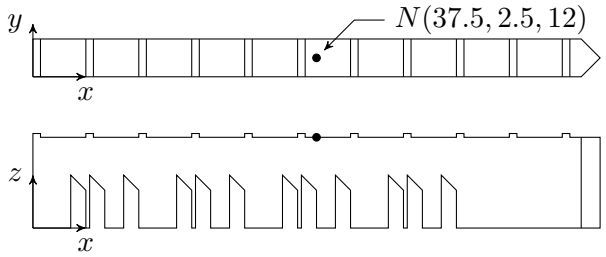

Figure 4.32: Definition of node (N), used to retrieve residual stress values in Software #1.

The longitudinal σ_{xx} and transverse σ_{yy} stress values for node (N) are displayed in Figure 4.33. Both values converged to less than 10% of the result difference correspondent to the finest mesh, with the transverse stresses σ_{yy} having a difference of 8.64% between them. This result is expected, considering the narrow nature of this component - it measures only 5 mm in width - so it benefits considerably from a more refined mesh.

The second objective of this simulation was measuring the effect of the projection factor, a parameter available in Software #2 that allows the creation of skewed elements: it varies from 0 to 1, and the greater its value is, the more closely it will adapt to the part's geometry at the risk of generating non solvable meshes. To evaluate the effect of this parameter in the mesh, three parameters are chosen: the aspect ratio, the Jacobian ratio and element quality.

Aspect ratio Aspect ratios are computationally simple measurements that quantify distortion. For hexahedral elements, such as the ones studied in this simulation group, it is calculated by dividing the longest edge by the shortest [74] (some solvers determine it through the diagonal instead of the edge). Figure 4.34 schematically displays this. For hexahedral elements, the following categories have been established: $1 < AR < 3$ are

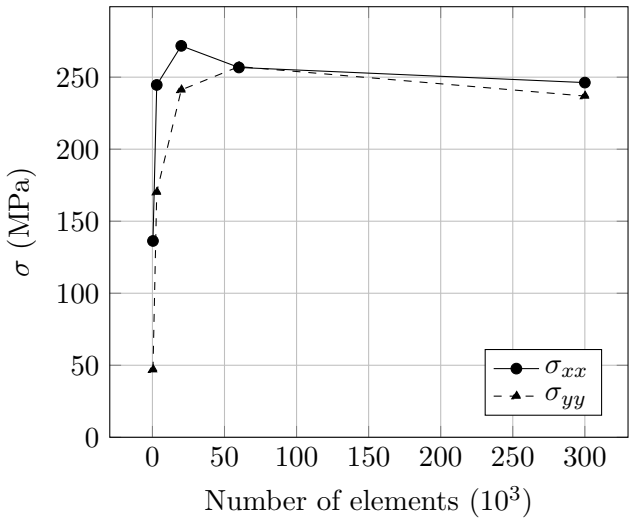

Figure 4.33: Longitudinal and transverse stress convergence curves, in node (N), in Software #1.

considered acceptable, $3 < AR < 10$ are problematic, and $AR > 10$ should be avoided [75].

Additionally, the analysis of the AR should be accompanied by the specific location of the critical elements, and what percentage they make up of the total number of elements: it is recommended that the percentage of elements with aspect ratios greater than three remain under 5% [76]. One should also be wary of their location, for if they are situated distant from the critical areas of interest, their harm is significantly hampered [74].

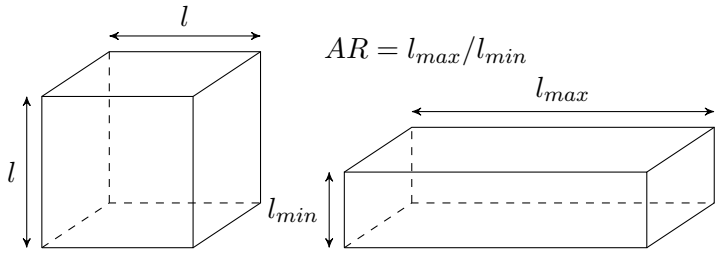

Figure 4.34: Schematic representation of the aspect ratio in hexahedral elements.

Jacobian ratio The Jacobian ratio provides a measure of the distortion undergone by a skewed element, in regards to its ideal shape [74]: mathematically, it is represented by the determinant of the Jacobian matrix. The Jacobian matrix $\boldsymbol{J}$ is present in all FEA computations, as it is responsible for mapping the ideally-shaped element in isoparametric coordinates to the problem's real geometry [77]; the Jacobian ratio of an extremely deformed element is negative and hinders any simulation from taking place [78].

The proposed criteria in literature to evaluate element's Jacobian ratio are: *(i)* it must be necessarily positive; *(ii)* preferably greater than 0.2 in magnitude [79]; *(iii)* less than 5% of elements should display a Jacobian ratio smaller than 0.7 [80].

Element quality The element quality metric provides a composite quality metric that ranges between zero and one [42], in which the unitary value represents a perfect cube and

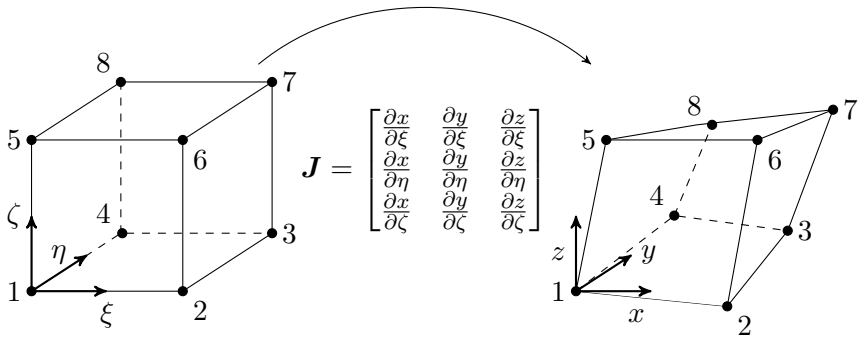

Figure 4.35: Schematic representation of the Jacobian ratio in hexahedral elements (adapted from [74]).

a value of zero indicates zero volume.

Its mathematical definition is given in Equation (4.3):

$$EQ = \gamma \cdot \frac{V}{\sqrt{\left(\sum_i l_i^2\right)^3}} \tag{4.3}$$

in which EQ is the element quality, γ is an element-dependent constant, assuming a value of 4 in hexahedral elements, V is the element's volume, and l_i is an element's side, in which the subscript i corresponds to the side's index.

Element quality, the Jacobian ratio and the aspect ratio's distribution in the three different meshes used in the benchmark bridge's simulations are shown in Figures 4.36, 4.37 and 4.38, respectively. These three images are aimed at showing the potentially problematic areas of the mesh, in the benchmark's geometry as a whole.

As expected, the areas of greater complexity provided increased challenges in the meshing processes, with these being the overhanging area at the top of the bridge legs, as well as the the bevelled extremity at $x = 72.5\,\text{mm}$.

Figures 4.39a-4.39b highlight the bevelled extremity's mesh, and how an increase in the projection factor helps with the description of more complex geometries at the cost of poorer defined elements. Additionally, Figures 4.40a-4.40b show the element quality contour plots for the bridge legs' slanted detail.

It can be seen that the bevelled area benefited considerably more from the increase of the projection factor, while the bridge legs remained awkwardly defined, in which a stair-step pattern is still very much observable, as observable in Figure 4.40b. This can be attributed to the mesh size being too coarse to accurately represent this region: it can be said that the projection factor does not replace a reduction of the mesh size to more accurately represent a workpiece, but should rather be though of as a complementary factor, as long as the appropriate metrics are taken to validate the mesh.

The evaluation of the presented metrics through the percentage of elements that display values that should be closely monitored ($AR \geq 10$ and $J \leq 0.7$) are shown in Table 4.4. It is observable that only in the mesh with the largest projection factor are there elements who display these values, although their prevalence is below the advised value of 5% of the total mesh, meaning that there is no valid reason to discard these meshes and should be considered validated in terms of mesh metrics. Furthermore, node (N) used to obtain values in this Sub-section can be considered distant from both of the potentially problematic areas.

Table 4.4: Percentage of elements that fulfil mesh metric condition, for three different meshes, pertaining to benchmark bridge with differing projection factors, in Software #2

Projection Factor	$J \leq 0.7$	$AR \geq 3$	$AR \geq 10$
0	0%	0%	0%
0.25	0.07%	0%	0%
0.75	2.48%	4.13%	2.86%

The residual stress values obtained in node (N) are shown in Figure 4.41, for different projection factors, within the Software #2 environment. As observable, the difference between the values obtained in Software #2 with different projection factors are not significantly different between them. Both the longitudinal and transverse stress σ_{xx} and σ_{yy}, after the layer's build stage and after cooldown, are similar, with the difference between the result with a projection factor of 0 and 0.75 being 0.84%. This isn't unsurprising due to the same reasons explored in the mesh's quality evaluation: the analysed node (N) is distant from the most problematic meshing areas, and therefore, for the same simulation parameters, results aren't expected to significantly differ.

In Figure 4.41 the comparison between the most refined mesh, with a 0.625 mm mesh, is also established. The longitudinal stress σ_{xx} is slightly larger for the simulations conducted in Software #2, with a difference of 6.65% between a projection factor of 0.0 and Software #1's simulation. Additionally, transverse residual stress σ_{yy} is considerably lower in Software #2, with the simulation with a null projection factor experiencing yielding a value 45.59% inferior in comparison to Software #1: this result behaviour is similar with the results obtained for the unitary layer case, explored in Subsection 4.2.1, where Software #2 provided increased results for the longitudinal stress σ_{xx} and lower values for the transverse stress σ_{yy}, for values obtained in node (D).

Lastly, the longitudinal stress contour plots for the three conducted simulations can be found in Figures 4.42a-4.42c. These figures have been included to display the general decrease in tensile residual stress, in the lateral bridge surface, in the slanted side of the bridge legs. The remaining stress field, however, remains largely the same, which is consistent to the extracted values in node (N).

To better highlight the projection factor's influence on the surrounding residual stress field, Figures 4.43a-4.43c are introduced. In these figures, it is possible to observe how a decrease of the stair-like pattern associated with hexahedral meshes can reduce the surrounding stress field due to the elimination of most sharp corners.

In FEA, sharp corners introduce stress singularities generally due to the derivatives of the primary variable, which in this case is the displacement, becoming unbounded and tending to infinity [26]. Sharp corners usually can be dealt with by applying more robust material formulations or through further treatment in the computational stage [81].

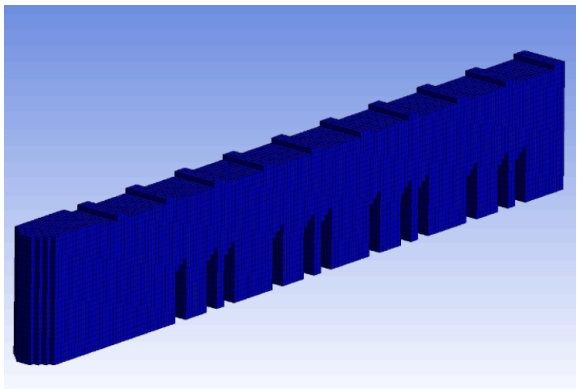

(a) Projection Factor of 0.0

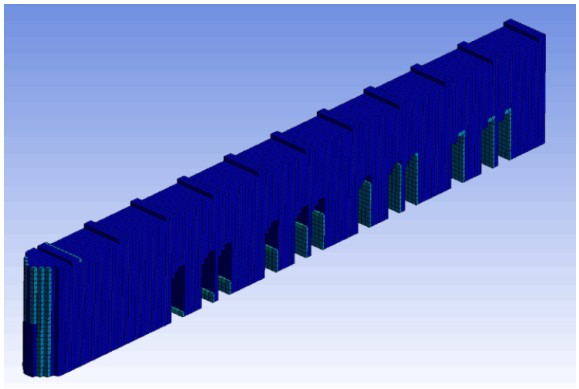

(b) Projection Factor of 0.25

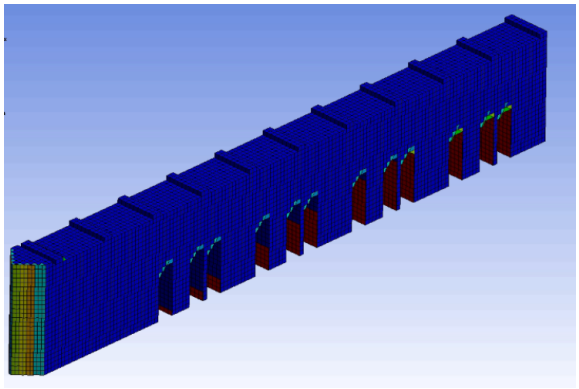

(c) Projection Factor of 0.75

Figure 4.36: Element quality contour plots, for three meshes with different projection factors, as defined in Software #2.

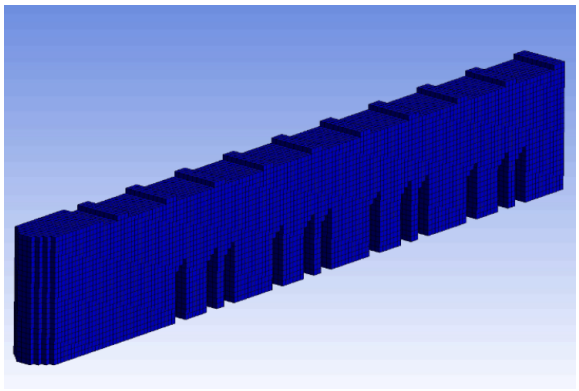

(a) Projection Factor of 0.0

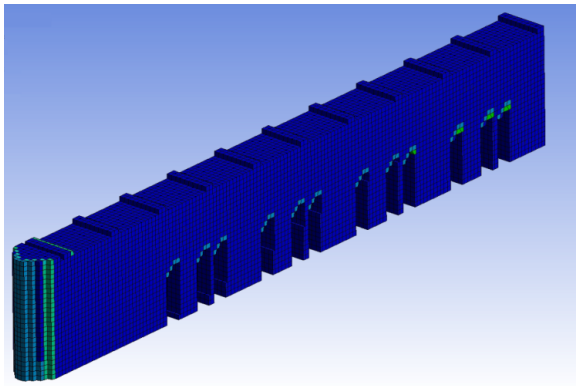

(b) Projection Factor of 0.25

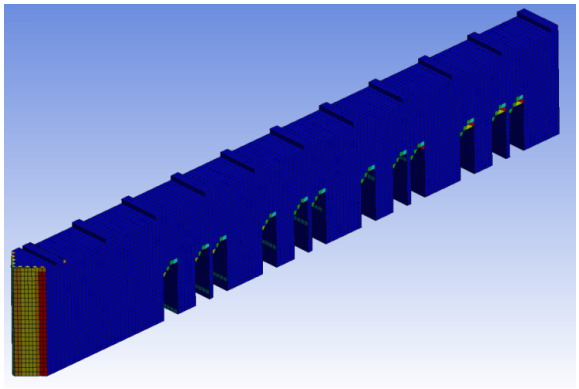

(c) Projection Factor of 0.75

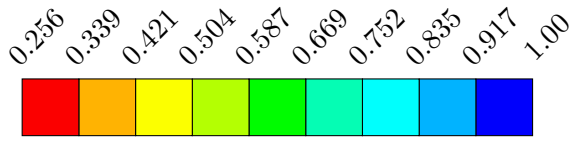

Figure 4.37: Jacobian ratio contour plots, for three meshes with different projection factors, as defined in Software #2.

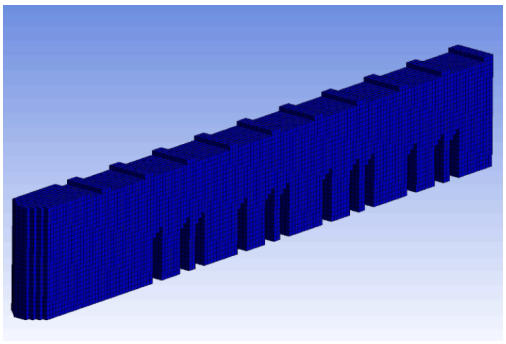

(a) Projection Factor of 0.0

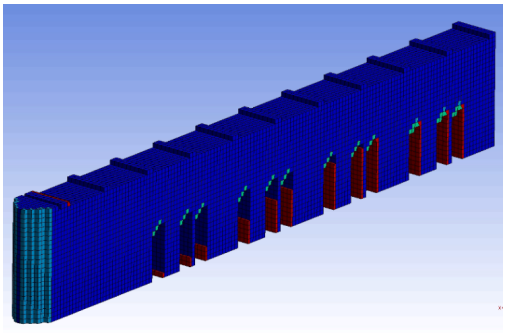

(b) Projection Factor of 0.25

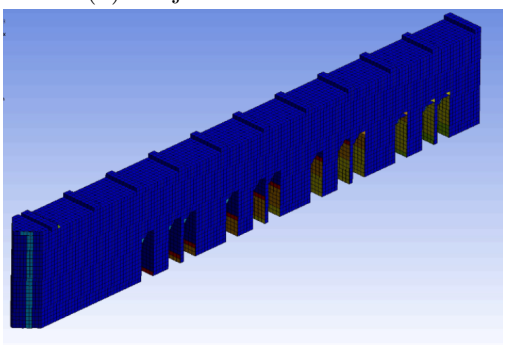

(c) Projection Factor of 0.75

Figure 4.38: Aspect ratio contour plots, for three meshes with different projection factors, as defined in Software #2.

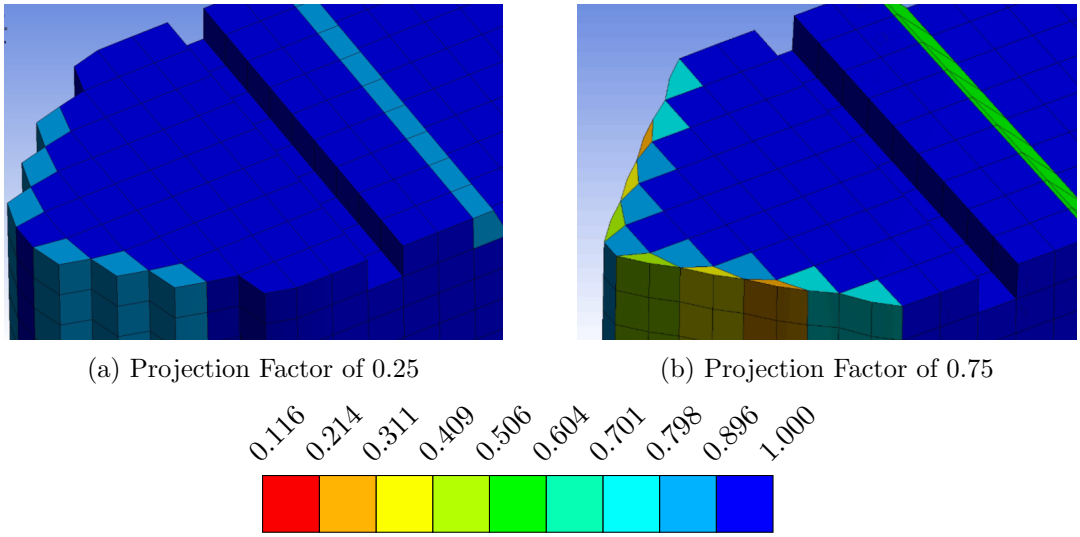

(a) Projection Factor of 0.25 (b) Projection Factor of 0.75

Figure 4.39: Element quality contour plots of bevelled extremity detail, for two different meshes, as defined in Software #2.

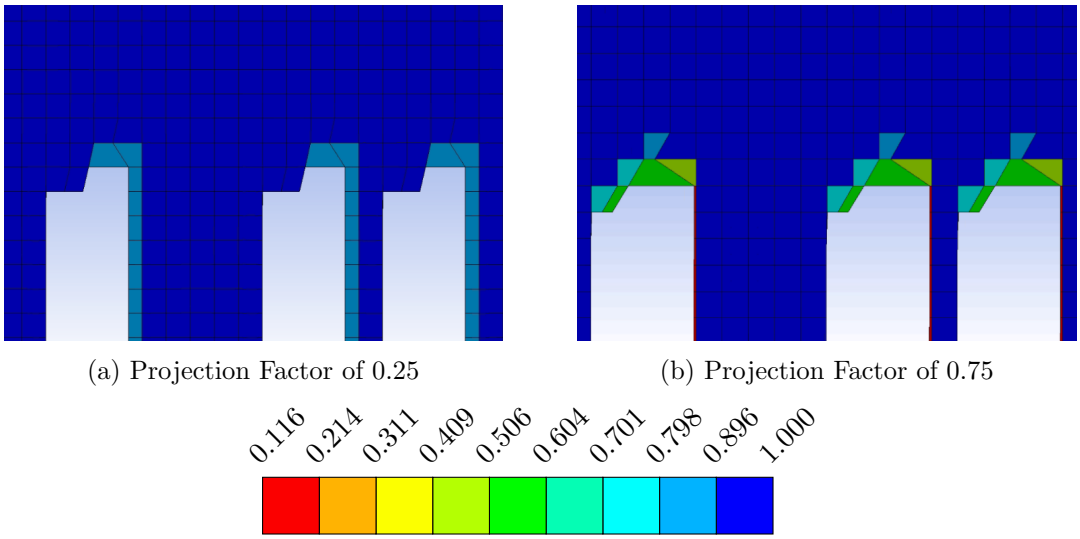

(a) Projection Factor of 0.25 (b) Projection Factor of 0.75

Figure 4.40: Element quality contour plots of bridge legs, for two different meshes, as defined in Software #2.

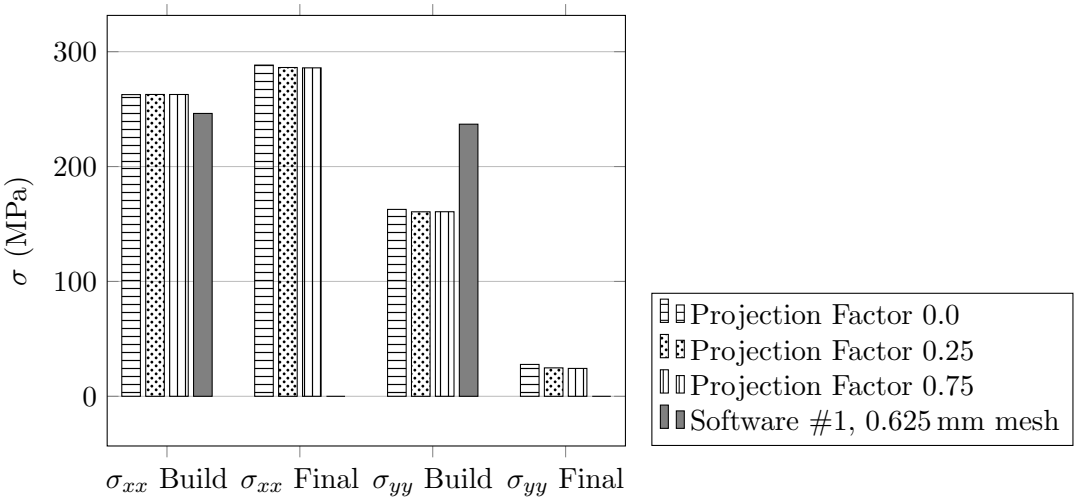

Figure 4.41: Longitudinal and transverse stresses in node (N), for different projection factor meshes, in Software #2

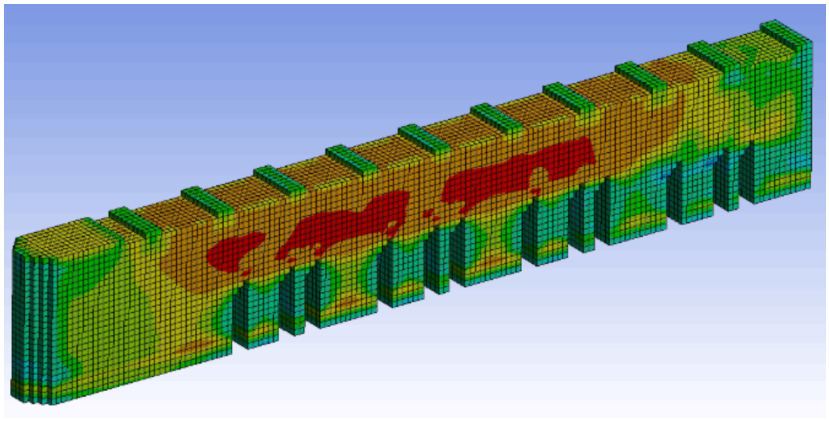

(a) Projection Factor of 0.0

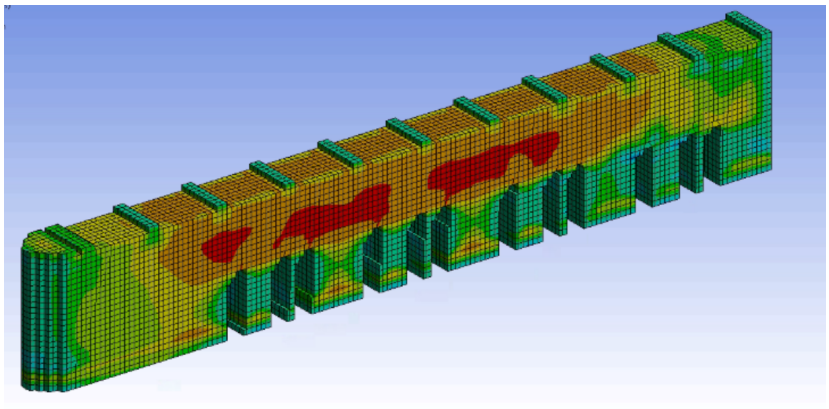

(b) Projection Factor of 0.25

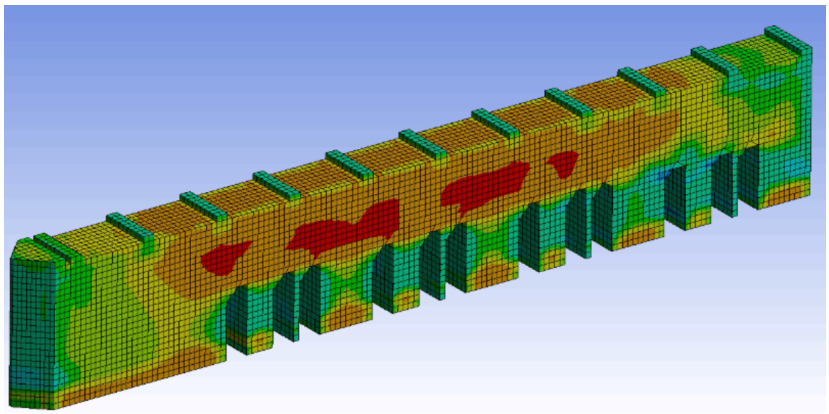

(c) Projection Factor of 0.75

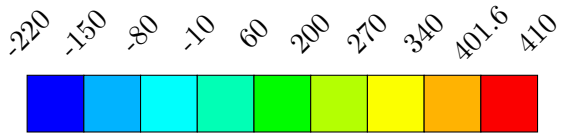

(MPa)

Figure 4.42: Longitudinal stress σ_{xx} contour plots for three different projection factors, as defined in Software #2, for the benchmark bridge's simulation.

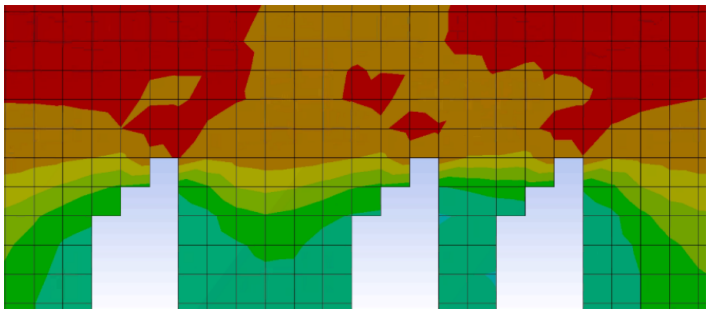

(a) Projection Factor of 0.0

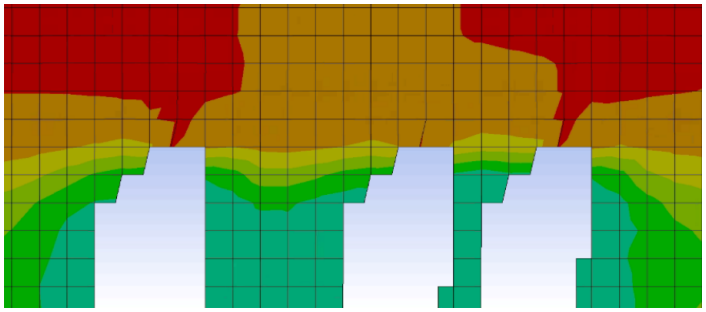

(b) Projection Factor of 0.25

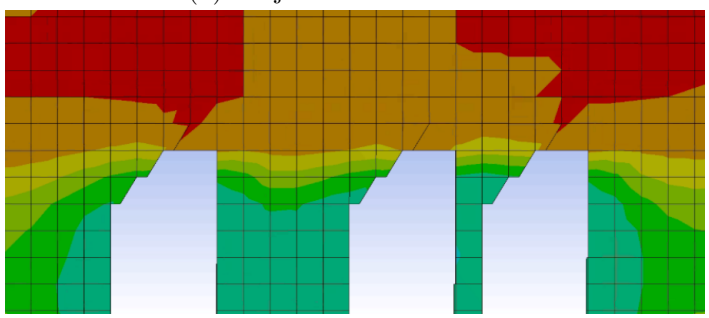

(c) Projection Factor of 0.75

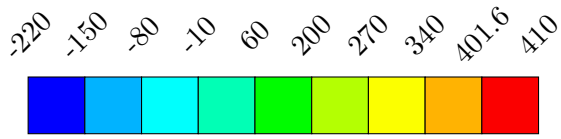

(MPa)

Figure 4.43: Longitudinal stress σ_{xx} contour plots in the slanted legs detail, for three different projection factors, as defined in Software #2, for the benchmark bridge's simulation.

4.3 Part removal

This simulation aimed at exploring the stress state and displacement evolution with the subsequent removal of bridge legs from the baseplate, simulating a manufacturing process such as EDM that would be responsible for the physical separation between the workpiece and the baseplate. This separation leads to a reduction in the magnitude of the residual stresses, as the connection between the rigid base and the remaining part is severed, leading to a greater part distortion. Hence, in this analysis, both the residual stress in the longitudinal direction σ_{xx} and the component displacement in the vertical direction u_{zz} is studied, for points (P) and (Q), as defined in Figure 4.44.

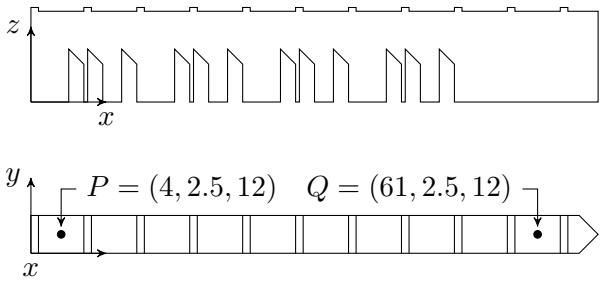

Figure 4.44: Points used to track nodal variables during the removal stage of the benchmark bridge's legs, in Software #1.

As expected, the residual stress in point (Q) immediately decreased by 31.8% once its respective supporting leg is removed. However, with the continuous leg detachment, no remarkable stress variations occur in point (Q) other than a decimal increment that can be attributed to the component's increasing bending. Additionally, the displacement that occurs in point (Q) is incremental with the number of bridge legs removed in an approximately linear fashion. Figures 4.46a-4.46d visually display the displacement evolution throughout the process.

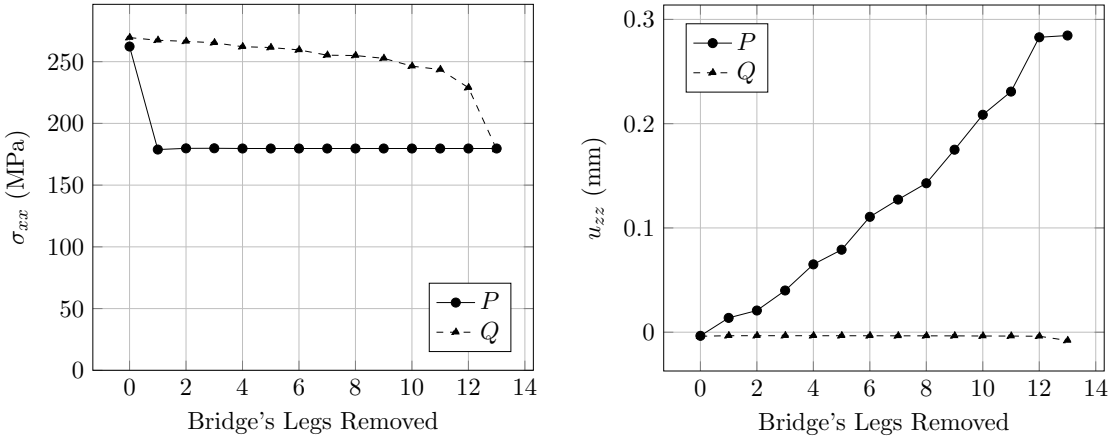

(a) Longitudinal stress evolution

(b) Vertical displacement evolution

Figure 4.45: Stress and displacement evolution with number of removed legs.

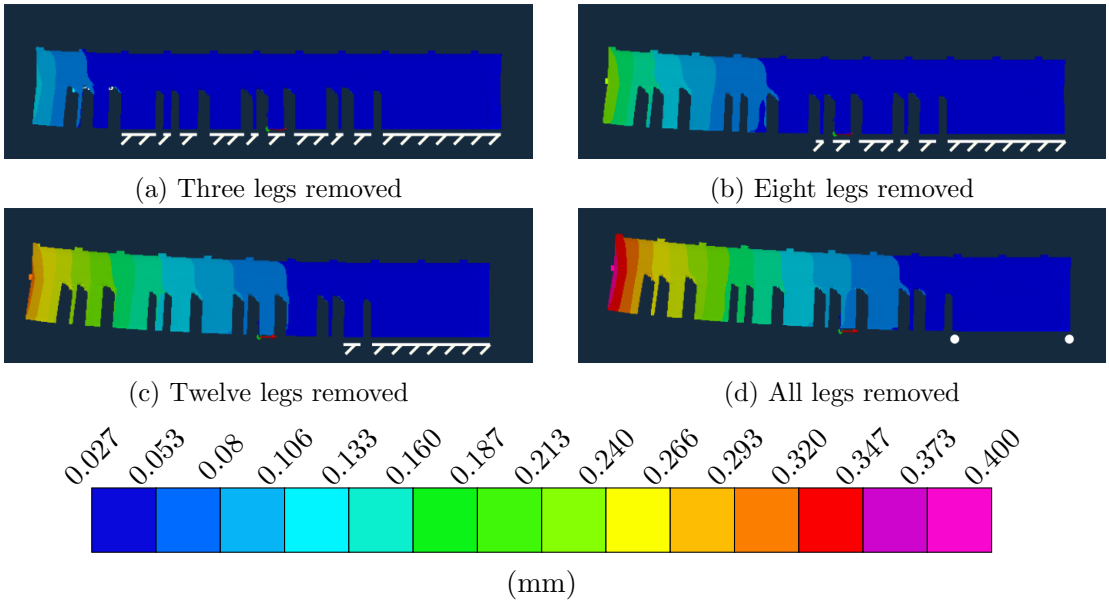

(a) Three legs removed

(b) Eight legs removed

(c) Twelve legs removed

(d) All legs removed

Figure 4.46: Displacement u_{zz} evolution with number of removed legs.

4.4 Comparison between numerical and experimental results

This Section of the research work is dedicated to exploring the numerical studies whose objective was simulating the manufacturing process of a physical sample as close as possible. Initially, both software packages were used to simulate this process; however, due to an unexpected temporary problem regarding INEGI's internal network rendered Software #1 inaccessible. As certain results could not be obtained, only Software #2 will be used in this Section.

The chosen specimen to simulate was the benchmark bridge, as its manufacturing process is very well documented, as well as several experimental results, through a series of thorough articles. Among these articles stands one by Phan et al. (2017), who explored the manufacturing process, distortions and residual strains of the benchmark bridge [56]

proposed by NIST, whose results and conclusions will be juxtaposed to the results of the conducted simulations.

Differing experimental analysis were conducted by Phan et al. (2017) through neutron and X-Ray diffraction, as well as contour and coordinate measurement system methods, with these being the residual strain field in the $y = 2.5\,\text{mm}$ plane, the residual strain of three section cuts after sectioning through WEDM and coordinate measurement after bridge's leg removal. In this research work, the former and the latter will be analysed and experimental values compared to performed simulations.

4.4.1 Residual strain field

Three simulations were conducted in Software #2, whose parameters were chosen to accurately simulate the NIST benchmark bridges' manufacturing process. Within these simulations, only one parameters differed, which was the projection factor: the chosen values for this property were 0.0, 0.25 and 0.75.

The results of the experimentally obtained residual strain fields are visually shown in juxtaposition to the ones obtained in Software # 2 through Figures 4.47-4.50. The use of the same colour scheme in the presented contour plots was employed to allow for easier and better comparison between residual strains; the black coloured areas are representative of values obtained in the FEA that are beyond the scale employed in the experimental analysis conducted by Phan et al. (2017) [56]. Figures 4.51-4.54 are shown to display the full range of residual strains.

As observable in Figures 4.48a-4.48d, the vertical strain ε_{zz} is mostly compressive in nature, with the exception of the sample's extremities, which in turn exhibit large tensile strains. Alternatively, the longitudinal strain ε_{xx} is compressive near the legs, but overwhelmingly tensile near the top of the sample, with the maximum experimental value nearing $2 \times 10^{-3}\,\text{mm}\,\text{mm}^{-1}$. Both of these observations are coherent with the expected residual strain and stress development in parts manufactured by LPBF.

The comparison between the simulated and the experimental component's residual strains shows that both compressive and tensile areas are generally well represented and do match in geometry: this means that the portions of the section area that were experimentally shown to be tensile were also tensile in the performed simulations. The outliers to this assertion would be a slight compression near the right-handed extremity of the experimentally obtained longitudinal strain ε_{xx} - shown in Figure 4.47d - that in the other hand is mostly tensile in the simulated cases - shown in Figures 4.47a-4.47c. The other problematic case, at first glance, would be the same area, but in the skewed residual strain ε_{45}, in which the experimental case appears to be largely in compression; however, Phan et al. (2017) explains that this measurement's statistical analysis failed to refine the data, as observable by the cloud-like effect in Figure 4.50d: this could explain how this area's strain distribution is mostly tensile in the FEA case.

In general, the values obtained by the finite element method displayed greater amplitudes, meaning that positive strains were larger and negative strains were smaller. This may be explained by the hindered ability of already deposited layers of being subjected to reheating cycles.

Furthermore, an additional reason for larger residual strains in the numerical case may be an overestimation of the contact stiffness between the baseplate and the component.

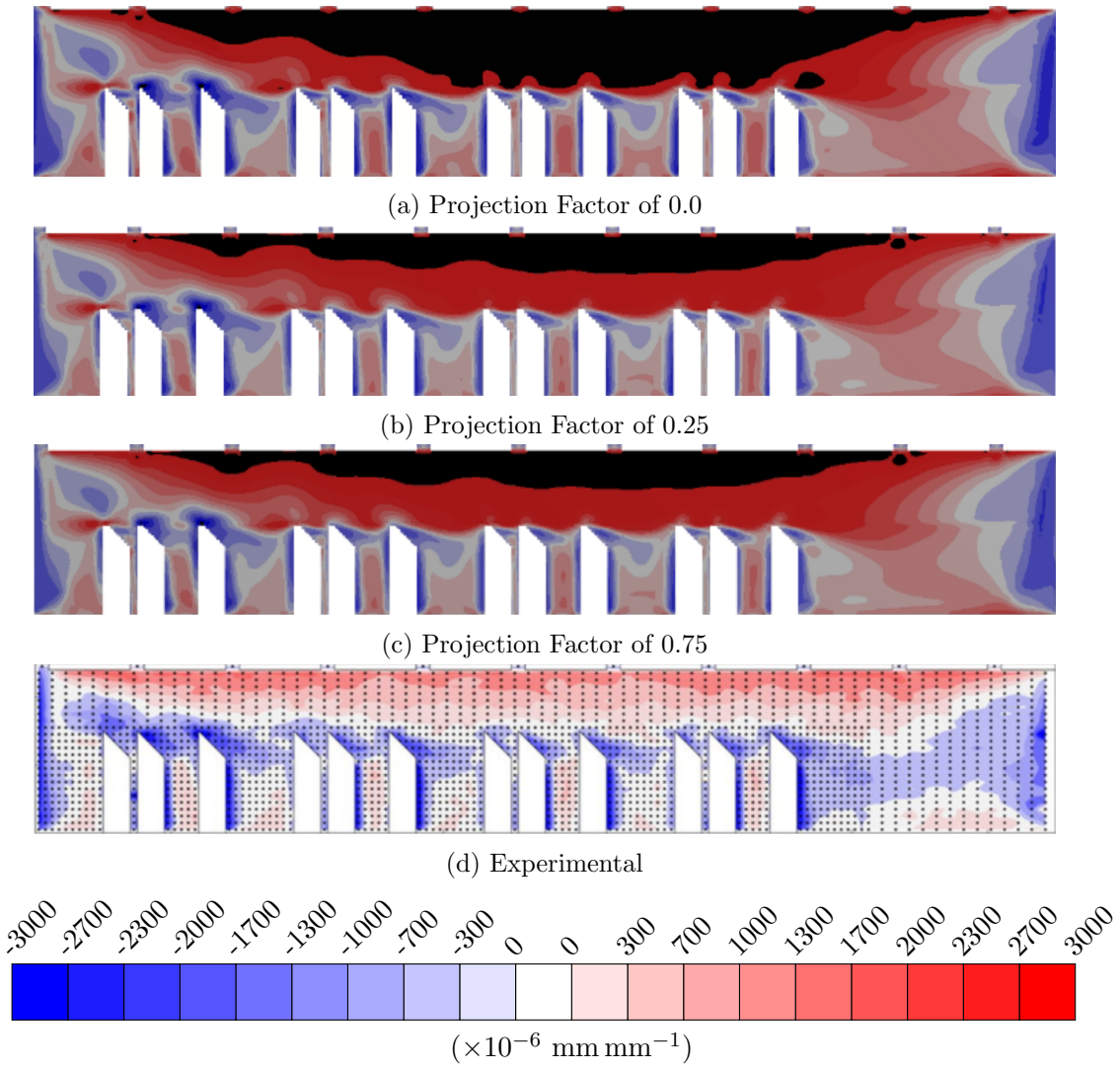

(a) Projection Factor of 0.0

(b) Projection Factor of 0.25

(c) Projection Factor of 0.75

(d) Experimental

Figure 4.47: Experimental and numerical comparison between longitudinal residual strain ε_{xx} contour plots, extracted from $y = 2.5\,\text{mm}$ plane in Iconel 625 benchmark bridges.

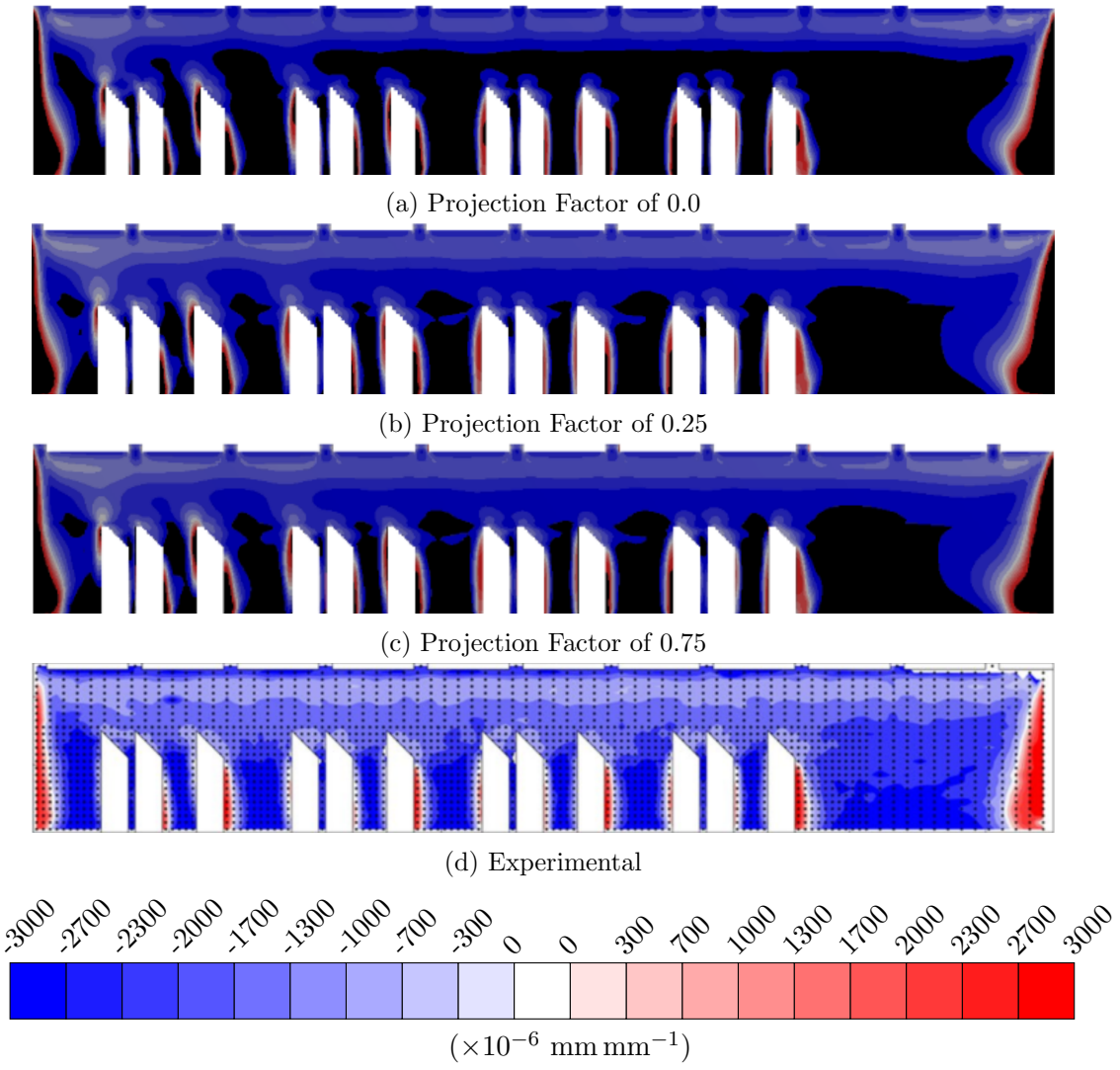

(a) Projection Factor of 0.0

(b) Projection Factor of 0.25

(c) Projection Factor of 0.75

(d) Experimental

Figure 4.48: Experimental and numerical comparison between vertical residual strain ε_{zz} contour plots, extracted from $y = 2.5\,\text{mm}$ plane in Iconel 625 benchmark bridges.

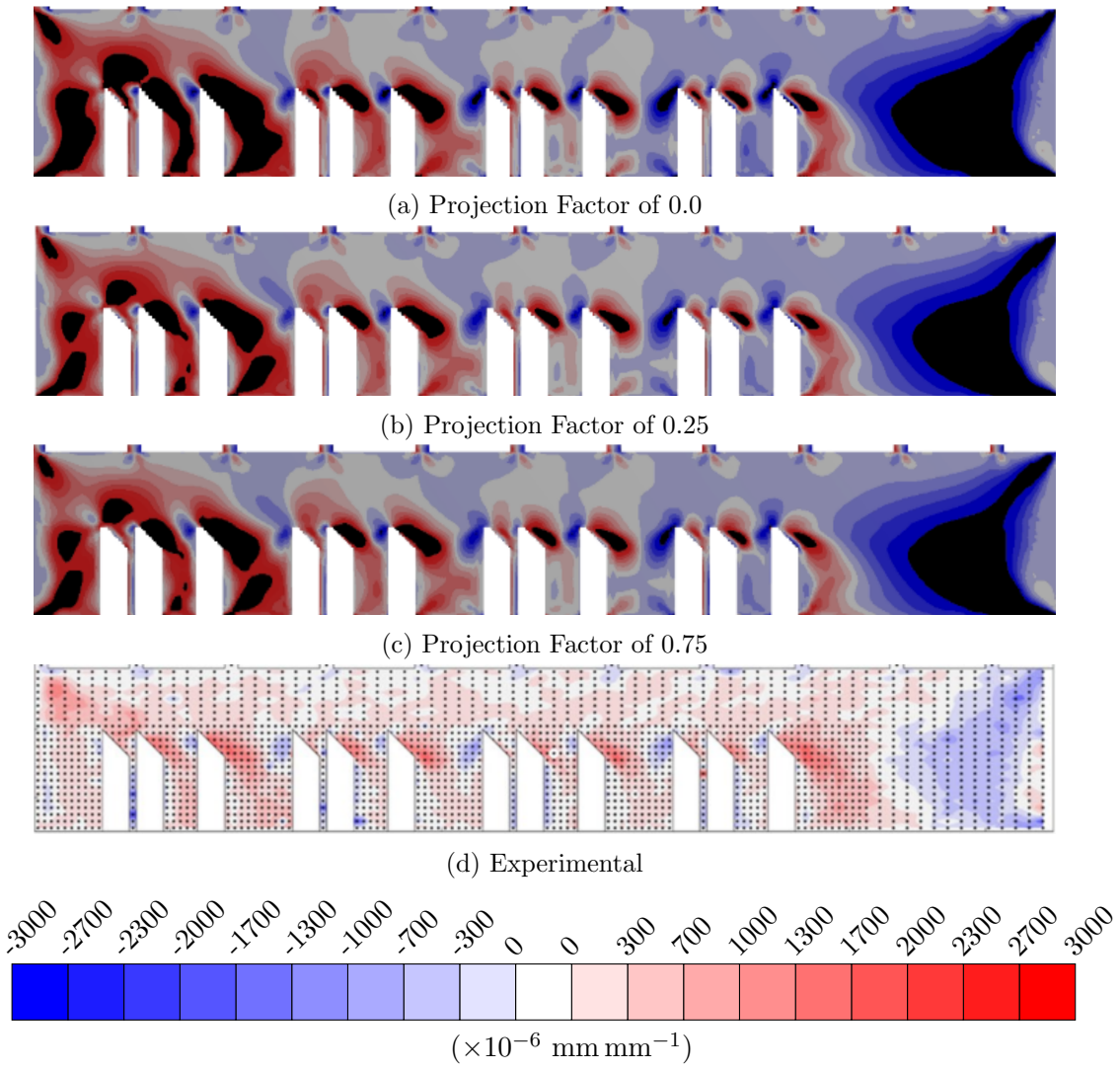

(a) Projection Factor of 0.0

(b) Projection Factor of 0.25

(c) Projection Factor of 0.75

(d) Experimental

Figure 4.49: Experimental and numerical comparison between vertical residual strain ε_{xz} contour plots, extracted from $y = 2.5\,\text{mm}$ plane in Iconel 625 benchmark bridges.

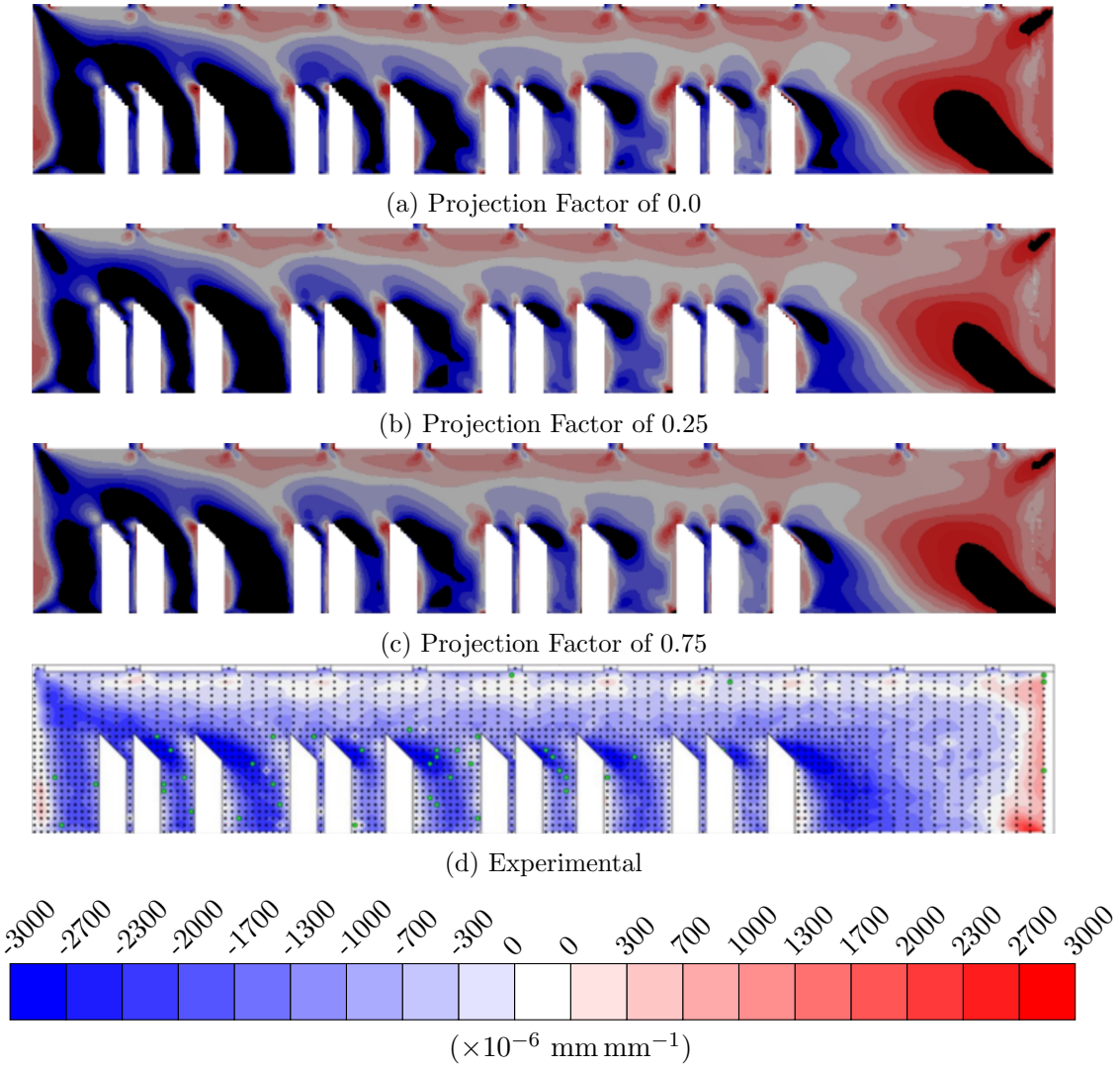

(a) Projection Factor of 0.0

(b) Projection Factor of 0.25

(c) Projection Factor of 0.75

(d) Experimental

Figure 4.50: Experimental and numerical and numerical comparison between skewed residual strain ε_{45} contour plots, extracted from $y = 2.5\,\text{mm}$ plane in Iconel 625 benchmark bridges.

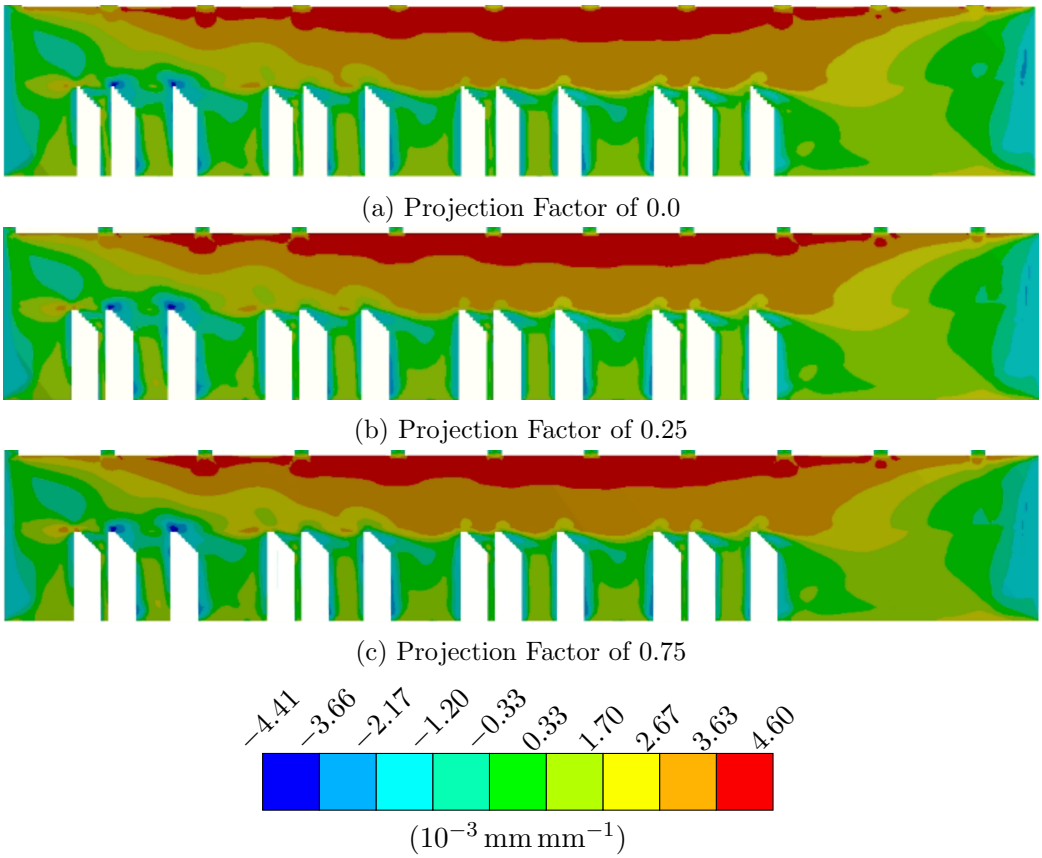

(a) Projection Factor of 0.0

(b) Projection Factor of 0.25

(c) Projection Factor of 0.75

Figure 4.51: Longitudinal elastic strain ε_{xx} contour plots, extracted from $y = 2.5\,\text{mm}$ plane in Iconel 625 benchmark bridges.

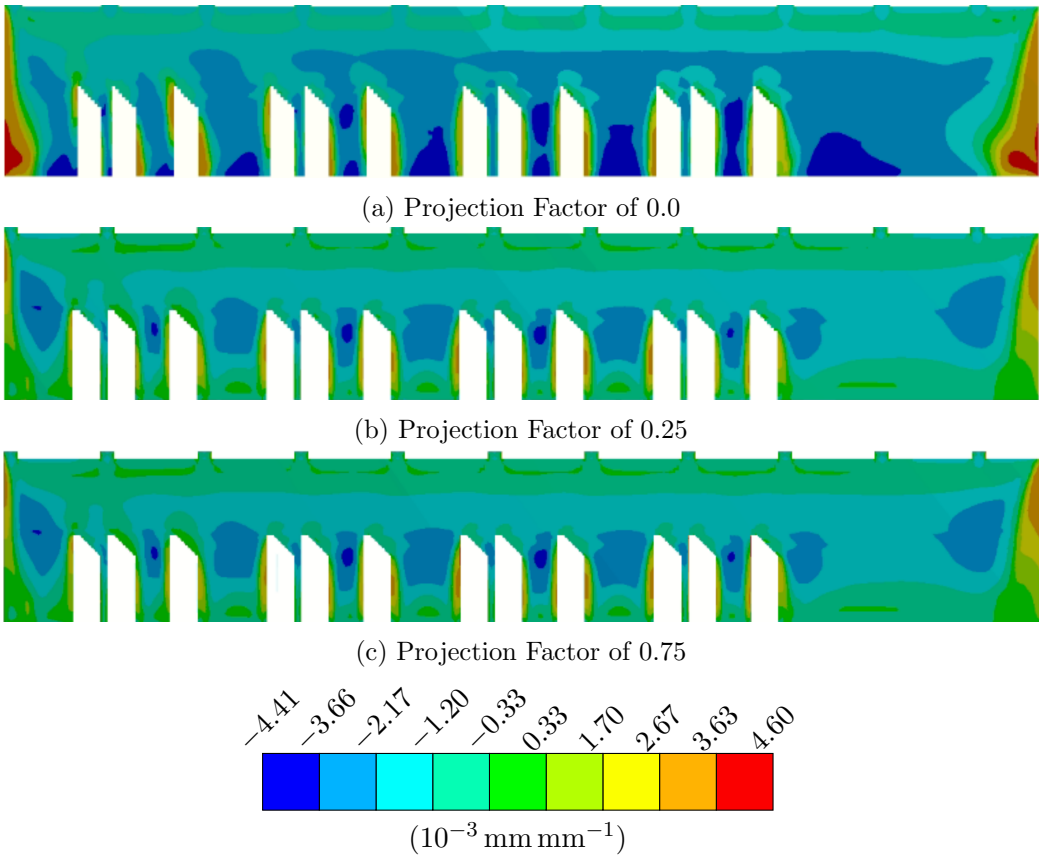

(a) Projection Factor of 0.0

(b) Projection Factor of 0.25

(c) Projection Factor of 0.75

Figure 4.52: vertical residual strain ε_{zz} contour plots, extracted from $y = 2.5\,\text{mm}$ plane in Iconel 625 benchmark bridges.

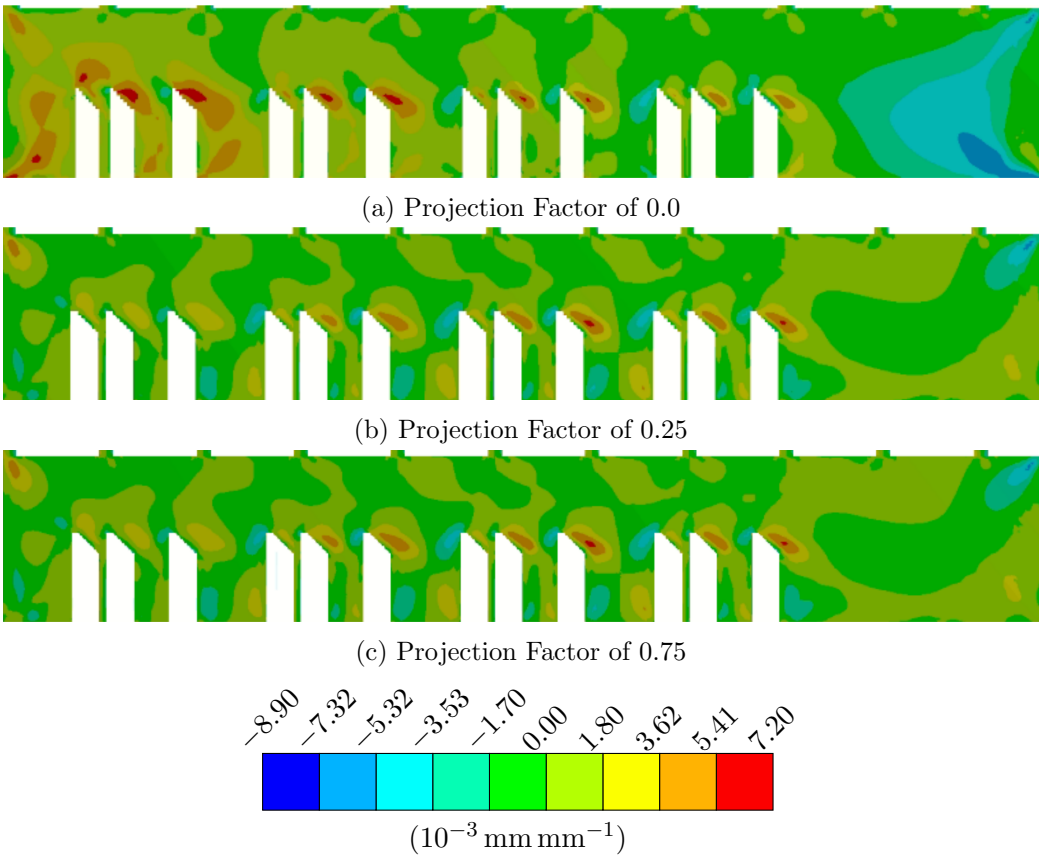

(a) Projection Factor of 0.0

(b) Projection Factor of 0.25

(c) Projection Factor of 0.75

Figure 4.53: vertical residual strain ε_{xz} contour plots, extracted from $y = 2.5\,\text{mm}$ plane in Iconel 625 benchmark bridges.

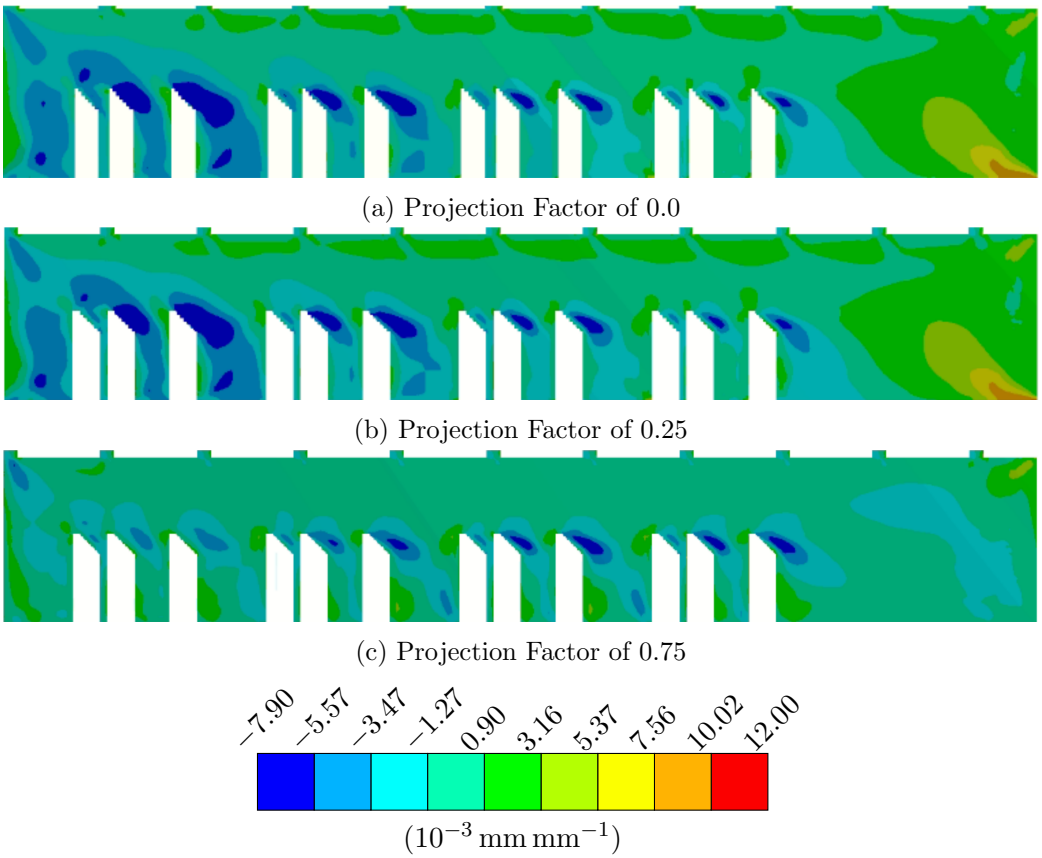

(a) Projection Factor of 0.0

(b) Projection Factor of 0.25

(c) Projection Factor of 0.75

Figure 4.54: Skewed residual strain ε_{45} contour plots, extracted from $y = 2.5\,\text{mm}$ plane in Iconel 625 benchmark bridges.

4.4.2 Deflection analysis

This portion of the performed analysis studies the component's deflection after all of its legs have been removed through EDM, meaning that the part remains attached to the baseplate solely through its larger section near the right-hand extremity.

The experimental results obtained through Coordinate Measuring Machine (CMM) after the component was subjected to post-processing to assure a smooth surface at its top, providing more accurate results. The associated error to this procedure is 5 µm [56].

Both the experimental and numerical results can be found in Figure 4.55, in which the numerical result was chosen to be exclusively the one with a projection factor of 0.75, due to the almost identical results obtained in the three simulations (the displacements only varied 0.015% with each other for different projection factors). The numerical results were shown to be smaller, with the simulated value at $x = 0$mm displaying a 22.2% difference.

Figure 4.55 shows where this difference may arise from: due to the final boundary conditions of the problem, in which three nodes of the mesh remain constrained to avoid rigid body movement, the volume near the right extremity contracts and bends downwards. This contraction causes a negative displacement in the nodes in the right hand side of the component, and worsens the results obtained via FEA.

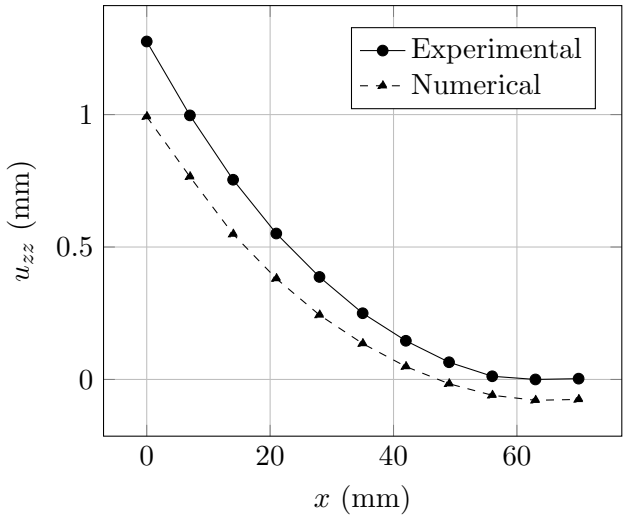

Figure 4.55: Experimental and numerical comparison between vertical deflection u_{zz} after leg removal.

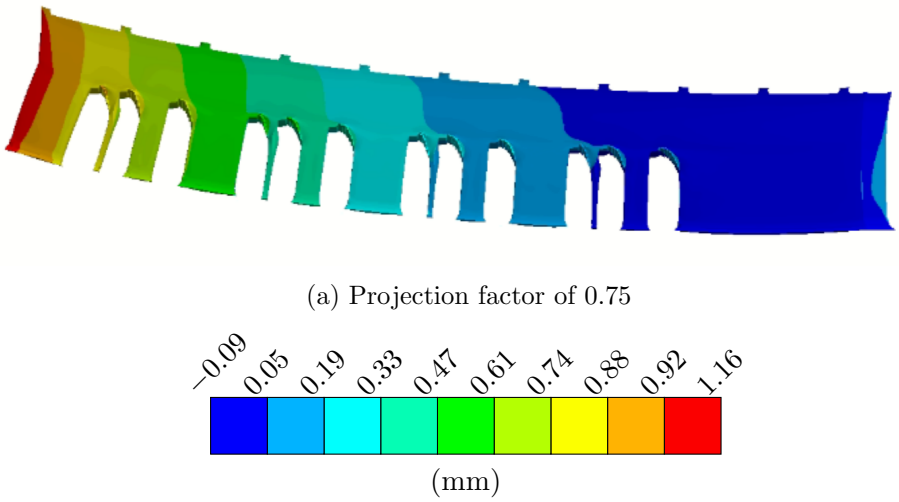

(a) Projection factor of 0.75

Figure 4.56: Displacement u_{zz} contour plot with geometrical scale of 6.6.

Chapter 5

Conclusions and Future Work

5.1 Conclusions

The main goal of this dissertation was to provide an insight into the existing commercial finite element software packages aimed at computing distortion and residual stresses. The goal was successfully achieved by exploring the FEA formulation of the AM process, conducting parametric and convergence studies on its input variables and, finally, establishing comparisons with experimental values found in literature.

The main conclusions that were reached are presented below:

- Software #1 solves the thermomechanical problem by establishing a layer's initial temperature to the melting temperature, and subsequently cooling it down to the chamber temperature; Software #2 solves a weakly-coupled thermomechanical analysis;
- In a simple geometry such as the prism, Software #1 converged on the measured residual stress values, as the mesh was refined. Out of both parameters that account for mesh size, the lumping factor proved to be the most significant, by allowing result convergence faster than increasing the number of elements per numerical layer;
- The decrease in the baseplate's stiffness greatly affects the prism's longitudinal residual stress, showing little influence on transverse stress. A thinner baseplate is less capable of constraining the component's deformations, leading to lower stress magnitudes.
- The large strain hypothesis' influence on results decreases with an increase in plate stiffness;
- Software #2's laser speed and hatch space contribute to the calculation of the deposition time step, with an increase in either parameter resulting in the decrease of residual stress in both transverse and longitudinal stresses, as the temperatures remain higher with less time to cool down;
- The one layered simulation proved to be successful, allowing the definition of a similar residual stress distribution using the same mesh size and material, providing similar values as expected;
- The prism's residual stress configuration, for the same mesh size and simulation parameters, gave non-optimal results that improved once the accurate time step pertaining to Software #2 was studied;

- The component removal simulation showed an almost linear variation between the number of bridge legs removed and the vertical displacement;
- The projection factor parameter in Software #2 showed to be capable of more accurately modelling a geometry's mesh, although it is not to replace the effectiveness of a finer mesh, which remains the most suitable way of representing a component more truthfully;
- Similar residual strain fields to the experimental NIST bridges were achieved in Software #2, although displaying larger strain ranges;
- The NIST's benchmark bridge deflection after leg removal was simulated in Software # 2 with an error of 22.2% owing to the boundary conditions of the final step.

5.2 Future Work

To build on the work developed in this thesis, some suggestions are provided:

- Simulations in additional software packages for distortion and residual stress prediction, to further compare different numerical models;
- Explore the inherent strain model and compare the residual stress field with the obtained values, juxtaposed to computation times;
- Analyse the influence of heat treatments in the AM simulation process;
- Experimental study of the prism and INEGI's benchmark bridges, and comparison to numerical values.

References

[1] Yi Zhang, Linmin Wu, Xingye Guo, Stephen Kane, Yifan Deng, Yeon-gil Jung, Jehyun Lee, and Jing Zhang. Additive Manufacturing of Metallic Materials : A Review. *Journal of Materials Engineering and Performance*, 27(1):1–13, 2018.

[2] Ian Gibson, David Rosen, and Brent Stucker. *Additive Manufacturing Technologies – Rapid Prototyping to Direct Digital Manufacturing*, volume 5. Springer, 01 2010.

[3] Yunkang Sui and Xirong Peng. *Modeling, Solving and Application for Topology Optimization of Continuum Structures: ICM Method Based on Step Function*. Butterworth-Heinemann, 2017.

[4] Li Yang, Keng Hsu, Brian Baughman, Donald Godfrey, Francisco Medina, Mamballykalathil Menon, and Soeren Wiener. *Additive Manufacturing of Metals: The Technology, Materials, Design and Production*. Springer, 01 2017.

[5] Adrian P. Mouritz. 11 - steels for aircraft structures. In Adrian P. Mouritz, editor, *Introduction to Aerospace Materials*, pages 232 – 250. Woodhead Publishing, 2012.

[6] Yu Sun, Rainer J. Hebert, and Mark Aindow. Effect of laser scan length on the microstructure of additively manufactured 17-4ph stainless steel thin-walled parts. *Additive Manufacturing*, 35:101302, 2020.

[7] Usman Ali, Haniyeh Fayazfar, Farid Ahmed, and Ehsan Toyserkani. Internal surface roughness enhancement of parts made by laser powder-bed fusion additive manufacturing. *Vacuum*, 177:109314, 2020.

[8] Ruishan Xie, Gaoqiang Chen, Yue Zhao, Shuai Zhang, Wentao Yan, and Xin Lin. In-situ observation and numerical simulation on the transient strain and distortion prediction during additive manufacturing. *Journal of Manufacturing Processes*, 38(February):494–501, 2019.

[9] H-W Mindt, O Desmaison, M Megahed, A Peralta, and J Neumann. Modeling of powder bed manufacturing defects. *Journal of Materials Engineering and Performance*, 27(1):32–43, 2018.

[10] C. Li, Z.Y. Liu, X.Y. Fang, and Y.B. Guo. Residual stress in metal additive manufacturing. *Procedia CIRP*, 71:348 – 353, 2018. 4th CIRP Conference on Surface Integrity (CSI 2018).

[11] Ze-Chen Fang, Zhi-Lin Wu, Chen-Guang Huang, and Chen-Wu Wu. Review on residual stress in selective laser melting additive manufacturing of alloy parts. *Optics & Laser Technology*, 129:106283, 2020.

[12] Jamison L. Bartlett and Xiaodong Li. An overview of residual stresses in metal powder bed fusion. *Additive Manufacturing*, 27:131 – 149, 2019.

[13] William E Frazier. Metal Additive Manufacturing : A Review. *Journal of Materials Engineering and Performance*, 23(June):1917–1928, 2014.

[14] Specification for additive manufacturing file format (amf) version 1.2, 2016.

[15] Ruiliang Feng, Xianda Li, Lin Zhu, Atul Thakur, and Xiangzhi Wei. An improved two-level support structure for extrusion-based additive manufacturing. *Robotics and Computer-Integrated Manufacturing*, 67:101972, 2020.

[16] Ratnadeep Paul and Sam Anand. Optimization of layered manufacturing process for reducing form errors with minimal support structures. *Journal of Manufacturing Systems*, 36:231 – 243, 2015. Ben Ezair, Fady Massarwi, and Gershon Elber. Orientation analysis of 3d objects toward minimal support volume in 3d-printing. *Computers & Graphics*, 51:117 – 124, 2015. International Conference Shape Modeling International.

[17] Ruizhen Hu, Honghua Li, Hao Zhang, and Daniel Cohen-Or. Approximate pyramidal shape decomposition. *ACM Trans. Graph.*, 33(6):213–1, 2014. Xuelin Chen, Hao Zhang, Jinjie Lin, Ruizhen Hu, Lin Lu, Qi-Xing Huang, Bedrich Benes, Daniel Cohen-Or, and Baoquan Chen. Dapper: decompose-and-pack for 3d printing. *ACM Trans. Graph.*, 34(6):213–1, 2015.

[18] Yassine Saadlaoui, Jean-Louis Milan, Jean-Marie Rossi, and Patrick Chabrand. Topology optimization and additive manufacturing: Comparison of conception methods using industrial codes. *Journal of Manufacturing Systems*, 43:178 – 186, 2017.

[19] Prashanth Konda Gokuldoss, Sri Kolla, and Jürgen Eckert. Additive Manufacturing Processes : Selective Laser Melting , Electron Beam Melting and Binder. *Materials*, 2017.

[20] Federico Mazzucato, Simona Tusacciu, Manuel Lai, Sara Biamino, Mariangela Lombardi, and Anna Valente. Monitoring approach to evaluate the performances of a new deposition nozzle solution for ded systems. *Technologies*, 5(2):29, 2017.

[21] Shahir M. Yusuf and Nong Gao. Influence of energy density on metallurgy and properties in metal additive manufacturing. *Materials Science and Technology*, 33(11):1269–1289, 2017.

[22] S.L. Sing, C.F. Tey, J.H.K. Tan, S. Huang, and Wai Yee Yeong. 2 - 3d printing of metals in rapid prototyping of biomaterials: Techniques in additive manufacturing. In Roger Narayan, editor, *Rapid Prototyping of Biomaterials (Second Edition)*, Woodhead Publishing Series in Biomaterials, pages 17 – 40. Woodhead Publishing, second edition edition, 2020.

[23] Tarasankar DebRoy, HL Wei, JS Zuback, T Mukherjee, JW Elmer, JO Milewski, Allison Michelle Beese, A Wilson-Heid, A De, and W Zhang. Additive manufacturing of metallic components–process, structure and properties. *Progress in Materials Science*, 92:112–224, 2018.

[24] Peter Mercelis and Jean-Pierre Kruth. Residual stresses in selective laser sintering and selective laser melting. *Rapid prototyping journal*, 2006.

[25] Sindo Kou. Welding metallurgy. *New Jersey, USA*, pages 431–446, 2003.

[26] Eugenio Oñate. *Structural Analysis with the Finite Element Method. Linear Statics. Vol. 1: Basis and Solids.* Springer, 1 edition, 01 2009.

[27] O.C. Zienkiewicz, R.L. Taylor, and J.Z. Zhu. 1 - the standard discrete system and origins of the finite element method. In O.C. Zienkiewicz, R.L. Taylor, and J.Z. Zhu, editors, *The Finite Element Method Set (Sixth Edition)*, pages 1 – 18. Butterworth-Heinemann, Oxford, sixth edition edition, 2005.

[28] Mathworks. Finite Element Method Basics, 2020.

[29] D. N. Arnold and A. Logg. Periodic table of the finite elements. *SIAM News*, 47(9), 2014.

[30] Sahil Garg and Mohit Pant. Meshfree methods: A comprehensive review of applications. *International Journal of Computational Methods*, 15(04):1830001, 2018.

[31] Eugenio Oñate. *Structural Analysis with the Finite Element Method. Linear Statics. Vol 2. Beams, Plates and Shells.* Springer, 1 edition, 01 2013.

[32] Y P Yang M Jamshidinia and P Boulware S M Kelly. Prediction of microstructure , residual stress , and deformation in laser powder bed fusion process. *Computational Mechanics*, 61(5):599–615, 2018.

[33] S M Kelly and S L Kampe. Microstructural Evolution in Laser-Deposited Multilayer Ti-6Al-4V Builds : Part I . Microstructural Characterization. *Metallurgical and Materials Transactions A volume*, 35(June):1861–1867, 2004.

[34] Jacob Smith, Wei Xiong, Jian Cao, and Wing Kam. Thermodynamically consistent microstructure prediction of additively manufactured materials. *Computational Mechanics*, 57(3):359–370, 2016.

[35] Jun Cao, Michael A. Gharghouri, and Philip Nash. Finite-element analysis and experimental validation of thermal residual stress and distortion in electron beam additive manufactured ti-6al-4v build plates. *Journal of Materials Processing Technology*, 237:409 – 419, 2016.

[36] T. Mukherjee, V. Manvatkar, A. De, and T. DebRoy. Mitigation of thermal distortion during additive manufacturing. *Scripta Materialia*, 127:79 – 83, 2017.

[37] Yukio Ueda, You Chul Kim, and Min Gang Yuan. A predicting method of welding residual stress using source of residual stress (report i): characteristics of inherent strain (source of residual stress)(mechanics, strength & structural design). *Transactions of JWRI*, 18(1):135–141, 1989.

[38] Nils Keller and Vasily Ploshikhin. New method for fast predictions of residual stress and distortion of am parts. *Student Support: 2014 Annual International Solid Freeform Fabrication Symposium*, 25, 2014.

[39] Farshid Hajializadeh and Ayhan Ince. Short review on modeling approaches for metal additive manufacturing process. *Material Design & Processing Communications*, 2(2):56, 2020.

[40] Matteo Bugatti and Quirico Semeraro. Limitations of the inherent strain method in simulating powder bed fusion processes. *Additive Manufacturing*, 23:329–346, 2018.

[41] Thomas Mayer, Gabriel Brändle, Andreas Schönenberger, and Robert Eberlein. Simulation and validation of residual deformations in additive manufacturing of metal parts. *Heliyon*, 6(5):6, 2020.

[42] Ansys. Additive calibration guide, 2020.

[43] Qingcheng Yang, Pu Zhang, Lin Cheng, Zheng Min, Minking Chyu, and Albert C To. Finite element modeling and validation of thermomechanical behavior of ti-6al-4v in directed energy deposition additive manufacturing. *Additive Manufacturing*, 12:169–177, 2016.

[44] Michael Gouge, Pan Michaleris, Erik Denlinger, and Jeff Irwin. The finite element method for the thermo-mechanical modeling of additive manufacturing processes. In *Thermo-Mechanical Modeling of Additive Manufacturing*, pages 19–38. Elsevier, 2018.

[45] NIST. Amb2018-01 description, 2018.

[46] W.D. Callister and W.D.C. William D. *Materials Science and Engineering: An Introduction, 7th Edition Wiley Plus Set*. John Wiley & Sons, Limited, 2007.

[47] D.N. Wasnik, G. Dey, Vivekanand Kain, and Indradev Samajdar. Precipitation stages in a 316l austenitic stainless steel. *Scripta Materialia*, 49:135–141, 07 2003.

[48] Nabendu Ghosh, Pradip Kumar Pal, and Goutam Nandi. Gmaw dissimilar welding of aisi 409 ferritic stainless steel to aisi 316l austenitic stainless steel by using aisi 308 filler wire. *Engineering Science and Technology, an International Journal*, 20(4):1334 – 1341, 2017.

[49] J.R. Davis and A.S.M.I.H. Committee. *Nickel, Cobalt, and Their Alloys*. ASM specialty handbook. ASM International, 2000.

[50] Adrian P. Mouritz. 12 - superalloys for gas turbine engines. In Adrian P. Mouritz, editor, *Introduction to Aerospace Materials*, pages 251 – 267. Woodhead Publishing, 2012.

[51] R.C. Reed and C.M.F. Rae. 22 - physical metallurgy of the nickel-based superalloys. In David E. Laughlin and Kazuhiro Hono, editors, *Physical Metallurgy (Fifth Edition)*, pages 2215 – 2290. Elsevier, Oxford, fifth edition edition, 2014.

[52] C. Sommitsch, R. Radis, A. Krumphals, M. Stockinger, and D. Huber. 12 - microstructure control in processing nickel, titanium and other special alloys. In Jianguo Lin, Daniel Balint, and Maciej Pietrzyk, editors, *Microstructure Evolution in Metal Forming Processes*, Woodhead Publishing Series in Metals and Surface Engineering, pages 337 – 383. Woodhead Publishing, 2012.

[53] Marco Amabili. *Nonlinear Mechanics of Shells and Plates in Composite, Soft and Biological Materials*. Cambridge University Press, 2018.

[54] J.P. Oliveira, A.D. LaLonde, and J. Ma. Processing parameters in laser powder bed fusion metal additive manufacturing. *Materials & Design*, 193:108762, 2020.

[55] Chiara Zitelli, Paolo Folgarait, and Andrea Di Schino. Laser powder bed fusion of stainless steel grades: A review. *Metals*, 9(7), 2019.

[56] Thien Q Phan, Maria Strantza, Michael R Hill, Thomas H Gnaupel-Herold, Jarred Heigel, Christopher R D'Elia, Adrian T DeWald, Bjorn Clausen, Darren C Pagan, J Y Peter Ko, Donald W Brown, and Lyle E Levine. Elastic Residual Strain and Stress Measurements and Corresponding Part Deflections of 3D Additive Manufacturing Builds of IN625 AM-Bench Artifacts Using Neutron Diffraction, Synchrotron X-Ray Diffraction, and Contour Method. *Integrating Materials and Manufacturing Innovation*, 8(3):318–334, 2019.

[57] Darby Luscher, John Yeager, Bjørn Clausen, Sven Vogel, Amanda Duque, and Don Brown. Using neutron diffraction to investigate texture evolution during consolidation of deuterated triaminotrinitrobenzene (d-tatb) explosive powder. *Crystals*, 7:138, 05 2017.

[58] A.C. Larson, R.B. Dreele, and Brian Toby. General structure analysis system - gsas/expgui. *Los Alamos National Laboratory*, 748, 01 1994.

[59] Thomas M Holden, Hiroshi Suzuki, and David G Carr. Macroscopic stress measurements by neutron diffraction and the part played by the "stress-free" reference. *ISIJ international*, 46(7):959–965, 2006.

[60] Brian Driessen. A direct stiffness-modification approach to attaining linear consistency between incompatible finite element meshes. ., 02 2000.

[61] Raphael Jean Boulbes. *Troubleshooting Finite-Element Modeling with Abaqus*. Springer International Publishing, 1 edition, 2020.

[62] Jang-Keun Lim, Tae-Han Song, and Byung-Ho Seog. Formulation method for solid-to-beam transition finite elements. *KSME international journal*, 15(11):1499–1506, 2001.

[63] Sascha Eisenträger, Albert Saputra, and Hauke Gravenkamp. High order transition elements: The xny-element concept – part i: Statics. *Computer Methods in Applied Mechanics and Engineering*, page 50, 09 2019.

[64] Klaus-Jürgen Bathe. *Finite element procedures*. Klaus-Jurgen Bathe, 2006.

[65] A. K. Gupta. A finite element for transition from a fine to a coarse grid. *International Journal for Numerical Methods in Engineering*, 12(1):35–45, 1978.

[66] D. J. Morton, J. M. Tyler, and J. R. Dorroh. A new 3d finite element for adaptive h-refinement in 1-irregular meshes. *International Journal for Numerical Methods in Engineering*, 38(23):3989–4008, 1995.

[67] C.G. Provatidis. Coons-patch macroelements in two-dimensional parabolic problems. *Applied Mathematical Modelling*, 30(4):319 – 351, 2006.

[68] Christopher Provatidis. Two-dimensional elastostatic analysis using coons-gordon interpolation. *Meccanica*, 47, 04 2012.

[69] Matthias Baitsch and Dietrich Hartmann. Piecewise polynomial shape functions for hp-finite element methods. *Computer Methods in Applied Mechanics and Engineering*, 198(13):1126 – 1137, 2009. HOFEM07.

[70] S. W. Dohrmann, C. R.; Key. A transition element for uniform strain hexahedral and tetrahedral finite elements. *International Journal for Numerical Methods in Engineering*, 44:1933–1950, 04 1999.

[71] A.C. Ugural. *Stresses in plates and shells*. McGraw-Hill Ryerson, Limited, 1981.

[72] Damien Buchbinder, Wilhelm Meiners, Norbert Pirch, Konrad Wissenbach, and Johannes Schrage. Investigation on reducing distortion by preheating during manufacture of aluminum components using selective laser melting. *Journal of laser applications*, 26(1):012004, 2014.

[73] M. Shiomi, K. Osakada, K. Nakamura, T. Yamashita, and F. Abe. Residual stress within metallic model made by selective laser melting process. *CIRP Annals*, 53(1):195 – 198, 2004.

[74] Timothy A. Burkhart, David M. Andrews, and Cynthia E. Dunning. Finite element modeling mesh quality, energy balance and validation methods: A review with recommendations associated with the modeling of bone tissue. *Journal of Biomechanics*, 46(9):1477 – 1488, 2013.

[75] Fem modeling: Mesh, loads, bcs, 2012.

[76] Cheryl E Quenneville and Cynthia E Dunning. Development of a finite element model of the tibia for short-duration high-force axial impact loading. *Computer Methods in Biomechanics and Biomedical Engineering*, 14(02):205–212, 2011.

[77] Patrick M Knupp. Algebraic mesh quality metrics. *SIAM journal on scientific computing*, 23(1):193–218, 2001.

[78] Yongjie Zhang, Thomas JR Hughes, and Chandrajit L Bajaj. An automatic 3d mesh generation method for domains with multiple materials. *Computer methods in applied mechanics and engineering*, 199(5-8):405–415, 2010.

[79] Costin Untaroiu, Kurosh Darvish, Jeff Crandall, Bing Deng, and Jenne-Tai Wang. A finite element model of the lower limb for simulating pedestrian impacts. Technical report, SAE Technical Paper, 2005.

[80] Malcolm H Ray, Mario Mongiardini, AO Atahan, CA Plaxico, and M Anghileri. Recommended procedures for verification and validation of computer simulations used for roadside safety applications. *Final Report (Draft), Project*, 1(22-24), 2008.

[81] O.C. Zienkiewicz, R.L. Taylor, and J.Z. Zhu. *The Finite Element Method: Its Basis and Fundamentals*. The Finite Element Method. Elsevier Science, 2013.

Appendix A

Fatigue Overview and Preliminary Experimental Results

A.1 Introduction

This appendix is aimed at exploring the initial underlying work plan of this research work, which due to the unfortunate circumstances of the global COVID-19 pandemic, had to be discontinued owing to the restrictions on academic and industrial activities.

One of the original main goals of this dissertation work was the development of an experimental fatigue testing plan, which aimed at comparing fatigue behaviour in components manufactured through conventional materials and additively manufactured alloys, namely precipitation-hardened Maraging steel.

With this in mind, the following appendix will be divided into two sections: Section A.2, which is a theoretical introduction to fatigue and related concepts; Section A.3, which delves into developed test pieces that were manufactured nearing the end of the semester, which allowed the attainment of several experimental values

A.2 Fatigue

A.2.1 Introduction and definition

Classical continuum mechanics, coupled with theory of elasticity, allow the engineer to determine parameters such as the admissible stress or elastic strain for static loading conditions, granting the necessary tools to design some rudimentary mechanisms. However, as intuitively deduced, most real life loading conditions vary with time, which invalidates a simpler analysis and can give way to catastrophic failure. This scenario leads to not only economical and material loss, but the possibility of endangering human lives, as happened in history before the phenomenon of fatigue was accurately studied. Perhaps one of the most striking example of fatigue failure was the sudden collapse of several *Liberty Ships*, a series of lightly armed cargo ships commissioned to supply England and France during the war effort in World War II. These ships' design was remarkably simple, so that the inexperienced workforce of recruits could nevertheless complete their manufacture in record time frames [A1]. The downside, however, came with the unexpected failure of several of these ships that quite literally snapped in half [A1]. It was later discovered that defective welds were serving as crack initiation zones, and brittle-ductile transition mechanism activated by low sea temperatures allowed for these cracks to become unstable, as mild steel became too brittle to accommodate significant deformation [A1] when subjected to the cold temperatures of the Arctic Sea.

For engineering materials, two major failure types can be found: *(i) brittle fracture*,

characterised by little to no plastic deformation, and whose surface is characterised by a relatively shiny, smooth surface [46]. This type of fracture is associated with *cleavage*, which constitutes a breakage along crystallographic planes; *(ii) ductile fracture*, defined by a considerable amount of necking. Crack propagation usually occurs at a 45° angle and is generally accompanied by microvoids that aggregate [46].

Another important distinction to highlight in this introductory subsection lies in the influence of the number of cycles within the realm of fatigue. Most of the references aimed at beginners distinguish *low-cycle fatigue* LCF and *high-cycle fatigue* HCF, with the latter being characterised by loading histories with over 10^3 cycles [A3]; more specific references recommend further division due to different failure mechanisms, establishing *ultra low-cycle fatigue* for $N < 10^2$ [A4] and *ultra high-cycle fatigue* for $N > 10^7$ [A5].

In the following subsections, different theories are explored within the three main methods of predicting fatigue life: the stress-life method, the strain-life method and fracture mechanics.

A.2.2 Stress-life method

The most traditional of the three methods for predicting fatigue failure, stress-life has the advantage of being the most accessible and easy to implement [A3]. Its main objective is determining a relation between a stress-based parameter and the number of cycles until failure, usually resorting to *S-N* curves or *Wöler* curves. These curves are data of the stress amplitude S_a plotted versus the logarithm of the number N of cycles to failure. Occasionally, the maximum or minimum value of applied stress may be used instead of stress amplitude [46]. More information about the *S-N* curves and how they are utilised to estimate a component's fatigue life is explored later in this Subsection. Naturally, the data is obtained through destructive testing, and due to the scattered nature of these values, it is imperative for a standardisation of testing systems and specimens: this information is explored in Subsection A.2.8.

Cycle counting techniques

Knowing that the construction of S-N curves is the ultimate goal for this type of analysis, one should ask what is the most accurate way of condensing a complicated loading history into a series of parameters translatable to a mathematical reality and framework. Even though this effort is but an approximation, several techniques have been explored throughout the years, such as the Rainflow cycle counting technique, firstly introduced by Matsuishi and Endo [A6] in 1968, which suggests accounting the damage by rotating the loading history ninety degrees in the clockwise direction, and imagining a water flow from each successive peak or valley, thus gaining its name. The American Society for Testing and Materials (ASTM) suggest a three-point counting technique that evaluates three peak/valleys at a time [A7]. Additional techniques aimed at multiaxial problems are the critical plane approach, which analyses all stresses in a single *critical* plane [A8], and the accumulated stress amplitude or accumulates strain amplitude, which aims at extracting accumulated damage models from the loading history [A9].

Cyclic stresses

The stress in a cycle can be described by either a combination of the stress amplitude σ_a and mean stress σ_m or by maximum stress σ_{max} and minimum stress σ_{min}. These parameters allow the definition of a sinusoidal loading history, as shown in Figure A.1,

which serves as a basis for a more in-depth mathematical analysis on fatigue life, as well as a parameter R named *stress ratio*, which is a valuable measure in subdividing loading histories according to tensile, compressive or fully reversible regimes.

$$\begin{aligned} \sigma_a &= \frac{\sigma_{max} - \sigma_{min}}{2} \\ \sigma_m &= \frac{\sigma_{max} + \sigma_{min}}{2} \\ \sigma_r &= \sigma_{max} - \sigma_{min} = 2\sigma_a \\ R &= \frac{\sigma_{min}}{\sigma_{max}} \end{aligned} \tag{A.1}$$

It's important to note that cyclic stresses may arise from axial, flexural or twisting solicitations, depending on the testing the specimen underwent. Each of these loading types has its own ramifications, a topic that is explored further in this section.

S-N curves

As aforementioned, S-N curves are graphs characterised by a stress parameter, usually stress amplitude, plotted versus the number of cycles until failure in a log-log fashion. Two types of behaviour is observed in S-N curves, depending on the analysed material, both of them schematically introduced in Figure A.2. One possible behaviour is common in ferrous or titanium alloys, where an initial decrease in stress amplitude intercepts a second phase where an increase in fatigue life does not lead to a diminishing of load capacity [46]. This limit is named *fatigue limit* or *endurance limit*, below which fatigue failure will not occur, and for many steels, this value ranges between 35 and 60% of the respective material's tensile strength [46]. The exact number of cycles that a material needs to withstand before its life is considered infinite depends on application and literary reference [A9].

The other expected behaviour, common in non-ferrous alloys such as magnesium, aluminium or copper, do not present a fatigue limit, meaning that fatigue failure will inevitably occur regardless of the involved stress [46].

Stress-based uniaxial analysis

In order to model fatigue life, failure criteria must be adopted, and three particular methods are worthy of note: Gerber (A.2), Goodman (A.3) and Soderberg (A.4).

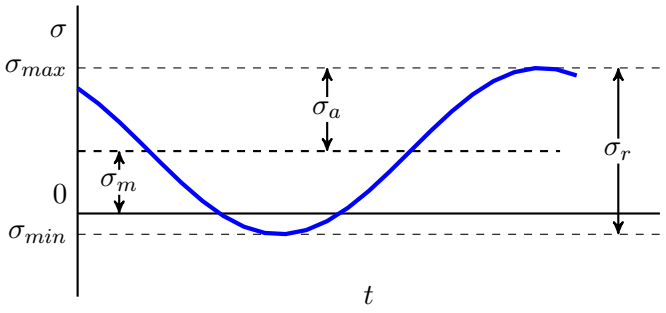

Figure A.1: Repeated stress cycle with a positive mean stress σ_m.

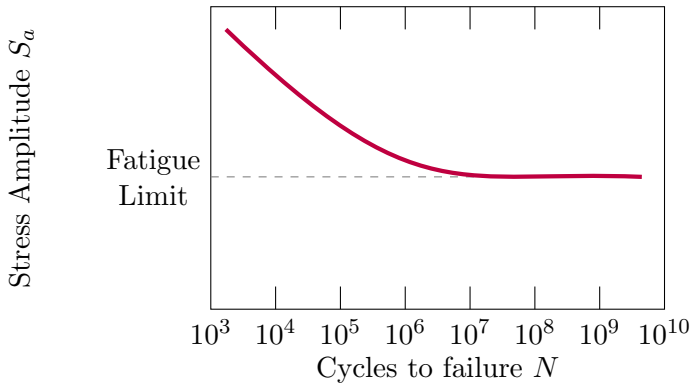

(a) Material that displays fatigue limit

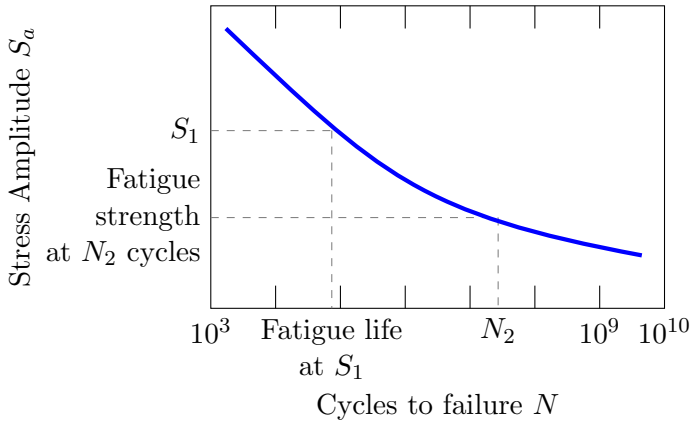

(b) Material that does not display a fatigue limit

Figure A.2: Typical behaviours of S-N curves (adapted from [46]).

$$\sigma_a = \sigma_{fo}\left(1 - \left(\frac{\sigma_m}{\sigma_{ts}}\right)^2\right) \tag{A.2}$$

$$\sigma_a = \sigma_{fo}\left(1 - \frac{\sigma_m}{\sigma_{ts}}\right) \tag{A.3}$$

$$\sigma_a = \sigma_{fo}\left(1 - \frac{\sigma_m}{\sigma_y}\right) \tag{A.4}$$

The Soderberg criteria is the most trustworthy, as it aims to prevent plastic deformation [A10]; Goodman's criteria also avoids plastic deformation by imposing $\sigma_m + \sigma_a = \sigma_y$. If a pessimist analysis is warranted, it's advisable the use of the stress value as an absolute so that compressive stresses do not result in a larger admissible stress amplitude [A10].

Stress-based multi-axial analysis

There are two main scenarios applicable to multi-axial fatigue analysis: *proportional* and *non-proportional* loading.

Non-proportional loading contemplates the multiaxial loading paths that cause the principal stress axis or maximum shear stress axis of a local element to rotate with time, and with respect to a local coordinate system, while in proportional loading, the principle

stress axis is stationary [A9]. Generally, non-proportional loading results in more damage for the same von-Mises stress range due to additional strain hardening [A11].

Furthermore, there are four main classification of multi-axial analysis possible: the empirical formula approach, equivalent stress approach, critical plane approach and Dang Van multiscale approach [A9]. The empirical formula approach is exclusively applied to the biaxial stress state in a fully revered loading condition ($R = 1$), and it provides tools to estimate the admissible normal and shear stress. The equivalent stress approach uses failure criteria to estimate admissible stress, and has been subjected to adaptations to account for hardening effects [A12]. The critical plane approach identifies the plane in which damage will most likely occur, as the name implies, and the Dang Van multiscale approach tackles mesoscopic fatigue damage at fatigue limit conditions [A9].

A.2.3 Strain-life method

The strain-life method attempts to determine fatigue strengths by establishing total strain as a fatigue parameter [A13]. In 1910, Bairstow observed that the elastic limit of steel could be altered both upwards or downwards by cyclic variations of stress: while annealing generally increased the elastic limit, cold-working decreased it [A14]. Much later, in 1968, Landgraf analysed the behaviour of high strength steels under low cycle fatigue, and plotted the results in true stress-strain hysteresis loops such as the one presented in Figure A.3 [A15]. These hysteresis loops highlight the three partly overlapping stages of the fatigue process: *(i) fatigue hardening/softening*, a consequence of the interactions between structural defects of the loaded volume; *(ii) crack nucleation* and lastly *(iii) crack propagation* [A13]. It is also worthy of note that plasticity is considerably more impactful in low-cycle fatigue [A12].

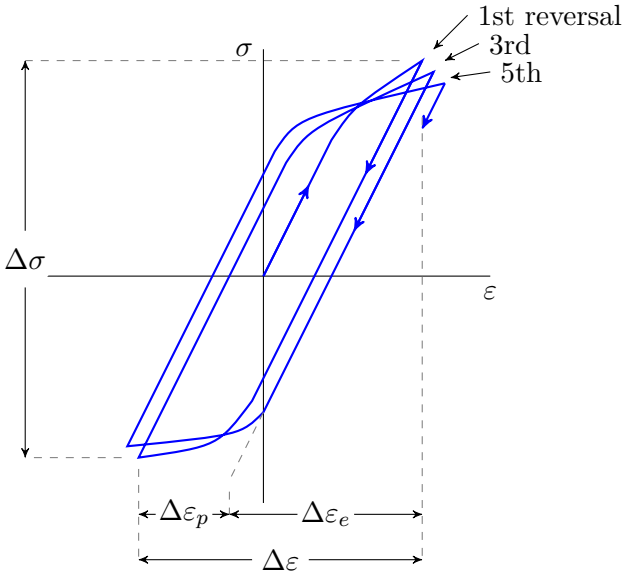

Figure A.3: Hysterisis loop showing the first five stress reversals (adapted from [A3]).

Additionally, one can plot multiple reversals in the same coordinate system, allowing the construction of the cyclic strain-stress curve by linking the loop tips of each uneven-th reversal [A12]: mathematically, this results in the Ramberg-Osgood equation [A16].

$$\varepsilon = \varepsilon_e + \varepsilon_p = \frac{\sigma}{E} + \left(\frac{\sigma}{K'}\right)^{1/n'} \tag{A.5}$$

where K' is the cyclic strength coefficient, n' is the cyclic strain hardening exponent and the superscript $'$ differentiates monotonic properties from cyclic ones. In 1926, G. Masing proposed a similar relation for the stress and strain amplitudes, which assumes that symmetric behaviour in tension and compression, a valid consideration for homogeneous materials [A17]. Later, in 1965, based on Morrow's proposal [A18], the total strain amplitude and the fatigue life to failure was established through Basquin's work on elastic strain [A19], present in Equation (A.6), and the Coffin-Manson equation that relates it to plastic strain [A20], as exemplified in Equation (A.7).

$$\frac{\Delta\varepsilon_e}{2} = \frac{\sigma_a}{E} = \frac{\sigma'_f}{E}\left(2N_f\right)^b \tag{A.6}$$

$$\frac{\Delta\varepsilon_p}{2} = \varepsilon'_f\left(2N_f\right)^c \tag{A.7}$$

$$\frac{\Delta\varepsilon}{2} = \frac{\Delta\varepsilon_e}{2} + \frac{\Delta\varepsilon_p}{2} = \frac{\sigma'_f}{E}\left(2N_f\right)^b + \varepsilon'_f\left(2N_f\right)^c \tag{A.8}$$

where σ'_f and ε'_f are the fatigue strength coefficient and the fatigue ductility coefficient, respectively; b and c are the fatigue strength exponent and fatigue ductility exponent, respectively. These parameters establish the *strain-life equation* for zero mean stress; when plotted in a log-log axis, both terms of the equation become straight lines, where its intersection defines the transition fatigue life in reversals [A12], as exemplified in Figure A.4.

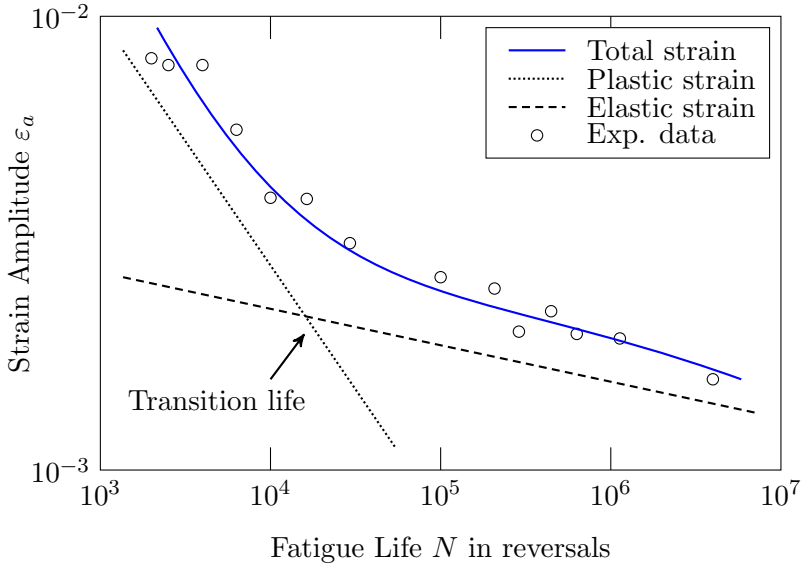

Figure A.4: Schematic of a total strain amplitude-life curve (adapted from [A12]).

The regime to the left of the transition life point is dominated by plasticity, and therefore linked to low-cycle fatigue, while the right-handed side is relevant to high-cycle fatigue [A12]. Steels with larger ultimate tensile strengths and hardness generally present lower transition lives [A12].

Adaptations to contemplate non-zero mean stresses have been made by Morrow [A21], alterations that found particular success in steels, while for materials such as Ti-6Al-4V, the mean stress value σ_m showed better results when multiplied by a correction factor [A22]. An interesting effect originated by a compressive mean stress is an increased fatigue life [A12].

Smith, Watson and Topper developed another theory that models total strain amplitude by postulating that the strain amplitude of a fully reversible cycle must be equal to the product of the maximum stress with the strain amplitude [A23].

$$\sigma_{max} \cdot \varepsilon_a = \sigma_{a,rev} \cdot \varepsilon_{a,rev} \ , \ \sigma_{max} > 0 \tag{A.9}$$

Lastly, regarding multi-axial strain-life theories, the last four decades have witnessed attempts to establish reasonable mathematical formulations for cyclic multiaxial plasticity; these efforts, however, require a large number of material constants to achieve reasonable correlation between simulation and experimental data [A13]. In fact, Even the simplest of plastic problems - assuming no temperature change, no anisotropy and no rate-dependent yielding - still constitutes a challenging effort for engineering: however, strain life methods may become more predominant in the future [A3], as finite element analysis becomes industry standard, coupled with faster and more powerful computing machines capable of solving complex problems in reasonable timeframes.

A.2.4 Fracture mechanics

Fracture mechanics find its place in modern machine design by taking into account geometric defects present in materials even before they have been solicited [A3]; it complements other fatigue analysis methods, such as stress-life. This doesn't mean the considered material is necessarily incapable of performing the desired task, but it means the engineer must be wary of crack initiation and growth rates throughout a part's service life. This particular field of engineering started in 1920 through Griffith's work, as he was intrigued by the fact that materials' tensile strength appeared to be inferior to the theoretical value deduced through atomic considerations [A10]. His conclusion was precisely that microscopical imperfections already present in the material decrease its resistance, and that for brittle materials [A24] (he worked with crack propagation in glass) a decrease in elastic strain potential energy per unit thickness is accompanied by an increase in superficial energy in unit thickness, resulting in crack growth [A10].

The mathematical translation of this conclusion is present in Equation (A.10), laying the foundation of Linear Elastic Fracture Mechanics (LCF):

$$G_I = \frac{\pi a \sigma^2}{E} \tag{A.10}$$

where G_I represents the *strain energy release rate*, which as the name implies, quantifies the amount of released energy from the system through the process of crack propagation. The subscript I is associated with mode I of fracture, out of three possible: mode I, equating with tensile stress, the most common and well researched of all modes [A3]; mode II, *sliding mode*, relating to in-plane shear; mode III, *tearing mode*, regarding out-of plane shear [A3]. The visual representation of these modes can be found in Figure A.5.

As Griffith's work was exclusively on brittle materials, both Irwin [A25] and Orowan [A26] furthered his theory to account for plastic strain work γ_p in the fracture process, as it effectively dwarfs the contribution of surface energy in ductile materials [A25, A26]. This resulted in Equation (A.11), where another relevant concept is introduced: *stress*

intensity factor K_i, not to be confused with the stress concentration factor K_t. The latter is the quantification of localised stress effects due to macroscopic geometric features, while the former exists due to microscopical imperfections and defects [A3]. Furthermore, K_t is a function of dimensional characteristics of the part's geometry, while K_I is a function of geometry, size and shape of the crack, loading type and in occasional situations a modification factor as well. Its mathematical definition is found in Equation (A.12).

$$G_I = \frac{K_I^2}{E} \tag{A.11}$$

To note that when the stress intensity factor is known, the stress field at the crack tip is defined [A27] as long as there's little plastic deformation; additionally, the critical value of this factor may be expected as a material property, commonly referred to as *fracture toughness* K_{IC}, that gives the engineer valuable insight into acceptable crack lengths before catastrophic failure. Values for fracture toughness are generally well documented in literature [A28]. The fracture toughness values are a function of thickness up to a point, until they reach a condition of plane strain [46].

$$K_I = \beta \cdot Y \cdot \sigma\sqrt{\pi a} \tag{A.12}$$

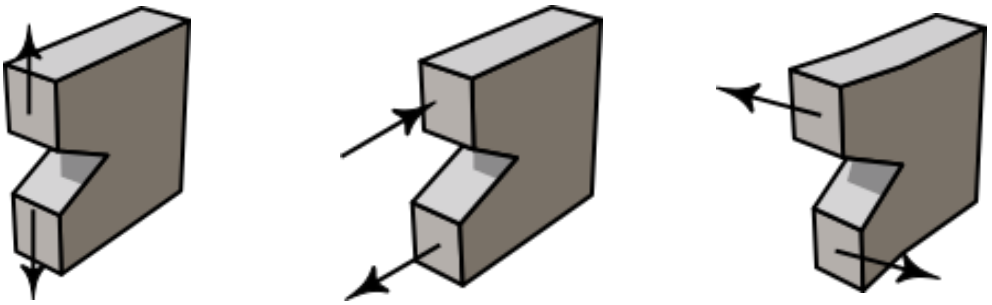

(a) Mode I - *tensile stress* (b) Mode II - *sliding* (c) Mode III - *tearing*

Figure A.5: Modes of fracture.

However, fracture toughness by itself provides no insight on the plastic behaviour of crack propagation, specially in the case of high toughness materials [A27]. The problem of crack tip plasticity was first tackled by Irwin and Dugdale in independent fashion, arriving at conclusions through differing methods: Irwin used the concept of virtual or effective crack length, whose extension Δa would need to sustain the difference between the singularity's theoretical stress and the actual yield stress it's subjected to [A29]. Alternatively, Dugdale proposed a model where a hypothetical stress, with the magnitude of the yield strength, would *close* the effective crack length [A30]. A comparison between each model can be found in Figure A.7.

This concept of effective crack length allows the definition of additional parameters that characterise its growth and general behaviour, useful for ductile materials [A28]: (*i*) δ_m = Crack mouth opening displacement (CMOD); (*ii*) δ_t = Crack tip opening displacement (CTOD); (*iii*) δ_5 = Crack opening displacement (COD); (*iv*) ψ_t = Crack tip opening angle (CTOA). ASTM provides guidelines on how to determine each one, and their visual representation is present in Figure A.6.

When paired with failure criteria the elasto-plastic zone can be determined. It may be of interest to analyse the visual distribution of this area in function of plain stress or plain strain, as well as in function of mode of loading [A27] and failure criteria. Attempts have

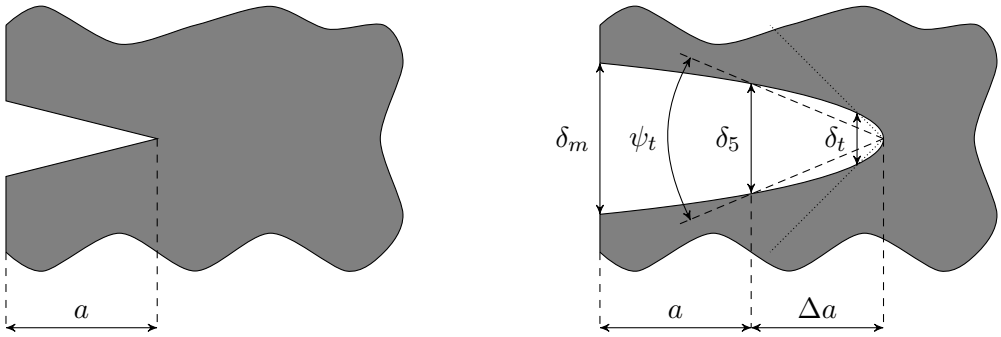

Figure A.6: Fracture parameters: δ_m, δ_t, δ_5 and ψ_t.

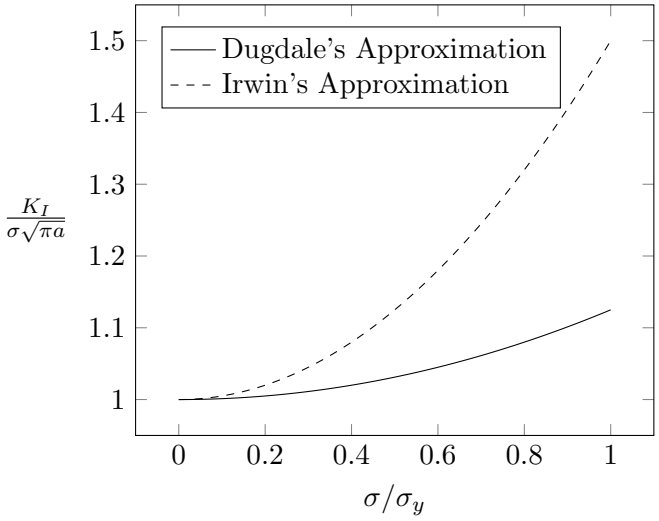

Figure A.7: Comparison between Dugdale's and Irwin's normalised stress intensity factor approximation.

been made to experimentally measure these areas, [A31], and finite element methods have been used to complement the analytical approach [A32].

Still on the subject of fracture mechanics, it is of value the discussion of situations where localised plasticity hampers the computation of the strain energy release rate G through Equation (A.10) and alternative methods must be employed. Cherapanov [A33] and Rice [A34] employed Eshelby's work on analytical methods of strain energy calculations to the problem of crack propagation, to determine the energy associated with crack propagation even in the case of significant plasticity. This resulted in the J-integral, a path independent integral that establishes an energy equilibrium around the crack, and computes the change potential energy per increase in crack length da [A27]. The mathematical definition is found on Equation (A.13).

$$J = \int_{\Gamma} \left(W dy - \boldsymbol{T} \frac{\partial \boldsymbol{u}}{\partial x} ds \right) \tag{A.13}$$

where W is the strain energy density, $\boldsymbol{T}$ is the tensile vector, $\boldsymbol{u}$ is the displacement vector and ds is the infinitesimal contour element of the path Γ. In the case of a fully closed path Γ, J must be zero by definition [A27]. Additionally, it is important to quantify the relation between fracture toughness and the number of cycles a component has been subjected to, for obvious practical application; this is done by conducting tests that allow the relation between the effective crack length a and the number of cycles N. Results

are then plotted against da/dN versus ΔK axis, where three main areas can be easily distinguishable: *(i) crack initiation*, where a crack has just been created and its overall significance is negligible [A10]; the second regime, characterised by its linearity, constitutes the area in which a crack increases in a steady and easily describable fashion [A35]: its mathematical definition is presented in Equation (A.14), widely named Paris' Law due to the contributions by Paul Paris in the study of fatigue and crack propagation. Lastly, the last stage is where failure is imminent and a component is no longer reliable [A10]: all three of these stages are schematically shown in Figure A.8.

$$\frac{da}{dN} = C\,(\Delta K)^m \tag{A.14}$$

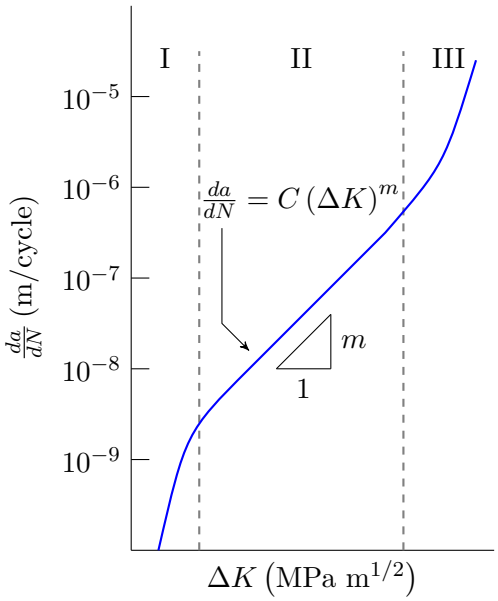

Figure A.8: Schematic representation of a typical $da/dN = f\,(\Delta K)$ curve (adapted from [A10]).

A.2.5 Fatigue life and modifying factors

Naturally, fatigue data has a significant amount of associated scatter; S-N curves are built by curve-fitting data points across many results for the same experimental scenario, but even with careful repetition and external factor supervision, results are bound to be approximate in nature [A9]. This implies that fatigue design is a probability-management process, and that certain corrections linked to the manufacturing process, size, temperature, surface roughness, among other phenomena can be applied to increase the level of confidence [A10]. This concept mathematically translates into Equation (A.15), where every correction factor of the four presented will be briefly explored.

$$\sigma_f^{co} = \sigma_f \cdot C_1 \cdot C_2 \cdot C_3 \cdot C_4 \tag{A.15}$$

The first correction factor C_1 is related to the loading type: usual values are 0.85 for axial loading, 1.0 for pure bending and 0.58 for torsion [A10]; the second correction factor C_2 quantifies the size effect of the part, as larger section areas are tied to sharper stress gradients [A10]; C_3 encompasses surface finishing effects, such as roughness-induced stress

concentrations or the introduction of residual stresses that act as crack initiation zones, as it's defined as the quotient between the fatigue limit of a specimen with certain surface conditions and a polished sample [A10]; this factor is highly impact, as the example of forged steel highlights, in which C_3 is as low as 0.54 [A3]: more on the calculation of this factor is encouraged [A36]. Lastly, C_4 contains all other relevant information, such as temperature effects, environmental phenomena like corrosion, or material properties as anisotropy [A10].

It is worthwhile to highlight the fact that some authors [A3] further divide the mentioned correction factors into more specific categories to account for other phenomena.

A.2.6 Stress concentration and notch sensitivity

Briefly mentioned in Subsection A.2.4 regarding fracture mechanics, the stress concentration factor K_t is a physical constant negligible in static loading conditions, but crucial in the study of fatigue, that represents the localised increased in stress a component experiences due to geometrical irregularities [A37].

The subscript t implies the specified concentration factor is theoretical, and the practical experimental case is given by the subscript f. The relationship between these two distinct factors is established through the *notch sensitivity factor* q, and these concepts are mathematically represented in Equations (A.16) and (A.17), and schematically represented in Figure A.9.

$$\sigma_{max} = K_t \ \sigma_{nom} \tag{A.16}$$

$$q = \frac{K_f - 1}{K_t - 1} \tag{A.17}$$

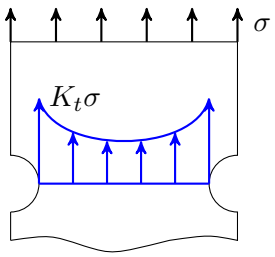

Figure A.9: Schematic representation of the stress evolution in a notched component.

Concentration factors vary with several factors, as they are a function of the loading type, material and its potential heat treatments besides the obvious geometrical characteristics of the component. In case of multiaxial loading, different concentration factors must be used, with each appropriate factor multiplying the respective solicitation amplitude [A10].

A very important hallmark of stress concentration factors is R.E. Peterson's work [A37], as he compiled hundreds of relations established by himself and others in books that are still relevant to this day, even within the broader context of FEM analysis [A3].

As aforementioned, this factor tends to infinity within the presence of sizeable cracks, thus rendering it useless and calling for the use of the stress intensity factor K_I, which is appropriately portrays the stress field near a crack tip.

A.2.7 Accumulated damage

When subjected to variable loading conditions, a component's behaviour is often described through damage rules that attempt to define loading cases that share similar parameters, and add each of their contributions to assess a component's expected life cycle [A3]. These methods feed off the cycle counting techniques explained in Subsection A.2.2, calculate fatigue damage associated to each loading case and compare it to a constant defined experimentally. The most popular cumulative damage law is *Miner's law*, or *Miner's rule*, shown in Equation (A.18).

$$\sum_{i=1}^{r} \frac{n_i}{N_i} \leq 1.0 \tag{A.18}$$

where r is the total number of loading cases. Alternatively, the second member of Equation (A.18), represented as a unitary value, can be replaced by a different constant, usually constrained between 0.7 and 2.2, as suggested by the Palmgren-Miner rule [A3].

A.2.8 Fatigue tests

The last subject within the broader contest of fatigue that will be introduced is fatigue testing: as previously pointed out, fatigue is a field of mechanical engineering that relies heavily on experimental data, and therefore necessitates strict guidelines to assure repeatability across multiple tests. Fatigue test specimens can broadly be categorised according to their mode of loading: *(i)* direct axial stress, *(ii)* plane bending, *(iii)* rotating beam, *(iv)* alternating torsion and *(v)* combined stress [A38].

Independently of the test type, most fatigue testing machine systems present the same basic components: a load train (consisting of a load frame, gripping devices and a loading system), controllers and a monitor [A38]. The control varies between older and more recent models, and automated fatigue tests are usually conducted in stress-control or strain-control conditions [A39]. Furthermore, machines usually have properly calibrated load cells, displacement transducers and strain gages, storing or sending the information in a digital format [A39].

Regarding specimens, these can usually be subdivided into three main areas: the test section and the two ends. The latter are specially designed to be smooth to avoid any significant stress concentration and thus reducing the fatigue capacity, while the former is designed to bear the load of the test. Naturally, the sample's shape and dimensions must be aligned with the test's loading type and objective's [A38]; schematic representations of used specimens are present in Figure A.6. As fatigue data displays considerable amounts of scatter, it is advisable to conduct multiple tests on the same specimen type and machine, allowing the construction of probability stress-life plots [A40].

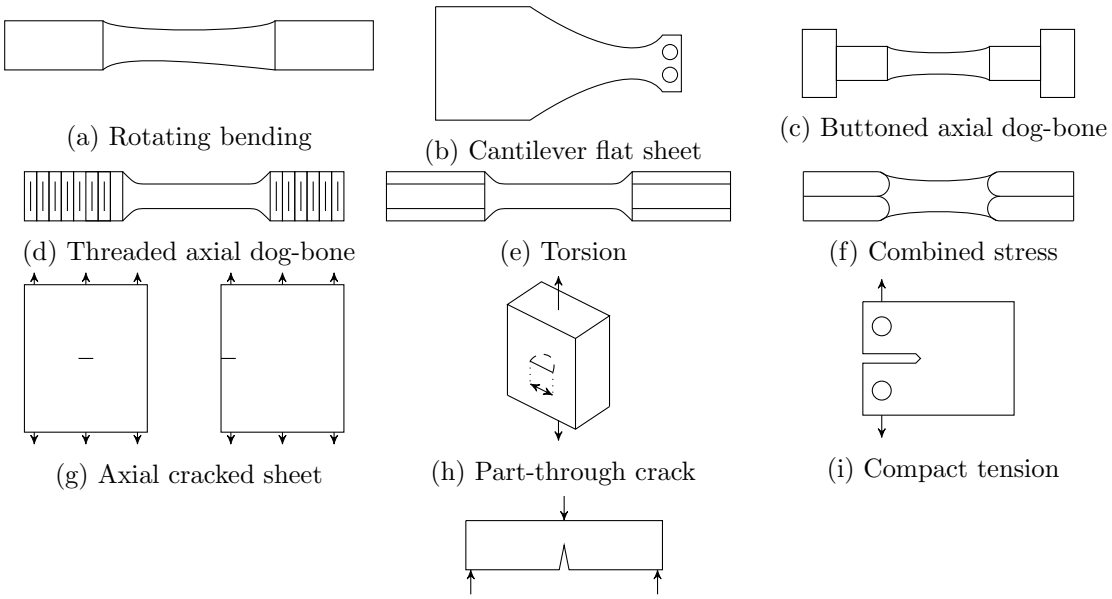

(a) Rotating bending
(b) Cantilever flat sheet
(c) Buttoned axial dog-bone
(d) Threaded axial dog-bone
(e) Torsion
(f) Combined stress
(g) Axial cracked sheet
(h) Part-through crack
(i) Compact tension
(j) Three point bend specimen

Figure A.10: Fatigue specimens.

A.3 Preliminary results

The conducted fatigue tests' objective is characterising the fatigue behaviour of additive manufactured components by establishing the S-N curves of both specimens produced via conventionally processed materials and through AM.

The dimensions and geometrical definition of the specimens is given in Figures A.11a and A.11b, corresponding to the component produced via AM and the conventional one, respectively. Their different geometries are solely justified due to limitations associated with the material at hand, as INEGI did not have raw material with the dimensions capable of being manufactured to the specimen represented in Figure A.11a.

The aforementioned conventional material is Maraging steel, which in turn was not subjected to any heat treatment. However, the AM produced component was heat-treated with a heating stage from an ambient temperature, equal to 27 °C, to the temperature of 510 °C in a 60 min period, and subsequently maintained at 510 °C for the duration of 6 h. The fact that one sample is heat-treated while the other one is not is far from ideal, considering that samples vary in geometry, manufacturing process and the presence of heat treatment. The ageing chart of the used material can be found in Figure A.12, highlighting the hardening potential for Maraging steels.

The conducted fatigue test was purely axial, force-controlled at constant amplitude and stress ratio $R = 0.1$, with normalised axisymmetric specimens according to the ASTM-E466 norm. The fatigue tests were not done until fracture, but rather until strains of 1.5% were achieved. The stresses at this level of strain was of 1006 MPa and 1870 MPa for the conventional sample and the additively manufactured one, respectively. The results of the conducted fatigue analysis are shown in Figure A.13.

Through these results, the S-N curve was established via the least squares method, knowing that the equation that relates the stress range σ_r with the number of cycles to failure N_f is given by Equation (A.19):

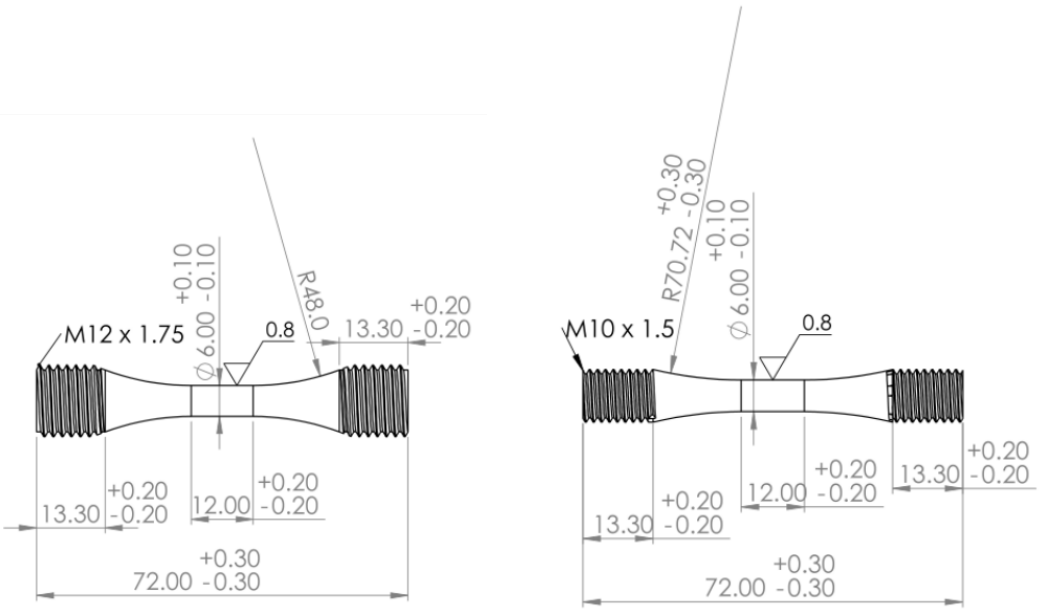

(a) AM specimen

(b) Conventional specimen

Figure A.11: Specimens for axial fatigue analysis.

$$\sigma_r = \chi N_f^{\epsilon} \tag{A.19}$$

where χ and ϵ are two experimentally determined parameters. Through the obtained results, χ and ϵ were determined, and their values are shown in Table A.1.

Table A.1: S-N curve parameters for AM and conventional specimens.

Material	χ	ϵ
AM	203 x 10^7	-0.0618
Conventional	132 x 10^7	-0.0640

It is important to note that this is an initial estimate, and that the use of only four points for the determination of an S-N curve is not advisable, specially keeping in mind the scattering nature of fatigue data. However, this is still a preliminary analysis that is nevertheless relevant.

To put the obtained values in perspective, other experimentally obtained parameters are shown in Table A.2. These two obtained results are taken from Prata (2019) [A42] and Melo (2020) [A43]'s work, previous collaborators involved in the *Add.Strength* project: their values were determined in miniature specimens subjected to bending loading, and therefore a direct comparison cannot be made.

However, it allows the conclusion that the fatigue behaviour of AM produced parts is worse than what would be expected, if the difference between yield strengths is analysed: considering that the heat-treated AM sample displayed a yield strength 1100 MPa greater than the conventional sample, a considerably better fatigue behaviour should occur.

However, imperfections and defects that develop during the manufacturing process seriously hinder the material's integrity.

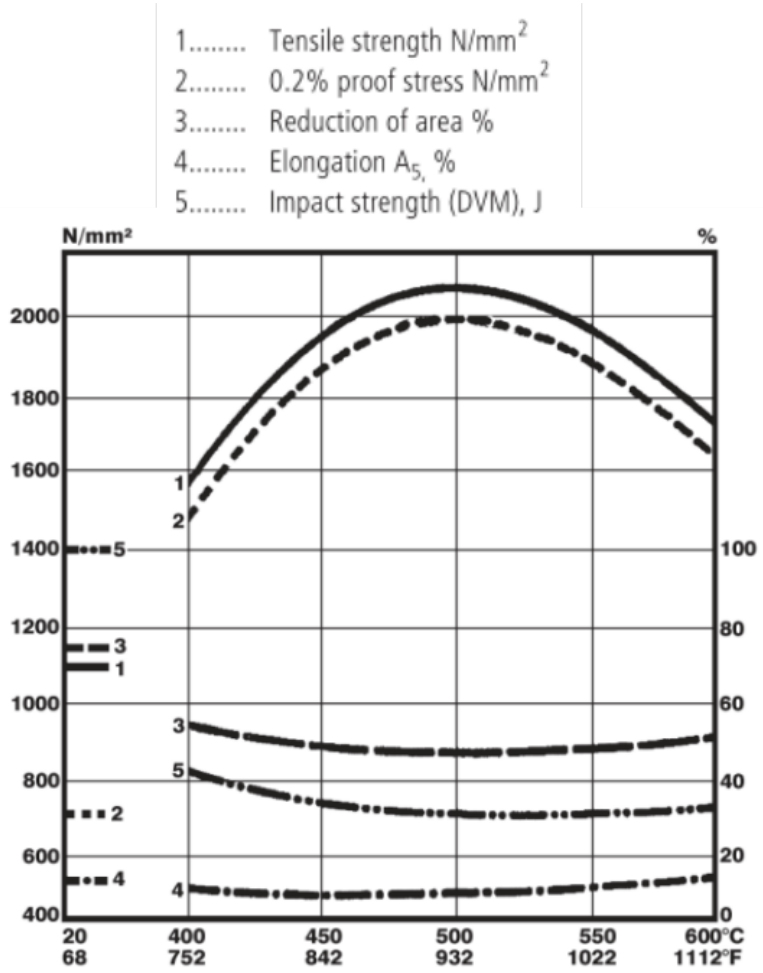

Figure A.12: Ageing chart for Maraging steel (holding time of three hours) (adapted from [A41]).

The fracture zone of two specimens can be observed in Figures A.14a-A.14d. As highlighted in Figure A.14c, there were several defects associated with the AM process, underlining the generally poor fatigue behaviour of AM produced parts. These defects, such as poor melting zones, inclusions and pores work as crack initiation zones [A44] and severely hinder the material's mechanical capacities.

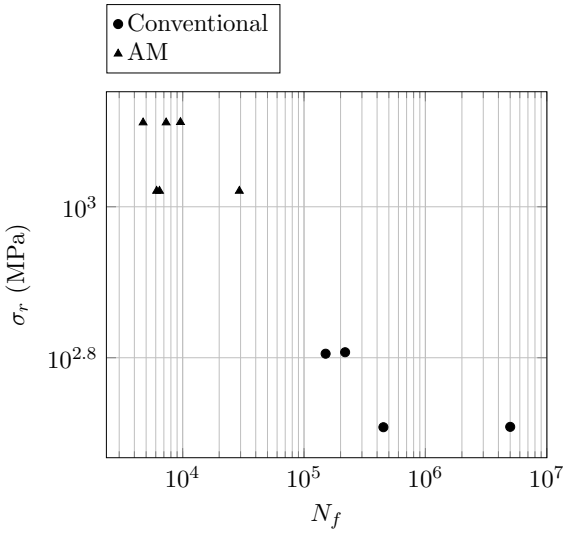

Figure A.13: Fatigue testing results, shown in logarithmic representation.

Table A.2: S-N curve parameters for miniature specimens under bending loading conditions.

Material	ϵ
Conventional [A43]	-0.071
Heat treated AM [A43]	-0.086
Conventional [A42]	-0.076

(a) AM specimen

(b) Conventional specimen

(c) AM specimen detail

(d) Conventional specimen detail

Figure A.14: Fractured specimen photos detailing fracture zones resulting from fatigue testing.

Appendix B

Distortion Evaluation Experimental Procedure

B.1 Electrical discharge machining

B.1.1 Introduction and definition

Electrical Discharge Machining (EDM) is the process by which material is electrically machined through precisely controlled sparks between the workpiece and an electrode, in the presence of a dielectric environment [A45]. The spark effectively vaporises the material without requiring physical contact, which constitutes the largest difference between EDM and most other chip making procedures [A46] that remove material through mechanical contact between the cutting tool and the workpiece, coupled with relative movement and tool force [A47]. In short, EDM is a thermal process: material is removed by heat, with the spark area reaching temperatures as high as 12 000 °C [A46].

These conditions, however, are not maintained through long stretches of time; instead, the sparking process is an infinitesimal event that repeats with frequencies varying from 2000 to 500000 times per second [A45]. It is important to note, additionally, that there are two distinct types of EDM: *die-sinker* EDM and *wire-cute* EDM, both of which shall be explained further.

A full die-sinker EDM cycle can be described as follows, and visually represented in Figure B.1:

1. The electrode approaches the workpiece, causing the alignment of particles present in the dielectric fluid and the decrease in electrical resistance of the circuit formed by the electrode, the power supply and control systems, and the workpiece. The fluid, therefore, switched from an insulating nature to a conductive on, in a process called *ionisation* [A45];

2. The proximity between the electrode and the workpiece finally allows the creation of an energy column in the form of a spark, closing off the electrical circuit. This lowers the voltage across the terminals, drastically increasing the current, hence creating the conditions for elevated temperatures and enabling the vaporisation of excess material. The vaporisation process translates into the appearance of gases - hydrogen, carbon, various oxides [A46] - that misalign the electrical particles and eventually cause the extinction of the spark, leading to the next stage of the cycle;

3. In this stage, the plasma hot area around the now extinct spark collapses, enabling new dielectric fluid to take its place;

4. Fluid fully engulfs the to-be machined area, decreasing resistivity and creating the same conditions for spark formation.

Generally speaking, lower frequencies are used for rough machining while higher frequencies are used in finish machining - Figure B.2; this being said, there are some materials that require naturally high frequencies, such as titanium, copper and carbides [A46].

As aforementioned, the electrode advances into the workpiece through an insulating fluid called *dielectric fluid* that provides several benefits: it cools down the workpiece from the extreme temperatures caused by the electric spark; it provides insulation towards premature sparks, and removes potential chips that would otherwise damage the quality of the process [A46].

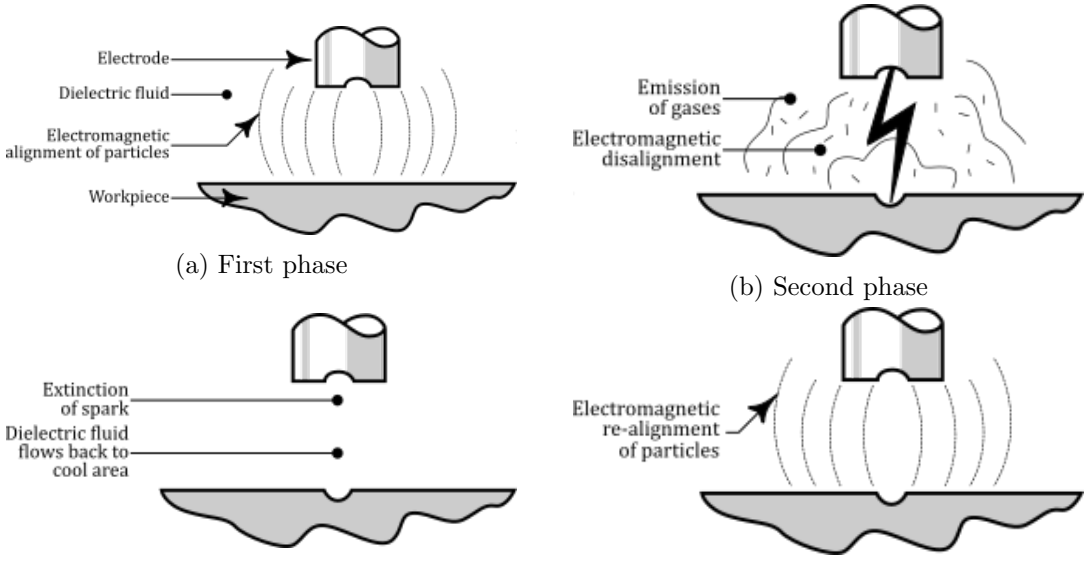

(a) First phase

(b) Second phase

(c) Third phase

(d) Fourth phase

Figure B.1: EDM cycle phases.

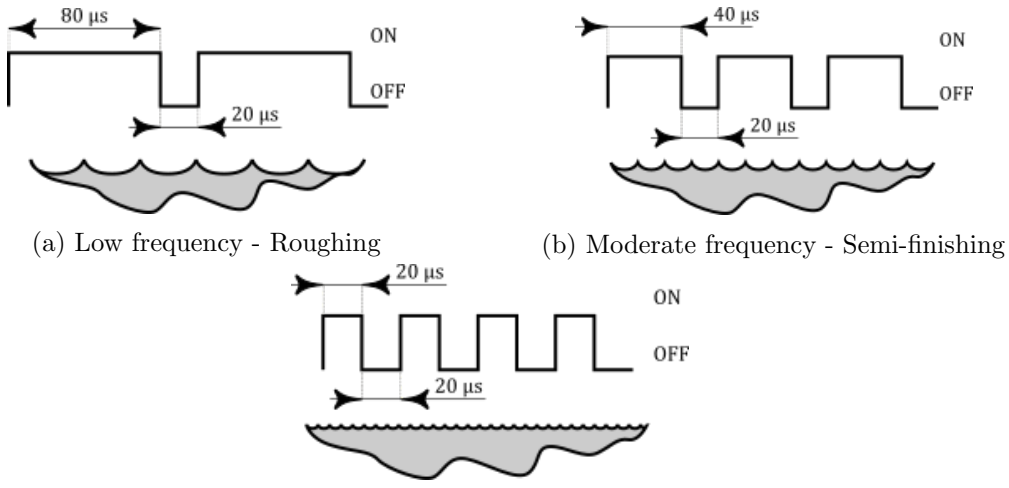

(a) Low frequency - Roughing

(b) Moderate frequency - Semi-finishing

(c) High-Frequency - Finishing

Figure B.2: Visual representation of frequency's impact on finishing.

WEDM does not differ much from the explanation provided above: an electrically charged wire advances through the workpiece, converting electric energy into a channel of plasma that vaporises excess material [A48]. However, in an attempt to reduce the need for complex (and often expensive) electrodes, manufacturers started conceiving machines

that would replace these with thin wires [A48] for the same effect. In wires, though, only its frontal section area contributes to the spark area, in regards to the direction in which the tool advances, as shown in Figure B.3. After the material is melted away, the spark area collapses and thus fluid flows back into the area, creating new conditions for the following spark, in an analogous process to the one visually represented in Figure B.1.

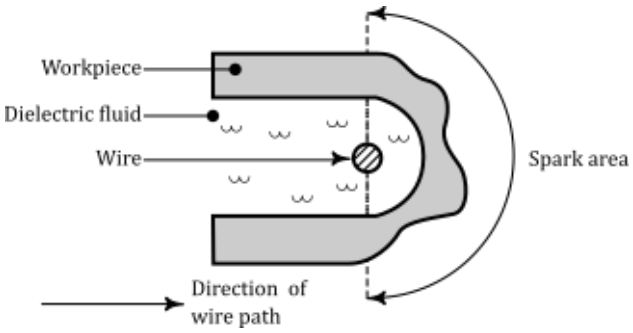

Figure B.3: Visual representation of WEDM.

The main differences between EDM and WEDM would, therefore, be not in underlying theoretical principles, but rather in functional characteristics [A48] explained ahead.

Dielectric fluid

- Die-sinker EDM machines usually use hydrocarbon oil and completely submerge the workpiece in fluid. Deionised water presents too low a viscosity, leading to larger electrode wear;

- Wire EDM machines generally use deionised water and contain only the sparking area [A45] (modern techniques, however, have been subverting this trend completely submerging the workpiece promotes temperature stabilisation and more efficient flushing of chips) [A48].

Applications

- Die-sinker EDM machines favour the manufacture of three-dimensional geometries;

- Wire machining is almost exclusively used in through hole machining.

Sparking and sparking area

- Die-sinker machinery produces spark between the bottom corners of the electrode and the surface of the workpiece, with spark characteristics (length, intensity) being functions of machine controls;

- Wire EDM machines produce sparks between the wire's frontal area as it progresses inwards, and the workpiece itself.

As any other engineering process, current day EDM technology is a far cry from its initial state, as explored in Subsection B.1.2.

B.1.2 Developments

The creation and development of EDM can be traced to the height of World War II, both in the USA and USSR in an independent fashion. Regarding the USSR, in 1941, Dr. Boris Lazarenko and Dr. Natalya Lazarenko were tasked by the USSR government to address a common problem in automotive-engine breaker points made out of tungsten, which was that of pitting: frequent sparking between components caused excessive wear and would require undesired maintenance. Interestingly enough, this problem remained unsolved, as the Lazarenkos used their observations on controlled sparking via the presence of a fluid to build the first ever EDM machine, resorting to resistor-capacitor circuit systems to power the oscillating sparks [A45].

Developments in the USA, however, were kick-started when three engineers by the names of Harold Stark, Victor Harding and Jack Beaver were assigned a project to remove broken taps, as at the time, drills and taps would frequently brake within the valve body during production. Their approach to this problem was the creation of controlled sparks that would destroy the inner unwanted objects, and flush them with water - that would too serve as dielectric fluid [A45].

After the end of the second word war, recovering countries such as Japan, Germany and the USSR underwent industry rebuilding programs that readily accepted EDM as a valid manufacture process, boosting research and development in the area [A45]. Nowadays, electrical discharge machining is widely regarded as an efficient method of machining with great precision and guaranteeing the manufacture of complex geometries that would be extremely difficult or downright impossible to produce otherwise [A45].

B.1.3 Parameters

There are some machining parameters worth mentioning for their impact in the final result obtained. Firstly, the concept of *on-time* and *off-time*, ever present in control terminology. In this context, on-time corresponds to the total amount of time a spark is established between the workpiece and electrode per unit of time, and off-time the opposite. The machining parameters under each of these envelopes of a duty cycle present their own challenges and influence the final quality of the piece in different ways.

On-time

- Speed: Machining speed is intrinsically tied to on-time, as larger spark intervals melt bigger metal pools at once. Intuitively, this affects finishing quality.
- Finish: Finishing quality depends heavily on frequency for the reasons explained above, and as presented in Figure B.2. The objective of EDM and its user is often striking a balance between machining speed, in order to obtain products at a reasonable pace, and the finishing quality.
- Wear: Every spark chips away particles belonging to the workpiece, as well as the electrode. This implies that larger cadences result in larger electrode wear.

Off-time

- Speed: Larger off-time intervals result in lower speeds, as it translated to longer periods of time where there is no work being done to the workpiece.

- Stability: The consequence of insufficient off-time is erratic cycles that negatively affect the servomotor's ability to progress forward [A46], slowing down the process further.
- Wear: Off-time has no direct relation to wear.

Polarity too plays a part in surface finishing quality: most machines operate utilising a positive electrode, which protects it from excessive wear. Exceptions are made when machining titanium, carbides and refractory metals when using metallic electrodes. Wire Electrical Discharge Machining machines, however, run with negative polarity almost exclusively [A46].

Regarding current, the necessary applied current is proportional to the intended work surface area: rule of thumb states an area-amperage ratio of approximately 65A for each 650mm. Larger currents are usually avoided due to uncontrolled heat treatments, specially if the material has low diffusivity coupled with low-frequency machining.

Additionally, it is important to further discuss the dielectric fluid's objectives, which can be broken down into four main categories:

- Removal of chips;
- Cooling the electrode and the workpiece;
- Cooling and flushing the resulting chips;
- Forming a barrier that works both as insulator and conductor, depending on circumstances [A45].

While hydrocarbon fluids maintain their dielectric nature during sparking, water changes characteristics as it absorbs the resulting chips, becoming more conductive while the process progresses [A45]. This may seem unwanted, but in WEDM, it is recurrent to use fluid as a high-velocity stream that primarily flushes chips away.

B.1.4 Materials

It is important to discuss the characteristics different materials convey both to the electrode, as well as the workpiece. At conception, brass was the only considered electrode material due to its inexpensive nature [A46]. However, high rate of wear lead to its replacement by copper, that although presented better wear performances, still presented issues related to its melting point of 1083 °C (as aforementioned, EDM temperatures may reach temperatures around 12 000 °C [A46]). The next step in EDM electrode evolution was the use of graphite, a metalloid that undergoes a process called sublimation when exposed to temperatures above 3500 °C, in which it undergoes the direct transformation from a solid state to a gas. Other advantages that graphite brought to the table were is ease in fabrication and handling, as it is generally has good machinability, if appropriate tooling is used. It's downsides arises in the fact that during machining, it originates clouds of graphite dust, and requires carbide-tipped tools to effectively machine; furthermore, it is expensive, costing on average three times more than copper [A46].

A more in-depth analysis on each material is presented.

- Brass: Inexpensive and readily available; presents decent wear when machining steel [A46].
- Copper: Usually paired with $0.5 - 1.0\%$ Tellurium (commonly called *Telco*) to improve machinability. Presents reasonable metal removal rates [A46].

- Copper tungsten: Very good wear characteristics, vastly used when machining carbides [A45]. Sintered material with 70% Tungsten and 30% Copper, difficult to machine.
- Silver Tungsten: Very specific applications where higher conductivity is desired [A46].
- Graphite: Commercially available in many grades. Undesired when machining carbides. May also be infused with copper particles (infiltrated graphite grades) that provides better machinability at the cost of higher wear.

B.2 Future procedure

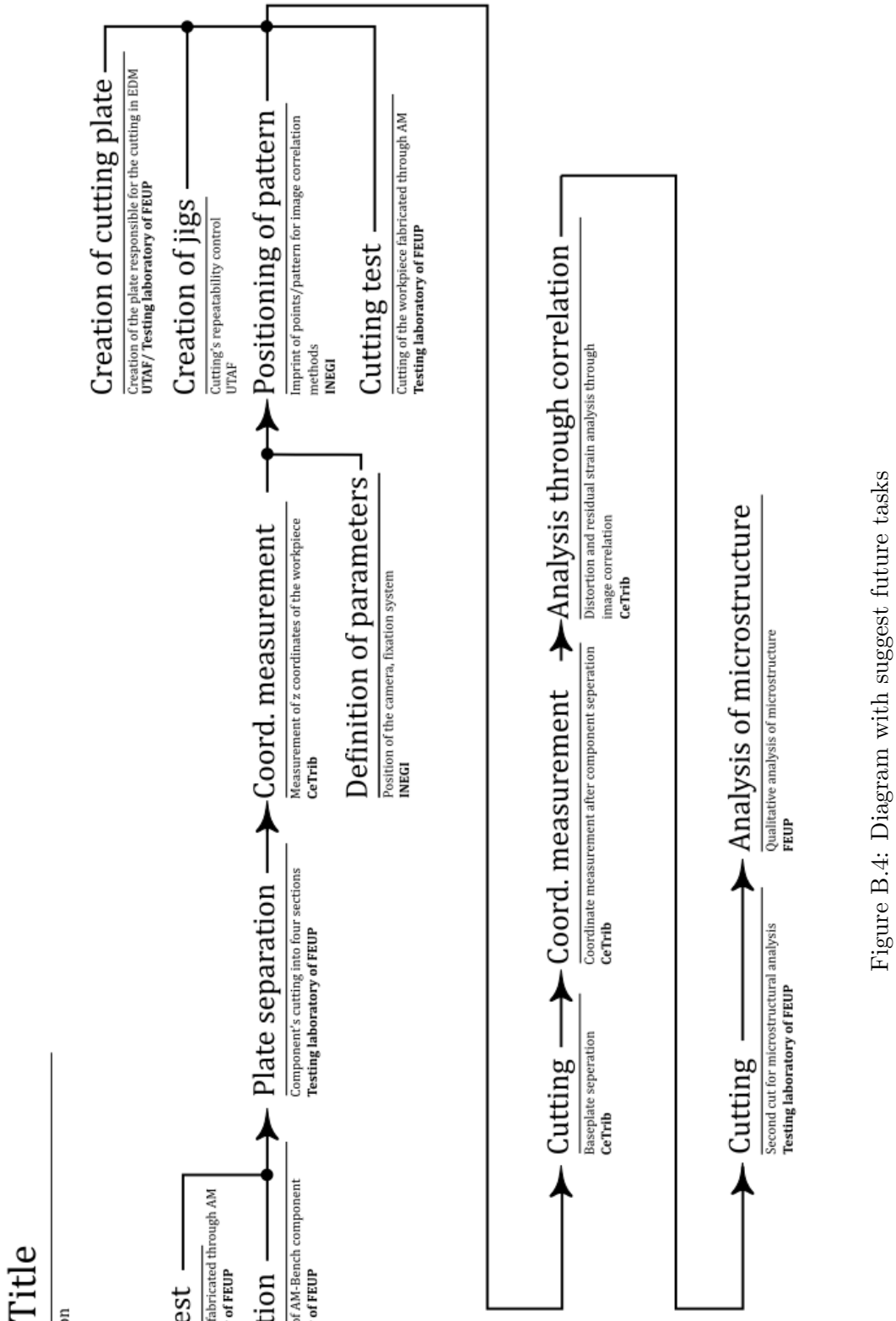

Figure B.4: Diagram with suggest future tasks

Appendix references

[A1] Wei Zhang. Technical Problem Identification for the Failures of the Liberty Ships. *Challenges*, 7(2):20–28, 2016.

[A2] W.D. Callister and W.D.C. William D. *Materials Science and Engineering: An Introduction, 7th Edition Wiley Plus Set*. John Wiley & Sons, Limited, 2007.

[A3] R.G. Budynas and J.K. Nisbett. *Shigley's Mechanical Engineering Design*. Number vol. 10 in McGraw-Hill series in mechanical engineering. McGraw-Hill, 8th edition, 2008.

[A4] J.C.R. Pereira, A.M.P., J. Xavier, and A.A. Fernandes. Ultra low-cycle fatigue behaviour of a structural steel. *Engineering Structures*, 60:214 – 222, 2014.

[A5] Qingyuan Wang, Muhammad Kashif Khan, and Claude Bathias. Current understanding of ultra-high cycle fatigue. *Theoretical and Applied Mechanics Letters*, 2(3):031002, 2012.

[A6] Igor Rychlik. Extremes, rainflow cycles and damage functionals in continuous random processes. *Stochastic Processes and their Applications*, 63(1):97 – 116, 1996.

[A7] Astm e1049-85(2017). *Standard Practices for Cycle Counting in Fatigue Analysis, ASTM International, Est Conshohocken, PA*, 2017.

[A8] IV Papadopoulos. Critical plane approaches in high-cycle fatigue: On the definition of the amplitude and mean value of the shear stress acting on the critical plane. *Fatigue & Fracture of Engineering Materials & Structures*, 21(3):269–285, 1998.

[A9] Y.L. Lee, M.E. Barkey, and H.T. Kang. *Metal Fatigue Analysis Handbook: Practical Problem-solving Techniques for Computer-aided Engineering*. Elsevier Science, 2011.

[A10] C.M. Branco, A.A. Fernandes, and P.M.S.T. Castro. *Fadiga de estruturas soldadas*. Fundação Calouste Gulbenkian, 2nd edition, 1986.

[A11] Takamoto Itoh, Masao Sakane, Masateru Ohnami, and Darrell F. Socie. Nonproportional Low Cycle Fatigue Criterion for Type 304 Stainless Steel. *Journal of Engineering Materials and Technology*, 117(3):285–292, 07 1995.

[A12] Yung-Li Lee, Tana Tjhung, and Algernon Jordan. A life prediction model for welded joints under multiaxial variable amplitude loading histories. *International Journal of Fatigue*, 29(6):1162 – 1173, 2007.

[A13] Chapter 1 - general features of the fatigue process. In Matěj Bílý, editor, *Cyclic Deformation and Fatigue of Metals*, volume 78 of *Materials Science Monographs*, pages 1 – 77. Elsevier, 1993.

[A14] L. Bairstow. The elastic limits of iron and steel under cyclic variations of stress. *Philosophical Transactions*, 210:35–55, 1910.

[A15] R. W. Landgraf. Cyclic deformation and fatigue behaviour of hardened steels. *Report*, 320:84–90, 1968.

[A16] Walter Ramberg and William R Osgood. Description of stress-strain curves by three parameters. page 29, 1943.

[A17] G. Masing. Eigenspannungen und verfestigung beim messing. pages 332–335, 1926.

[A18] JoDean Morrow. Cyclic plastic strain energy and fatigue of metals. In *Internal friction, damping, and cyclic plasticity*. ASTM International, 1965.

[A19] OH Basquin. Fatigue failure of notched specimen—a strainlife approach. In *American Society for Testing and Materials Proceedings*, volume 10, pages 625–630, 1910.

[A20] L Fo Coffin Jr. A study of the effects of cyclic thermal stresses on a ductile metal. *Transactions of the American Society of Mechanical Engineers, New York*, 76:931–950, 1954.

[A21] J Morrow. Fatigue properties of metals. *Fatigue design handbook*, pages 21–29, 1968.

[A22] J Walcher, D Gray, and SS Manson. Aspects of cumulative fatigue damage analysis of cold end rotating structures. *AIAA Paper*, pages 79–1190, 1979.

[A23] KN Smith. A stress-strain function for the fatigue of metals. *Journal of materials*, 5:767–778, 1970.

[A24] Alan Arnold Griffith. Vi. the phenomena of rupture and flow in solids. *Philosophical transactions of the royal society of london. Series A, containing papers of a mathematical or physical character*, 221(582-593):163–198, 1921.

[A25] G. R. Irwin. Fracture dynamics. *Fracturing of materials*, pages 147–166, 1948.

[A26] E. Orowan. Energy criteria of fracture. *Welding Journal*, 34:1575–1605, 1955.

[A27] David Broek. *Fatigue crack propagation*. Springer, 1982.

[A28] N. Perez. *Fracture Mechanics*. Springer International Publishing, 2016.

[A29] G.R. Irwin. Plastic zone near a crack and fracture toughness. *Sagamore Conf.*, 7:63, 1960.

[A30] Donald S Dugdale. Yielding of steel sheets containing slits. *Journal of the Mechanics and Physics of Solids*, 8(2):100–104, 1960.

[A31] Michigan State and East Lansing. Quantitative measurement of plastic strain field. (February):2399–2415, 2012.

[A32] C.T. Sun and Z.-H. Jin. Chapter 6 - crack tip plasticity. In C.T. Sun and Z.-H. Jin, editors, *Fracture Mechanics*, pages 123 – 169. Academic Press, Boston, 2012.

[A33] G.P. Cherepanov. Crack propagation in continuous media: Pmm vol. 31, no. 3, 1967, pp. 476–488. *Journal of Applied Mathematics and Mechanics*, 31(3):503 – 512, 1967.

[A34] James Rice. A path integral and the approximate analysis of strain concentration by notches and cracks. *Journal of Applied Mechanics*, 35:379–386, 01 1968.

[A35] PC Paris. The growth of fatigue cracks due to variations in load. *Lehigh University.*, 1962.

[A36] GC Noll and C Lipson. Allowable working stresses. *Society for Experimental Stress Analysis*, 3(2):29, 1946.

[A37] W.D. Pilkey and D.F. Pilkey. *Peterson's Stress Concentration Factors*. Wiley, 2008.

[A38] H.E. Boyer and A.S. Metals. *Atlas of Fatigue Curves*. American Society for Metals, 1985.

[A39] B.K. Parida. Fatigue testing. In K.H. Jürgen Buschow, Robert W. Cahn, Merton C. Flemings, Bernhard Ilschner, Edward J. Kramer, Subhash Mahajan, and Patrick Veyssière, editors, *Encyclopedia of Materials: Science and Technology*, pages 2994 – 2999. Elsevier, Oxford, 2001.

[A40] Paul H Wirsching. Statistical summaries of fatigue data for design purposes. page 63, 1983.

[A41] Böler. Böler w720 vmr maraging high strength steel, 2020.

[A42] JJoão Luís Alves Pereira. Fatigue behaviour of miniature specimens produced by additive manufacturing, 2019.

[A43] Joana Costa Leite Pereira de Melo. Comportamento à fadiga de aço maraging produzido por fabrico aditivo, 2020.

[A44] R Konečná, L Kunz, G Nicoletto, and A Bača. Long fatigue crack growth in inconel 718 produced by selective laser melting. *International Journal of Fatigue*, 92:499–506, 2016.

[A45] E.C. Jameson. *Electrical Discharge Machining*. Society of Manufacturing Engineers, 1st edition, 2001.

[A46] E.B. Guitrau. *The EDM Handbook*. Hanser, 2009.

[A47] Y. Altintas. *Manufacturing Automation: Metal Cutting Mechanics, Machine Tool Vibrations, and CNC Design*. Cambridge University Press, 2012.

[A48] K H Ho, S T Ã Newman, S Rahimifard, and R D Allen. State of the art in wire electrical discharge machining (WEDM). 44:1247–1259, 2004.